Novel coherent supercontinuum light sources based on all-normal dispersion fibers

by

Alexander M. Heidt

Dissertation presented for the degree of Doctor of Philosophy at the University of Stellenbosch

Promoter:
Prof. Dr. Erich G. Rohwer
University of Stellenbosch, Faculty of Science, Department of Physics

Co-Promoter:
Prof. Dr. Hartmut Bartelt
Friedrich-Schiller-University Jena, Germany, Faculty of Physics and Astronomy

December 2011

Declaration

By submitting this dissertation electronically, I declare that the entirety of the work contained therein is my own, original work, that I am the sole author thereof (save to the extent explicitly otherwise stated), that reproduction and publication thereof by Stellenbosch University will not infringe any third party rights and that I have not previously in its entirety or in part submitted it for obtaining any qualification.

December 2011

This thesis was prepared in the framework of a bi-national Cotutelle agreement between the University of Stellenbosch and the Friedrich-Schiller-Universität Jena, Germany.

Die vorliegende Arbeit wurde im Rahmen eines bi-nationalen Cotutelle Abkommens zwischen der University of Stellenbosch und der Friedrich-Schiller-Universität Jena (Deutschland) erstellt.

Abstract

The concept of broadband coherent supercontinuum (SC) generation in all-normal dispersion (ANDi) fibers in the near-infrared, visible and ultraviolet (UV) spectral regions is introduced and investigated in detail. In numerical studies, explicit design criteria are established for ANDi photonic crystal fiber (PCF) designs that allow the generation of flat and smooth ultrabroad spectral profiles without significant fine structure and with excellent stability and coherence properties. The key benefit of SC generation in ANDi fibers is the conservation of a single ultrashort pulse in the time domain with smooth and recompressible phase distribution. In the numerical investigation of the SC generation dynamics self-phase modulation and optical wave breaking are identified as the dominant nonlinear effects responsible for the nonlinear spectral broadening. It is further demonstrated that coherence properties, spectral bandwidth and temporal compressibility are independent of input pulse duration for constant peak power. The numerical predictions are in excellent agreement with experimental results obtained in two realizations of ANDi PCF optimized for the near-infrared and visible spectral region. In these experiments, the broadest SC spectrum generated in the normal dispersion regime of an optical fiber to date is achieved. The exceptional temporal properties of the generated SC pulses are verified experimentally and their applicability for the time-resolved study of molecular dynamics in ultrafast transient absorption spectroscopy is demonstrated. In an additional nonlinear pulse compression experiment, the SC pulses obtained in a short piece of ANDi PCF could be temporally recompressed to sub-two cycle durations by linear chirp compensation. Numerical simulations show that even shorter pulse durations with excellent quality can be achieved by full phase compensation. The concept is further extended into the UV spectral regime by considering tapered optical fibers with submicron waist diameter. It is shown that coherent SC spectra with considerable spectral power densities in the usually hard to reach wavelength region below 300 nm can be generated using these freestanding photonic nanowires. Although technological difficulties currently prevent the fabrication of adequate nanofibers, the concept could be experimentally verified by coherent visible octave-spanning SC generation in tapered suspended core fibers with ANDi profile. The work contained in this thesis therefore makes important contributions to the availability and applicability of fiber-based broadband coherent SC sources with numerous high-impact applications in fundamental science and modern technology.

Opsomming

Die konsep van breëband koherente superkontinuum (SK) in alles-normaal dispersiewe (ANDi) vesels in die naby-infrarooi, sigbare en ultraviolet (UV) spektrale gebiede word voorgestel en in detail ondersoek. In numeriese studies word eksplisiete ontwerpskriteria vasgestel vir ANDi fotoniese kristal vesel (FKV) ontwerpe wat dit moontlik maak om plat en gladde ultra-breë spektrale profiele te genereer sonder noemenswaardige fynstruktuur en met uitstekende stabiliteit en koherensie eienskappe. Die sleutel voordeel van SK genering in ANDi vesels is die behoud van 'n enkele ultrakort puls in tyd met 'n gladde en saamdrukbare fase distribusie. In die numeriese ondersoek van die SK generering is die dinamika van fase selfmodulering geïdentifiseer as die dominante nie-lineêre effek wat verantwoordelik is vir die nie-lineêre spektrale verbreding. Daar word voorts aangetoon dat die koherensie eienskappe, spektrale bandwydte en saamdrukbaarheid in tyd onafhanklik is van die inset pulsduur vir konstante drywing. Die numeriese voorspellings stem uitstekend ooreen met die eksperimentele resultate wat verkry is met twee ANDi FKVÕs wat optimeer is vir die naby-infrarooi en sigbare spektrale gebied. In hierdie eksperimente is die breedste SK spektrum gegenereer wat tot hede in die normaal dispersiewe regime met 'n optiese vesel behaal is. Die besondere eienskappe van die genereerde SK pulse is eksperimenteel bevestig en die toepasbaarheid vir tyd opgelosde studie van molekulêre dinamika is gedemonstreer. In 'n addisionele nie-lineêre puls kompressie eksperiment is SK pulse verkry in 'n kort stuk ANDi FKV wat in tyd saamgedruk kon word tot sub-twee siklus tydsduur deur liniêre tjirp kompensering. Numeriese simulasies toon aan dat selfs korter pulse met uitstekende kwaliteit behaalbaar is met volledige fase kompensasie. Die konsep is verder uitgebrei na die UV spektrale gebied deur 'n koniese vesel te beskou met sub-mikron diameter. Daar is aangetoon dat koherente SK spektra met noemenswaardige spektrale drywing in die golflengte gebied onder 300 nm, wat gewoonlik as moeilik toeganklik beskou word, bereik kan word deur hierdie vrystaande fotoniese nano-vesels aan te wend. Alhoewel tegnologiese probleme die vervaardiging van voldoende nano-vesels verhinder, kon die konsep eksperimenteel bewys word deur koherente sigbare oktaafspannende SK te genereer in koniese gesuspendeerde kern vesels met 'n ANDi profiel aan te wend. Die werk wat in die tesis vervat is, maak dus belangrike bydraes tot die beskikbaarheid en toepasbaarheid van vesel gebaseerde breëband koherente SK bronne met verskeie hoë impak toepassings in fundamentele wetenskap en moderne tegnologie.

Contents

1. Introduction

Nonlinear fiber optics has experienced a boost in research interest with the invention of the photonic crystal fiber (PCF) [1, 2, 3] and the subsequent demonstration of extreme nonlinear spectral broadening or supercontinuum (SC) generation [4, 5]. Although SC generation was demonstrated earlier in bulk materials and standard nonlinear fibers [6, 7, 8], the possibility of controlling the dispersion characteristics in PCF is revolutionary. The bandwidth and properties of the generated SC spectrum are critically dependent on the relationship between pump wavelength and dispersion profile of the fiber, and the design flexibility of PCF enables the adaption of the fiber to available pump sources and the tailoring of the SC properties to the requirements of specific applications [9, 10]. In addition, PCF offer enhanced nonlinearity compared to conventional fibers [11] and can exhibit single-mode behaviour over broad wavelength ranges [12]. These unique properties of PCF allow SC generation over a much wider range of source parameters than has been possible in conventional fibers or bulk media, and high brightness broadband spectra have been generated using pump pulses from the femto- to the nanosecond regime as well as using continuous wave (CW) sources [13, 14, 15, 16]. Consequently, PCF based SC generation has been widely applied in diverse research fields such as spectroscopy [17], optical coherence tomography [18] and telecommunications [19]. However, the most prominent application is certainly in optical frequency metrology and carrier envelope phase control, which culminated in the award of the 2005 Nobel Prize in Physics to Hall and Hänsch [20, 21].

The generation of ultra-broadband and simultaneously highly coherent spectra puts demanding requirements on the pump source. In the conventional setup using a fiber with single zero dispersion wavelength (ZDW) and pumping in the anomalous dispersion regime, highly stable pulses of typically less than 50 fs duration and nanojoule pulse energies are necessary to maintain high temporal coherence [22]. The broadening dynamics are in this case dominated by soliton dynamics, in particular the break-up of the injected pulse due to soliton fission [23]. For longer pulses, the SC generation dynamics become very sensitive to fluctuations of the input pulse and pump laser shot noise due to the increasing noise amplification through modulation instability (MI) gain [24, 25]. Consequently, these ultra-broad SCs are characterized by a complex temporal profile and phase distribution, considerable fine structures over their spectral bandwidth and in addition exhibit pulse-to-pulse variations in intensity and phase if not pumped by extremely short pulses [26, 27].

The noise sensitivity is often a precision or resolution limiting factor and a relaxation of the pump source requirements would be beneficial for many applications [28, 29]. A

highly coherent broadband spectrum, uniform and smooth spectral power densities, the conservation of a single pulse in the time domain with stable and recompressible phase distribution or combinations thereof are especially critical for applications in which the temporal profile and phase stability of the SC pulse is of importance. This includes, for example, time-resolved spectroscopic measurements, amplification of SC pulses in parametric processes, few- or single-cycle pulse compression as well metrology and telecommunication applications. Therefore, considerable research effort has been directed towards fiber designs limiting the detrimental effects of soliton dynamics on coherence properties and spectral fine structure.

One approach to achieve coherent and recompressible SC spectra has been the suppression of soliton fission in PCF with convex and flattened dispersion profile exhibiting two closely spaced ZDWs centered near the pump [30]. The resulting stable and coherent SC features two distinct spectral peaks on the normal dispersion side of each ZDW [31], and has found successful application in coherent anti-Stokes Raman scattering microscopy [32], but the missing spectral content in between the two ZDWs is not ideal for applications requiring continuous broadband spectra. This type of PCF has also been numerically investigated in a taper configuration having all-normal dispersion after a certain distance, which was shown to result in improved stability [33].

In a further development of this concept, improved spectral flatness has been achieved by using dispersion-flattened dispersion-decreasing fibers (DF-DDFs) [34]. Starting with a profile with two ZDWs, the convex dispersion longitudinally decreases from anomalous to normal values in the vicinity of the pump. This leads to a decreasing separation of ZDWs until the dispersion is normal at all wavelengths. The decreasing anomalous dispersion induces adiabatic soliton compression that prevents fission, followed by the generation of dispersive waves which create a coherent spectrum over the bandwidth [35]. However, there is a restriction on the soliton number of the input pulse to maintain the coherence and, consequently, applications of DF-DDFs have been mainly found in telecommunications using low peak power picosecond pulses and the spectrum exhibits a $\sim$ 20 dB peak around the pump wavelength [36].

Soliton dynamics and the associated problems can also be avoided when pumping occurs entirely in the normal dispersion regime, but this is usually associated with significantly reduced spectral bandwidths due to the fast temporal broadening of the input pulse [37]. Especially if only longer pump pulses with durations of a few hundred femtoseconds are available, there seems to be a trade-off between maximizing spectral bandwidth by anomalous dispersion pumping or achieving high coherence by normal dispersion pumping [25]. However, the results described above give an indication that the optimization of the fiber dispersion properties may overcome the limitations of this trade-off, and the transition from fibers with two ZDWs to all-normal dispersion (ANDi) fibers seems especially interesting. Reports of stable ultraflat SC generation in fibers with ANDi profiles (which remain constant during propagation) at wavelengths of 1550 nm and above further emphasize the importance of this fiber type [38, 39], but design and scaling possibilities have never been investigated in detail.

The main objective of this thesis is therefore the development of optimized optical fibers for pulse-preserving and spectrally uniform broadband coherent SC generation for ultrashort time-resolved applications, focussing on silica fibers with convex dispersion profiles. The influence of the fiber design and input pulse parameters on the generated spectrum and resulting pulse profile is examined in detail with the aim of optimizing the SC generation process in such a way that (i) a single pulse is maintained during the propagation through the fiber; (ii) this pulse is recompressible, preferably by simple means such as a grating or a prism pair; and (iii) a broadband, stable, and flat-top spectrum with a high spectral power density over the entire bandwidth is achieved. Ideally, these properties should also be obtainable for pump pulses of a few hundred femtoseconds duration.

The thesis is structured in the following way: chapter 2 briefly reviews the properties, involved nonlinear effects and dynamics of conventional SC generation in fibers with single ZDW under anomalous dispersion femtosecond pumping and details the challenges that need to be addressed in the thesis. The numerical model used for the simulation of nonlinear pulse propagation in optical fibers and its implementation details are discussed in chapter 3, and the conservation quantity error method (CQEM) is introduced as a novel and highly efficient longitudinal step size adaption algorithm. In chapter 4, a comprehensive survey over possible PCF design and input pulse parameters is presented, focussing on the pump wavelength of Ytterbium-doped fiber lasers around 1 μm. Design criteria are established for the optimization of spectral bandwidth and flatness. It is shown that more than octave-spanning highly coherent and uniform spectra can be generated in optimized ANDi fibers, which are virtually independent of the input pulse duration for constant peak power.

The main experimental results of the thesis are presented in chapter 5. The numerical predictions of the previous chapter are confirmed and octave-spanning SC generation in two realizations of ANDi PCF optimized for pumping in the visible and near-infrared spectral regions is demonstrated. The conservation of a single pulse in the time domain with smooth phase distribution and its applicability in ultrafast transient absorption spectroscopy is experimentally verified. The stable and smooth spectral phase of the SC is exploited by demonstrating temporal recompression of the generated SC pulse to sub-two cycle duration simply by linear chirp compensation.

Chapter 6 transfers the design concepts developed in chapter 2 to tapered nanofibers and tapered suspended core fibers exhibiting all-normal dispersion profiles with the aim of extending the SC bandwidth towards shorter wavelengths. The possibility of generating coherent SCs in the deep ultraviolet (UV) regime by 400 nm pumping of tapered fibers with sub-micron diameter waist is analyzed numerically and the conditions for experimental success are specified. The concept is proven with the experimental demonstration of coherent visible SC generation in tapered suspended core fibers, and fiber designs are specified that would allow further extension of the SC bandwidth towards the UV range.

Finally, and outlook is given and future scaling possibilities are briefly discussed in chapter 7.

2. Conventional supercontinuum generation in optical fibers

Nonlinear fiber optics is a very mature field of research and the processes responsible for SC generation have been investigated for a wide range of fiber and pump pulse parameters. Excellent books and review articles are available in literature [8, 25, 35, 40]. Therefore, the purpose of this chapter is not a comprehensive overview of the field, but a very brief review of the involved nonlinear effects and generation dynamics applicable to the scope of the thesis.

SC generation in optical fibers can roughly be divided into two regimes by considering the duration of the employed pump pulses. If the SC is generated with femtosecond pulses, soliton dynamics usually play the key role in the spectral broadening process, while for picosecond, nanosecond or CW pumps modulation instability/four-wave mixing dominates the initial broadening process. Consequently, the properties of the generated SCs in the two regimes are generally quite different. While SCs generated with femtosecond pump pulses can be highly coherent both temporally and spatially, in the long pump pulse regime the generation dynamics are usually seeded by random noise, which leads to substantial shot-to-shot fluctuations and therefore the loss of temporal coherence [25]. Since the objective of this thesis is the development of optical fibers for highly coherent and pulse-preserving SCs relevant to ultrafast time-resolved applications, the discussion will be limited to the case of femtosecond pumping.

The most commonly considered configuration in SC generation with femtosecond pulses is the pumping in the anomalous dispersion regime close to the single ZDW of the fiber. This will be referred to as *conventional SC generation* throughout this document. Here a summary of the involved dynamics and the properties of this SC type is provided, which will be used as reference for comparison in the later chapters of the thesis.

The general argumentation of this chapter follows the discussions in [25, 41, 42]. Although numerical simulations are used to illustrate certain dynamics, the chapter focusses on the physical description of the involved processes. The numerical details and implementation are discussed in chapter 3.

2.1. Physical mechanisms

2.1.1. Dispersion

The relationship between pump wavelength and the dispersion profile of the fiber is one of the most important factors determining the characteristics of the generated SC. It has been found that the broadest more than octave-spanning spectra can be generated when pumping occurs close to the ZDW of the fiber in the anomalous dispersion region [43]. In conventional silica fibers the dispersion is dominated by the material dispersion, and the ZDW is located in the vicinity of 1.3 μm wavelength, which is far from the emission wavelength of the most commonly employed femtosecond pump sources based on Ti:sapphire (800 nm) or Ytterbium (1 μm). PCF possess additional design degrees of freedom that allow the engineering of the dispersion profile, its adaption to specific pump sources and the tailoring of the generated SC properties to specific applications [44]. In PCF, the light is guided in a silica core, which is surrounded by a photonic crystal cladding of air holes, most commonly arranged in a hexagonal lattice structure (Fig. 2.1 a)). Note that the expressions "PCF" and "microstructured fiber" are used in this thesis synonymously to refer to the type of fiber that guides light on the basis of total internal reflection - bandgap guiding fibers are not considered. For small core diameters, the photonic crystal cladding has a significant influence on the waveguide dispersion, which is added to the material dispersion of silica to yield the total dispersion profile of the fiber. By adjusting the two design parameters pitch Λ and relative hole diameter d/Λ, the position of the ZDW can be controlled and shifted far into the visible. Additionally, the slope of the dispersion profile is also adjustable within certain limits, which enables for example the design of PCF with two ZDWs. Additional design flexibility arises through the change of the fiber dimensions by tapering or by using rings of air holes with different sizes or structures other than hexagonal, which will be considered in chapter 6 of this thesis.

The dispersion characteristics of PCF can be obtained by numerically solving the vectorial transverse wave equation. Both commercial packages (Comsol Multiphysics) and free software based on the multipole method (CUDOS MOF, [45]) are used in this thesis. In addition, an analytical method to obtain dispersion and effective mode field diameter of the fundamental mode is useful for quick calculations and surveys over multiple fiber geometries [46, 47], but the validity of the method over the desired parameter range should first be confirmed by numerical packages. Fig. 2.1 b) shows the numerically calculated group velocity dispersion (GVD) profile of the PCF with $\Lambda = 1.8$ μm and $d/\Lambda = 0.8$ as well as the contributions of material and waveguide dispersion. Here the GVD dispersion paramater $D = -(2\pi c/\lambda^2)\beta_2$ is used, where λ is the wavelength, c the vacuum speed of light and $\beta_2 = \frac{\partial}{\partial\omega}\frac{1}{v_g}$ is related to the angular frequency variation of the group velocity v_g. The wavelength range where $D < 0$ ($\beta_2 > 0$) is called the normal dispersion regime, in which the group velocity decreases with wavelength. The opposite is the case in the range with $D > 0$ ($\beta_2 < 0$), which is called the anomalous dispersion regime. The ZDW is located where $D = 0$, in this case at around 780 nm. The figure clearly illustrates that

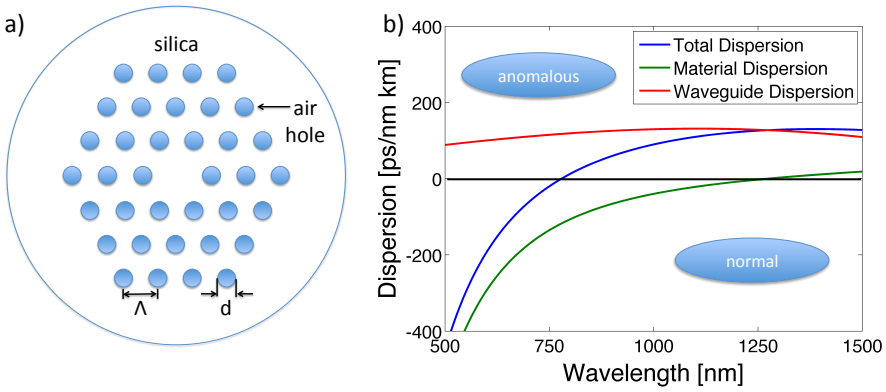

Figure 2.1. – a) Schematic illustration of a photonic crystal fiber (PCF) with hexagonal lattice of air holes in a silica background. The core is formed by a defect in the lattice structure. The fiber design parameters pitch Λ and hole diameter d are indicated. b) Wavelength dependence of material, waveguide and total dispersion of a PCF with $\Lambda = 1.8$ μm and $d/\Lambda = 0.8$. The zero dispersion wavelength is located around 780 nm. The regions of normal and anomalous dispersion are indicated.

the waveguide dispersion adds a significant normal dispersion component to the material dispersion of silica such that the dispersion profile is essentially shifted upwards, which causes the shift of the ZDW towards the visible wavelengths.

GVD is a linear effect and in the absence of nonlinearity leads to a temporal broadening of an initially transform-limited pulse in both normal and anomalous dispersion regimes. In the presence of nonlinearity, however, the sign of the GVD becomes an important factor and determines the effects participating in the spectral broadening dynamics [48].

2.1.2. Self-phase modulation

Self-phase modulation (SPM) arises from the intensity dependence of the refractive index and leads to spectral broadening of optical pulses [49]. Neglecting the influence of dispersion and loss in the fiber, the time dependent temporal intensity $I(t)$ of an optical pulse causes a modulation of the refractive index $n = n_0 + n_2 I(t)$, with n_0 and n_2 the linear and nonlinear refractive index, respectively. In order to be consistent with the parameters used in the later chapters of this thesis, the intensity is written as $I(t) = P_0/A_{\text{eff}} U(t)$ with the peak power P_0, effective mode field area A_{eff} and normalized intensity profile $U(t)$. The intensity dependent refractive index introduces a time dependent phase $\Phi(t)$ and consequently a time dependent instantaneous frequency

$$\omega(z,t) = -\frac{\partial \Phi}{\partial t} = \omega_0 - \gamma P_0 \frac{\partial U(t)}{\partial t} z, \tag{2.1}$$

where the nonlinear parameter $\gamma = (n_2 \omega_0)/(c A_{\text{eff}})$ is introduced [48]. SPM therefore creates new spectral components, whose separation from ω_0 increase with nonlinearity, peak power, slope of the pulse and propagation distance z. At the leading edge of the

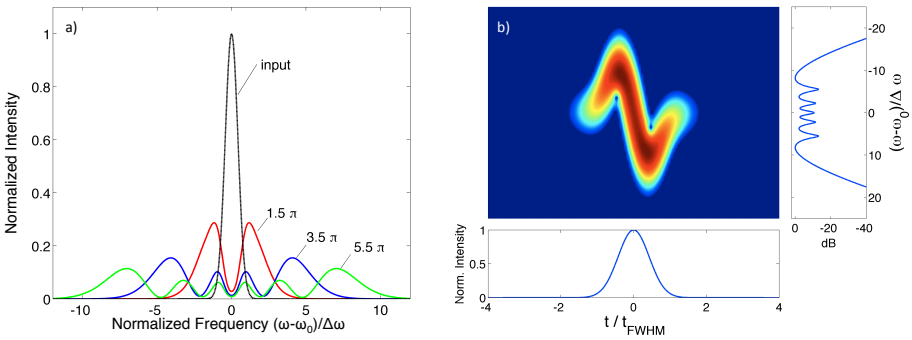

Figure 2.2. – a) SPM induced spectral broadening for a Gaussian pulse shape and different values of the maximum nonlinear phase shift $\Phi_{\mathrm{NL}}^{\mathrm{max}}$. Spectrogram of the pulse with $\Phi_{\mathrm{NL}}^{\mathrm{max}} = 5.5\pi$.

pulse, where the slope of the rising intensity profile is positive, the spectrum is broadened towards red shifted lower frequencies, while a broadening towards blue shifted higher frequencies is introduced at the trailing pulse edge, where the slope of the intensity profile is negative.

As an example, Fig. 2.2 a) shows the SPM induced spectral broadening for a Gaussian pulse shape and different values of the maximum nonlinear phase shift $\Phi_{\mathrm{NL}}^{\mathrm{max}} = \gamma P_0 z$. The most remarkable feature is the development of an oscillatory structure in the spectrum. In general, the spectrum consists of many peaks, and the outmost peaks are the most intense. The number of peaks and the spectral broadening depend on the magnitude of $\Phi_{\mathrm{NL}}^{\mathrm{max}}$ and increase linearly with it. Fig. 2.2 b) makes use of the spectrogram representation to illustrate the time - frequency correlation of the pulse with $\Phi_{\mathrm{NL}}^{\mathrm{max}} = 5.5\pi$ and summarizes the most important features of SPM-induced spectral broadening. While the temporal pulse shape remains unaffected, the spectrogram clearly shows the red shift on the leading and the blue shift on the trailing pulse edge. The central section exhibits an almost linear chirp, i.e. the instantaneous frequency varies linearly in time, which leads to the typical S-shape of the spectrogram. Spectral interference of identical spectral components being present at different temporal positions within the pulse can be identified as the origin of the oscillatory spectral structure.

SPM occurs if the modulation of n is caused by the pulse itself. However, this modulation can also be caused by a co-propagating pulse, in which case a coupling due to cross-phase modulation (XPM) occurs [48].

If dispersion is included into the discussion, fundamentally different behaviour can be observed in the two dispersion regimes. SPM and normal dispersion lead to a simultaneous temporal and spectral broadening. The interaction of SPM and normal dispersion is crucially important for the interpretation of the results in this thesis and will be discussed in detail in section 4.4. In the anomalous dispersion regime, SPM and dispersion can balance each other and lead to the formation of solitons.

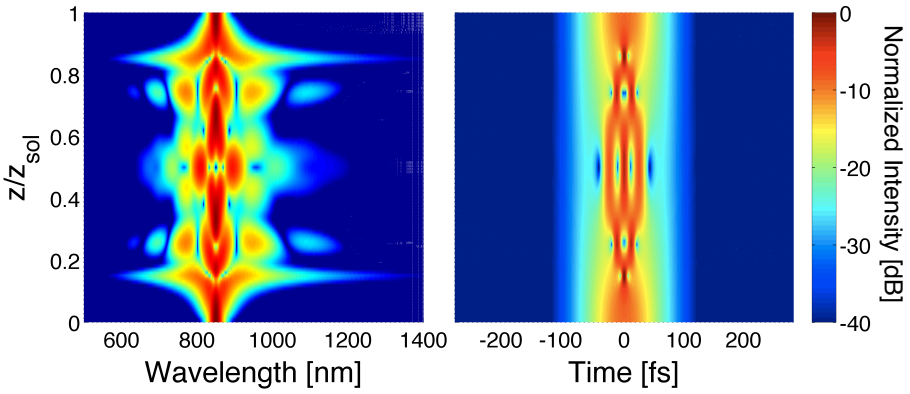

Figure 2.3. – Spectral and temporal evolution of a $N = 4$ soliton with propagation distance z over one soliton period z_{sol}.

2.1.3. Soliton dynamics

A soliton is formed when the nonlinear chirp induced by SPM is balanced by the linear chirp from GVD in the anomalous dispersion regime, i.e. when $\beta_2 < 0$ and higher order dispersion terms can be neglected [50]. Solitons are solutions to the nonlinear Schrödinger equation (3.7) and their temporal electric field envelope (3.5) can be described as $A(t) = N\mathrm{sech}(t/t_0)$, where t_0 is a measure of the pulse width and N is called the soliton number. It is determined by both pulse and fiber parameters through $N^2 = L_{\mathrm{D}}/L_{\mathrm{NL}}$, where $L_{\mathrm{D}} = t_0^2/|\beta_2|$ and $L_{\mathrm{NL}} = 1/(\gamma P_0)$ are the dispersive and nonlinear length scales, respectively. For the fundamental soliton with $N = 1$, both temporal and spectral profiles remain unchanged during propagation. Higher order solitons with $N > 1$ undergo a periodic spectral and temporal evolution, which is illustrated in Fig. 2.3 for the example of a $N = 4$ soliton. Here the fiber parameters $\beta_2 = -14.8$ ps^2/km and $\gamma = 0.08$ W^{-1}m^{-1} of the PCF from Fig. 2.1 were used for an initial pulse with 850 nm central wavelength, $t_0 = 28.4$ fs (corresponding to 50 fs full width at half maximum) and $P_0 = 3.68$ kW. The propagation distance over one soliton period $z_{\mathrm{sol}} = (\pi/2)L_{\mathrm{D}}$ is considered. The initial nonlinear spectral broadening and associated temporal compression is characteristic for all higher order solitons, while the subsequent evolution varies for different N [48]. A high peak-power femtosecond pulse injected into the anomalous dispersion regime of a fiber generally evolves into a soliton with $N >> 1$ [51], and the initial stage of the spectral broadening process is qualitatively similar to this example.

Soliton fission

The perfect periodic evolution of higher order solitons is only stable in the absence of any perturbation. In reality, the presence of higher order dispersion and Raman scattering perturbs the soliton evolution and the injected higher order soliton breaks up into a train of fundamental solitons, whose number is identical to the initial soliton number N [52]. The fundamental solitons are ejected one by one, the ones ejected first having the highest

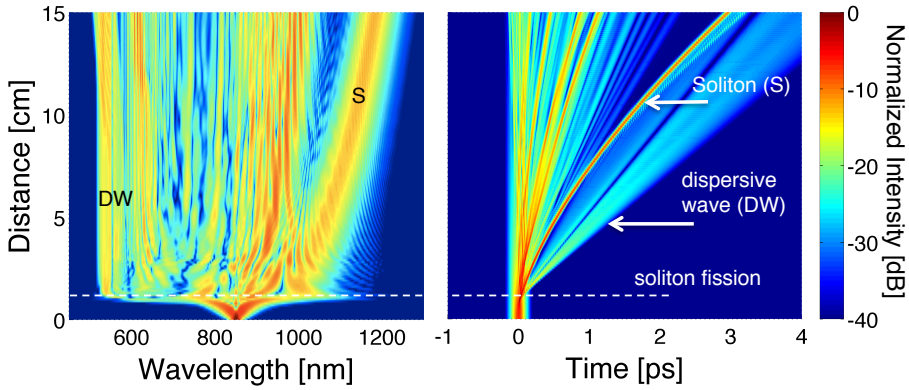

Figure 2.4. – Spectral and temporal evolution of the SC generation process in the PCF of Fig. 2.1, pumped in the anomalous dispersion regime at 850 nm with a 50 fs, 10 kW input pulse.

amplitude and shortest duration [53]. This break-up is called soliton fission and occurs typically after a distance of $L_{\text{fiss}} \approx L_{\text{D}}/N$ when the initial soliton reaches its maximum bandwidth [25].

Soliton self-frequency shift and dispersive wave generation

After the soliton fission, each individual fundamental soliton experiences a shift to longer wavelengths due to the soliton self-frequency shift caused by intra-pulse Raman scattering [54]. Quantum-mechanically this process can be interpreted by the scattering of a photon by a silica molecule, resulting in a lower frequency photon and a higher vibrational state of the molecule. The dynamics of the frequency shift ν_R can be described as $\mathrm{d}\nu_R/\mathrm{d}z \propto |\beta_2|/t_0^4$ [55], which leads to a stronger shift for the the first ejected solitons from the fission process and therefore to an increasing separation between the individual solitons with propagation distance. In addition, the presence of higher order dispersion can lead to energy transfer from the solitons to a resonance band in the normal GVD regime, which is referred to as the dispersive wave. Its position can be determined from a phase-matching argument [56].

2.2. Deconstruction of supercontinuum generation dynamics

While the above discussion focussed on the most important isolated nonlinear effects, Fig. 2.4 shows the full simulation of the SC generation process in the PCF of Fig. 2.1, pumped with the 50 fs input pulse at 850 nm already considered in the discussion of soliton dynamics, but with a higher peak power of 10 kW. The corresponding soliton number is $N \approx 6.6$. The initial dynamics of spectral broadening and temporal compression are similar to the evolution of a higher order soliton shown in Fig. 2.3. After about 1.5 cm

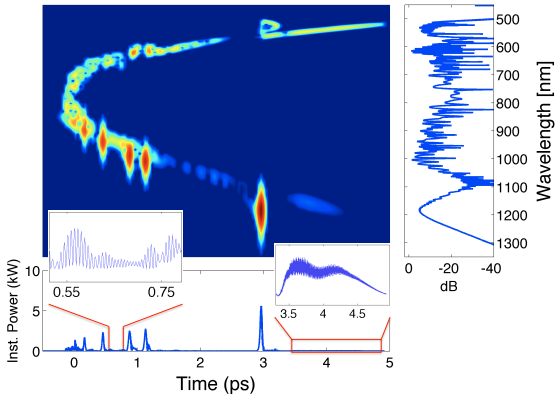

Figure 2.5. – Spectrogram of the generated SC after 15 cm propagation distance.

soliton fission takes place, caused by higher order dispersive and nonlinear perturbations. The input pulse, which forms a higher order soliton inside the fiber, breaks up into its fundamental constituents, as can be clearly seen in the temporal evolution, where the first ejected fundamental soliton with the highest peak power is indicated. Each ejected soliton subsequently shifts to longer wavelengths due to the soliton self-frequency shift and transfers energy to a dispersive wave (DW) in the normal GVD regime. At longer wavelengths, the solitons experience a larger amount of GVD and are slowed down with respect to the retarded time reference frame which travels at the envelope group velocity of the input pulse. As discussed above, the first ejected soliton experiences the highest amount of frequency shift and is therefore clearly temporally separated from the subsequent solitons. Its red-shifting spectral signature (S) is clearly identifiable in the spectral evolution. After ca. 2 cm, the broadening of the spectrum is essentially concluded, only the self-frequency shift of this highest peak power soliton extends the spectrum further into the infrared.

Even more insight into the origin of the complex temporal and spectral features of the generated SC can be obtained from the time-wavelength correlations visible in the spectrogram in Fig. 2.5, in which the dispersive properties of the fiber are evident by the parabolic variation of the group delay with wavelength. The fundamental solitons are lined up according to their amplitude, and the prominent spectral feature on the long wavelength side can immediately be identified as the spectral signature of the highest amplitude soliton. The oscillatory structure in the central section of the SC spectrum is explained by spectral interference of the overlapping bandwidths of the subsequent solitons. In addition, the temporal signature of the dispersive wave becomes identifiable as a low level pedestal at the trailing edge of the pulse. Finally, temporal beating between distinct wavelengths components are the origin of low level complex temporal structures and fast oscillations.

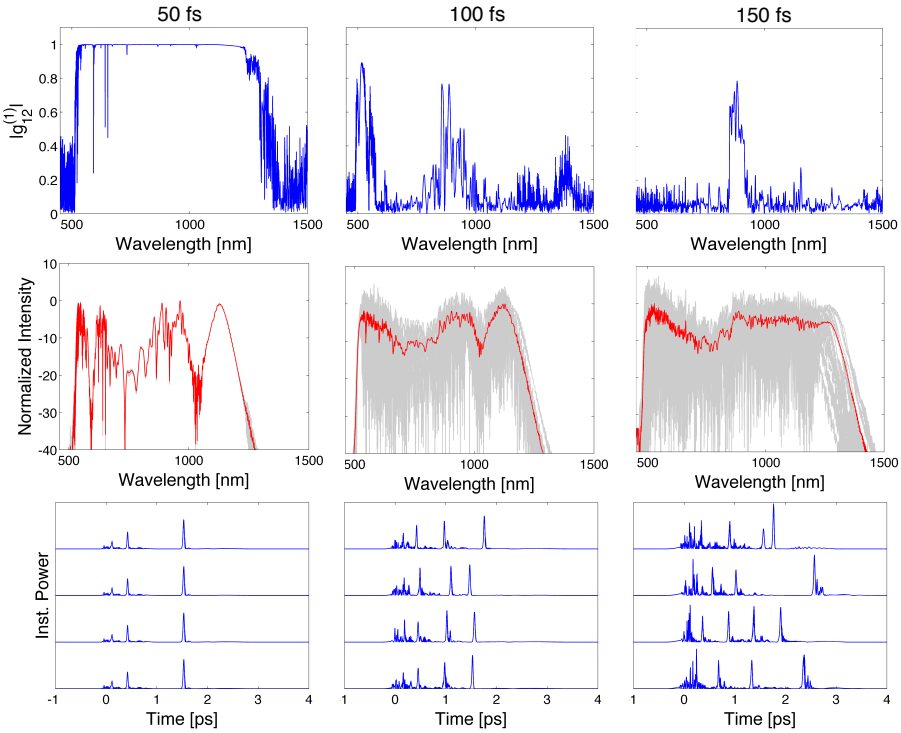

Figure 2.6. – Temporal coherence and stability calculations from an ensemble of 20 individual simulations including noise for pump pulse durations of 50 fs, 100 fs and 150 fs at a fixed peak power of 10 kW and 10 cm propagation distance. Top: coherence function $|g_{12}^{(1)}(\lambda)|$. Center: individual spectra (grey) and mean spectrum (red). Bottom: Four randomly selected temporal profiles at the fiber end, displayed with 10 kW offsets.

2.3. Coherence and stability

Up to now, all shown simulations were obtained from single shot calculations. However, it has been shown that depending on the considered parameter regime the SC generation can be very sensitive to input pulse shot noise and fluctuations introduced by spontaneous Raman scattering, resulting in considerable shot-to-shot variations of the output SC [22, 24]. The noise sensitivity can be numerically investigated by including stochastical parameters into the simulations, as described in section 3.1.2, and comparing the results of 20 individual simulations obtained with different noise seeds. The fluctuations are characterized by the spectrally resolved modulus of first order coherence at zero path difference $|g_{12}^{(1)}(\lambda, t_1 - t_2 = 0)|$ (3.11), which yields a positive number in the interval [0;1] with the value of 1 representing perfect coherence. Fig. 2.6 shows the calculated coherence function as well as spectral and temporal fluctuations for identical fiber parameters as above, but for varying input pulse durations and shorter propagation distance of 10 cm. For the 50 fs input pulse $|g_{12}^{(1)}(\lambda| \approx 1$ over almost the entire bandwidth indicates high stability of the output SC, which is confirmed by the absence of both spectral and temporal fluctuations. For higher pump pulse durations, however, temporal and spectral

shot-to-shot fluctuations become significant and the coherence is degraded significantly.

The spectral bandwidth increases for longer pulse durations, because the pulse energy is increased to keep a constant peak power. The figure also illustrates that the mean spectrum, which would be measured by a slow spectrometer averaging over many shots, appears smoother for longer pump pulse durations, although in reality increasing shot-to-shot fluctuations are present.

It is interesting to note that setting the Raman gain to zero and repeating the simulations yields similar coherence properties, indicating that the input pulse shot noise is the main reason for decoherence. In literature, the mechanism of decoherence for the longer pump pulse durations is attributed to noise seeded modulation instability (MI), which induces soliton fission before other perturbations such as higher order dispersion or Raman scattering become significant [25]. The position where soliton fission occurs is therefore random and its products completely incoherent. In contrast, the initial spectral broadening for shorter pulses is very fast and spectral overlap with the maximum MI gain is obtained before noise seeded amplification becomes significant. This results in coherent seeding of the MI gain bandwidth and therefore a more deterministic occurrence of soliton fission. The ratio of soliton fission characteristic length L_{fiss} and the characteristic length of MI $L_{\mathrm{MI}} = L_{\mathrm{NL}}/2$ [48] determines the degree of coherence. The ratio is proportional to N, and therefore a critical value $N_{\mathrm{crit}} \approx 10$ of the soliton number exists above which soliton fission will be initiated by MI thus changing the nature of the continuum from coherent to incoherent. For longer pulses, the peak power needs to be drastically reduced to maintain coherence. Hence, continua with practically usable spectral power densities generated with pump pulses longer than 100 fs are typically incoherent.

It is important to understand that both input pulse shot noise and spontaneous Raman scattering are quantum noise sources and therefore intrinsic to the SC generation process. In contrast, additional technical noise sources such as pump laser power fluctuations and beam pointing stability are not considered here, because they can be eliminated by optimizing the experimental conditions [24].

2.4. Advantages and challenges

It is clear from the discussion above that conventional SC generation in microstructured optical fibers offers a number of advantages compared to SC generation in bulk media or standard optical fibers. However, especially in the context of applications in which the temporal profile and coherence of the SC is of importance, such as time-resolved spectroscopy, telecommunications, optical parametric amplification and pulse compression, some of the discussed properties become problematic and represent challenges that require careful control of the nonlinear processes involved in the spectral broadening dynamics. Without claiming completeness, both advantages and challenges are summarized in the following list.

Advantages:

- spectral bandwidth: the enhanced nonlinearity and modified dispersion properties of PCF allow the generation of more than octave-spanning potentially highly coherent spectra with pulse energies below 1 nJ, which enables the use of relatively simple unamplified pump sources. In contrast, the generation of similar bandwidths in bulk media requires significantly more complex sources and pulse energies in the μJ regime.

- spatial profile: the broadband single mode guiding properties of PCF result in a uniform spatial profile, which ensures excellent spatial coherence properties. Filamentation effects in bulk media often lead to more complex spatial profiles.

- design possibilities: the high index contrast between silica core and air holes leads to a significant contribution of the waveguide dispersion, which is extremely sensitive to the cladding geometry and allows the adaption of the dispersion properties to the requirements of specific pump sources and applications.

- conversion efficiency: the wavelengths conversion from the pump to spectral wings is generally highly efficient, in the final spectrum the pump wavelength is usually not more prominent than the rest of the spectrum. In contrast, the conversion in bulk is generally less efficient, which results in a dominant spectral peak around the pump wavelength with a low level SC background. Filtering of the pump is usually required for the subsequent application.

Challenges:

- pulse conservation: in conventional SC generation, the spectral broadening is inherently connected to the breakup of the injected pulse due to soliton fission, resulting in highly complex temporal profiles and phase distributions. In time-resolved spectroscopy, for example, this causes a severe degradation of temporal resolution. In pulse compression, the complex phase distribution significantly limits the practically achievable pulse duration and quality. It would therefore be desirable if soliton fission is suppressed and a single ultrashort pulse is maintained in the time domain.

- spectral uniformity: the highly structured nature of the spectra shown above is problematic for applications which require, for example, spectrally uniform sensitivity and signal-to-noise ratios or fast readout of the spectra and hence cannot use sensitive but slow spectrum analyzers. The variation of spectral intensity with wavelength is also undesirable in the development of fiber-based tunable sources based on parametric processes or pulse compression to the single-cycle regime. Consequently, the spectral broadening dynamics have to be optimized to increase spectral flatness.

- coherence: a major drawback of conventional SC generation is its sensitivity to input pulse shot noise, which puts demanding requirements on the pump sources if highly coherent spectra are desired. It is highly desirable to relax these requirements

and make highly coherent broadband SC generation possible for longer input pulse durations as well. Therefore, the noise-seeding of MI gain bandwidths needs to be suppressed.

In the following chapters of the thesis, these challenges will be addressed and resolved, mainly by exploiting the advantage of substantial design possibilities in PCF and tapered optical fibers. Extensive numerical simulations are used to establish optimized fiber designs in order to achieve more than octave-spanning SCs while suppressing soliton fission and maintaining a single pulse in the time domain. The conditions for optimizing the spectral flatness are investigated in detail, and the development of special fibers exhibiting normal dispersion at all wavelengths prevents MI entirely. This allows the use of pump pulses with several hundred femtoseconds duration without degradation of the coherence properties. The numerical results are confirmed by experiments and applications in transient absorption spectroscopy and few-cycle pulse compression show the enormous potential of this novel SC type.

3. Numerical modelling of ultrashort pulse propagation in optical fibers

The numerical modelling of ultrashort nonlinear pulse propagation in optical fibers plays an important role in a variety of applications and research areas. The approach of describing the evolution of the pulse envelope leads to a nonlinear Schrödinger equation (NLSE), which has been extensively used to simulate optical fiber communication systems. It describes the effects of second order dispersion and SPM and has proven very successful to simulate the propagation of low power pulses with durations of a few picoseconds through optical fiber networks. In the case of supercontinuum generation by femtosecond pulses with high peak powers and high nonlinearities, however, higher order dispersive and nonlinear processes have to be included, resulting in a generalized NLSE (GNLSE) [48]. Both NLSE and GNLSE are reviewed in the first part of this chapter.

Numerical modelling based on the GNLSE is used extensively in this thesis for analyzing the underlying physics of the complex supercontinuum generation process, facilitating the design of fibers for coherent supercontinuum generation and tailoring of the continuum properties to specific applications such as time-resolved spectroscopy and ultrashort pulse compression. Since the numerical computation of solutions for the GNLSE can be time consuming, fast algorithms are required. The two key ingredients for an efficient implementation are

- an accurate numerical integration scheme and
- an intelligent control of the longitudinal spatial step size.

While highly efficient numerical integration schemes adapted to the requirements of the GNLSE are available, which are discussed in section 3.2, adaptive step size methods were simply transferred to GNLSE calculations from standard partial differential equation solvers, which leave room for improvement. Therefore, the conservation quantity error method (CQEM) was developed in this project as a highly efficient adaptive step size method, which is specifically designed for the GNLSE and its associated integration schemes. The CQEM is explained in detail in section 3.3.2 for the example of the GNLSE and the findings are transferred to the NLSE and extended to include linear loss. Finally, in section 3.3.3 the performance of the CQEM is evaluated in combination with two different integration schemes and compared to the established local error method (LEM).

Parts of this chapter were published in [57].

3.1. Nonlinear Pulse Propagation Equations

The electric field of an electromagnetic pulse, linearly polarized along the x-axis, can be defined as [41]

$$\vec{E_N}(\vec{r},t) = \frac{1}{2}\vec{x}\left\{E_N(x,y,z,t)\exp(-i\omega_0 t) + c.c.\right\}. \tag{3.1}$$

Here $\vec{x}$ is the unit vector in x-direction. $\vec{E_N}$ is scaled to the actual electric field $\vec{E}$ in units of V/m by

$$\vec{E_N} = \sqrt{\frac{1}{2}\epsilon_0 cn}\,\vec{E}, \tag{3.2}$$

where ϵ_0 is the vacuum permittivity, c the speed of light and n the refractive index. In the frequency domain, the Fourier transform of $E_N(x,y,z,t)$ is

$$\tilde{E}_N(x,y,z,\omega) = F(x,y,\omega)\tilde{A}(z,\omega-\omega_0)\exp(i\beta_0 z), \tag{3.3}$$

where $\tilde{A}(z,\omega)$ is the complex spectral envelope, ω_0 is the center frequency of the pulse and β_0 the wavenumber at that frequency. $F(x,y,\omega)$ is the unit-less transverse modal distribution with effective mode field area

$$A_{\text{eff}}(\omega) = \frac{\left(\iint_{-\infty}^{\infty}|F(x,y,\omega)|^2\mathrm{d}x\mathrm{d}y\right)^2}{\iint_{-\infty}^{\infty}|F(x,y,\omega)|^4\mathrm{d}x\mathrm{d}y}. \tag{3.4}$$

The time-domain envelope is obtained from

$$A(z,t) = \mathcal{F}^{-1}\left\{\tilde{A}(z,\omega-\omega_0)\right\} = \frac{1}{2\pi}\int_{\infty}^{\infty}\tilde{A}(z,\omega-\omega_0)\exp[-i(\omega-\omega_0)t]d\omega, \tag{3.5}$$

where due to the scaling in (3.2) the amplitude is normalized such that $|A(z,t)|^2$ yields the instantaneous power in Watts and $\mathcal{F}^{-1}$ denotes the inverse Fourier transform. The change of the pulse envelope A as the pulse propagates along the fiber axis z can then generally be expressed as

$$\frac{\partial A(z,T)}{\partial z} = \left(\hat{D}+\hat{N}\right)A(z,T), \tag{3.6}$$

where $T = t - \beta_1 z$ is the retarded time for a frame of reference travelling at the envelope group velocity $v_g = \beta_1^{-1}$, $\hat{D}$ is the dispersion operator and $\hat{N}$ is the nonlinear operator [48].

3.1.1. Nonlinear Schrödinger equation

The NLSE describes the propagation of optical pulses with durations in the picosecond regime in the presence of second order dispersion and SPM, so that the operators in (3.6)

are given by

$$\begin{aligned} \hat{D} &= -i\frac{\beta_2}{2}\frac{\partial^2}{\partial T^2} - \frac{\alpha}{2}, \\ \hat{N} &= i\gamma|A|^2, \end{aligned} \tag{3.7}$$

where β_2 is the second order dispersion parameter, α is the absorption coefficient and $\gamma = n_2\omega_0/cA_{\text{eff}}(\omega_0)$ is the nonlinear coefficient, with $n_2 \simeq 3.0\times10^{-20}$ m^2/W the nonlinear refractive index of silica and $A_{\text{eff}}(\omega_0)$ the effective mode field area of the fiber, evaluated at the center angular frequency of the pulse [48].

3.1.2. Generalized nonlinear Schrödinger equation

In order to obtain the GNLSE, higher order dispersive and nonlinear effects are explicitly included. A version that is widely used for the numerical simulation of supercontinuum generation defines the operators in (3.6) as [58]:

$$\begin{aligned} \hat{D} &= -\frac{\alpha}{2} - \sum_{n\geq 2}\beta_n\frac{i^{n-1}}{n!}\frac{\partial^n}{\partial T^n}, \\ \hat{N}A(z,T) &= i\gamma\left(1 + i\tau_{\text{shock}}\frac{\partial}{\partial T}\right) \\ &\quad\times\left[A(z,T)\left(\int_{-\infty}^{\infty}R(t')|A(z,T-t')|^2\mathrm{d}t' + i\Gamma(z,T)\right)\right]. \end{aligned} \tag{3.8}$$

$\hat{D}$ models linear loss and higher order dispersion effects with the dispersion coefficients β_n associated with the Taylor series expansion of the propagation constant $\beta(\omega)$ around the center frequency ω_0. The time derivative in the nonlinear operator includes the effects of self-steepening and optical shock formation, characterized on a time scale $\tau_{\text{shock}} = 1/\omega_0$. The response function $R(t) = (1 - f_R)\delta(t) + f_R h_R(t)$ contains both instantaneous and delayed Raman contributions, where $\delta(t)$ is the Dirac delta function and $f_R = 0.18$ representing the fractional contribution of the delayed Raman response. For the Raman response function of silica fiber $h_R(t)$, the analytical expression

$$h_R(t) = \frac{\tau_1^2 + \tau_2^2}{\tau_1\tau_2^2}\exp(-t/\tau_2)\sin(t/\tau_1)\Theta(t) \tag{3.9}$$

introduced in [59] is used, with $\tau_1 = 12.2$ fs, $\tau_2 = 32$ fs and the Heaviside step function $\Theta(t)$.

Inclusion of noise

Noise is included into the simulations in order to investigate the temporal coherence properties. Γ models the effect of spontaneous Raman scattering with the frequency

domain correlations given by

$$\langle \Gamma(z,\Omega)\Gamma^*(z',\Omega')\rangle = \frac{2f_R\hbar\omega_0}{\gamma}\,|\mathrm{Im}[h_R(\Omega)]|\,[n_{th}(|\Omega|)+\Theta(-\Omega)]\delta(z-z')\delta(\Omega-\Omega'), \quad (3.10)$$

with $\Omega = \omega - \omega_0$ and $n_{th}(\Omega) = [\exp(\hbar\Omega/k_BT)-1]^{-1}$ the thermal Bose distribution [60]. Input pulse shot noise is modelled semi-classically by the addition of one photon per mode with random phase on each spectral discretization bin (see appendix A.5). The noise sensitivity of the generated spectra is then characterized by calculating the modulus of the complex degree of first-order coherence at each wavelength [22]

$$\left|g_{12}^{(1)}(\lambda, t_1 - t_2)\right| = \left|\frac{\langle E_1^*(\lambda,t_1)E_2(\lambda,t_2)\rangle}{\sqrt{\langle|E_1(\lambda,t_1)|^2\rangle\langle|E_2(\lambda,t_2)|^2\rangle}}\right|. \quad (3.11)$$

Angular brackets indicate an ensemble average over independently generated pairs of SC spectra and t is the time measured at the scale of the temporal resolution of the spectrometer used to resolve these spectra. In order to focus on the wavelength dependence of the coherence, $|g_{12}^{(1)}|(\lambda)$ at $t_1 - t_2 = 0$ is used. In this thesis, 20 independent spectra with random noise seeds are simulated resulting in 190 unique pairs, which are sufficient for the calculation of the ensemble average. At each wavelength bin, (3.11) gives a positive number in the interval [0;1] with the value 1 representing perfect coherence. Spontaneous Raman noise and input pulse shot noise are only considered where coherence properties are calculated, while in all other simulations $\Gamma = 0$.

Frequency domain formulation

Although versions of the GNLSE have been derived in both time and frequency domain, the time domain formulation presented above is most often found in literature. However, from the perspective of numerical efficiency and accuracy, a frequency domain formulation offers several advantages:

- The time domain formulation (3.8) contains several time derivatives, which can only be calculated approximately in the discrete numerical case with a finite number of sample points and therefore lead to numerical errors. These derivatives vanish when the equation is transformed into the frequency domain due to the Fourier transform replacement property $\partial/\partial t \leftrightarrow -i(\omega - \omega_0)$. Therefore, both dispersive and nonlinear operators can be applied in an approximation-free manner. The frequency domain formulation is therefore fundamentally more accurate than the time domain formulation.

- It is possible to directly include the frequency dependence of effects such as linear loss and effective mode field area, which are usually neglected in the time domain.

- The convolution in $\hat{N}$ in (3.8) is transformed into a simple multiplication in the frequency domain using the Fourier convolution theorem $\mathcal{F}(\int_{-\infty}^{\infty} A(\tau)B(t-\tau)\mathrm{d}\tau) = \tilde{A}(\omega)\tilde{B}(\omega)$, which takes significantly less computational time to compute.

When transformed into the frequency domain, the GNLSE can be written as [61]

$$\begin{aligned}\frac{\partial \tilde{A}(z,\omega)}{\partial z} &= \left(\hat{D}(\omega)+\hat{N}(z,\omega)\right)\tilde{A}(z,\omega),\\ \hat{D}(\omega) &= -\frac{\alpha(\omega)}{2}+i(\beta(\omega)-\beta_1(\omega-\omega_0)-\beta(\omega_0)),\\ \hat{N}(z,\omega)\tilde{A}(z,\omega) &= i\gamma\left(1+\frac{\omega-\omega_0}{\omega_0}\right)\\ &\quad\times\mathcal{F}\left\{A(z,T)\left[\mathcal{F}^{-1}\left(\tilde{R}(\omega)\mathcal{F}\left(|A(z,T)|^2\right)\right)+i\Gamma(z,T)\right]\right\}. \end{aligned} \tag{3.12}$$

Here $\tilde{R}(\omega)$ is the Fourier transform of the Raman response function $R(t)$. Due to the stated advantages, this version of the GNLSE is implemented for the calculations in this thesis.

Dispersion of the nonlinearity

The dispersion or frequency dependence of the nonlinearity is responsible for effects such as self-steepening and optical shock formation, characterized on a time scale of τ_{shock} and modelled in the time domain formulation of the GNLSE (3.8) by the derivative term in $\hat{N}$ or by the fraction $(\omega-\omega_0)/\omega_0$ in the frequency domain formulation (3.12). Additional dispersion of the nonlinearity results from the frequency dependence of the effective mode field area $A_{\text{eff}}(\omega)$(3.4), which is included in the nonlinear parameter

$$\gamma(\omega)=\frac{n_2\omega_0}{cA_{\text{eff}}(\omega)}. \tag{3.13}$$

It has been shown that this frequency dependence can be included in the time domain version of the GNLSE in an approximative manner by a first-order correction to τ_{shock} [58]. In the frequency domain (3.12), $\gamma(\omega)$ can be included explicitly. However, it was demonstrated in [62] that this is also only an approximative treatment as the GNLSE was derived under the assumption of constant γ. Instead, a new version of the GNLSE can be derived which treats the frequency dependence of A_{eff} rigorously. This new version makes the replacement $\tilde{A}(z,\omega)\rightarrow\tilde{C}(z,\omega)$ in (3.12) and defines a new nonlinear parameter $\bar{\gamma}(\omega)$

$$\begin{aligned}\tilde{C}(z,\omega) &= \left[\frac{A_{\text{eff}}(\omega)}{A_{\text{eff}}(\omega_0)}\right]^{-1/4}\tilde{A}(z,\omega),\\ \bar{\gamma}(\omega) &= \frac{n_2 n_{\text{eff}}(\omega_0)\omega_0}{cn_{\text{eff}}(\omega)\sqrt{A_{\text{eff}}(\omega)A_{\text{eff}}(\omega_0)}}, \end{aligned} \tag{3.14}$$

where n_{eff} is the effective refractive index of the guided mode [41, 62].

3.1.3. Limits to validity

The pulse propagation equations presented in this chapter have their origin in the interaction of an electromagnetic pulse with a nonlinear medium and therefore are derived from Maxwell's equations including a nonlinear polarization term. From these a second-

order wave equations can be derived which is then approximated to the first-order NLSE or GNLSE equations. Since they can affect the applicability and validity of the derived equations, it is important to list the key assumptions made in the derivation of the GNLSE (3.12):

1. The propagation is assumed to be unidirectional. Any backward propagating waves and any coupling between backward and forward propagating waves are neglected.

2. The pulse is assumed to propagate in a single transverse mode (usually the fundamental mode) of the fiber (see (3.3)). A multimode version of the GNLSE, which also accounts for coupling between the modes, has been derived in [63], but the calculations tend to be very complex.

3. The derivation is purely scalar, i.e. the vectorial character of the electric field is ignored. Typically a polarization maintaining fiber pumped along a single polarization axis is assumed. Effects such as polarization mode dispersion and coupling between light propagating along two different polarization axes are neglected. However, coupled propagation equations describing polarization effects as well as a vectorially-based nonlinear Schrödinger equation, which also takes refractive index inhomogenities and the longitudinal field component of the propagating mode in strongly guiding waveguides into account, are available in literature [64, 65].

It is often assumed that the decomposition of the electromagnetic pulse into an envelope and a carrier wave necessarily leads to the fact that the envelope needs to be slowly varying. This would imply that the equation for the evolution of the pulse envelope becomes invalid when the pulse duration approaches a single field oscillation period. However, it has been shown that envelope-based equations can remain valid down to the single optical cycle limit [66, 67]. Also in this thesis it will be demonstrated that the GNLSE delivers results in excellent agreement with experiments down to the sub-two optical cycle regime.

3.2. Numerical Implementation

In literature, the numerical solution of NLSE and GNLSE has widely been carried out using the symmetric split-step Fourier method (SSFM) in connection with a fourth order Runge-Kutta solver for the nonlinear step [68]. The SSFM finds an approximate solution to the general pulse propagation equation in time (3.6) or frequency (3.12) formulation by assuming that dispersive and nonlinear operator act independently and consecutively, while in reality they act simultaneously. When the algorithm propagates the pulse envelope longitudinally along the fiber axis from a position z to a new position $z + h$, a numerical error is introduced, because the SSFM ignores the non-commuting nature of the operators $\hat{D}$ and $\hat{N}$. In an analysis using the Baker-Hausdorff formula for two non-commuting operators, it can be shown that the dominant error term per step is of order $O(h^3)$ [48]. Note that the total number of steps is inversely proportional to h, so that the

global error at the end of the simulation is $O(h^2)$. The algorithm advancing the spectral envelope is detailed in appendix A.1.

Recently, the Runge-Kutta in the interaction picture method (RK4IPM) was applied to the simulation of nonlinear pulse propagation and supercontinuum generation in optical fibers [69]. This method was originally developed for the solution of the Gross-Pitaevskii equation which describes the dynamics of Bose-Einstein condensates. It transforms the pulse propagation equation into an interaction picture in order to separate the dispersive terms in $\hat{D}$ from the non-dispersive terms in $\hat{N}$. The RK4IPM is closely related to the SSFM and exhibits a fifth order local accuracy, while it is as easy to implement as the less accurate SSFM [70]. While both SSFM and RK4IPM are used in this chapter to investigate how the accuracy of the integration algorithm effects the performance of the adaptive step size control, only the RK4IPM will be applied in the subsequent chapters due to its higher accuracy. The exact algorithm is detailed in appendix A.2.

The computationally most expensive operation in both methods is the Fourier transform, and both integration methods require a total of 16 Fourier transforms per step. The main advantage of the RK4IP is the high accuracy of the integration with a dominant local error term of order $O(h^5)$, making it possible to set h much larger to reach the same accuracy and therefore making the calculation significantly faster than the SSFM.

3.3. Adaptive step size algorithms

The accuracy of a given integration method depends on the resolution of the time (or frequency) window and on the longitudinal step size. The time domain resolution is usually chosen according to the maximum bandwidth of the signal during propagation and the available discretization bins, which are limited by the memory of the computer and the acceptable computational time. The time and frequency domain resolutions therefore depend on the properties of signal and computer and are not varied during the simulation. The longitudinal step size h, however, does not have to be constant and can be adjusted. If nonlinearities are low, h can be increased, because the error in splitting dispersive and nonlinear processes is negligible. If both dispersion and nonlinearity are significant, a smaller step size is required. Since the balance between dispersion and nonlinearity can change during propagation, e.g. due to decreasing peak power and broadening of the pulse, an algorithm is required to estimate the current local error and to adapt h accordingly.

Various adaptive step size methods have been introduced in literature, including the nonlinear phase rotation, logarithmic step size and walk-off methods [71]. Sinkin. et. al. tested the performance of these methods in a systems context and introduced the local error method (LEM), which was also found to be the most efficient [72]. Unlike the other methods, which were introduced for the NLSE, the LEM can also be employed when simulating broadband supercontinuum generation with the GNLSE in connection with both SSF and RK4IP integration schemes [25, 15]. The LEM applies the techniques of step size doubling and local extrapolation, which are widely used in partial differential

equation solvers. Step size doubling implies that each step is taken twice, once as a full step to compute a coarse solution and then independently as two half steps resulting in a fine solution. The difference between the two results yields an estimation of the local error. In addition, a higher order solution is obtained with this method. However, the LEM requires 50% more Fourier transforms than the standard integration scheme. While computational speed is gained by the adaption of the step size, it is lost by the necessity of computing coarse and fine solutions.

In this section, an enhancement of the local error method is introduced which was specifically designed for the use with higher order integration algorithms such as the RK4IPM. The estimation of the local error is obtained from a conservation quantity error (CQE) without the necessity of step size doubling. In case of the GNLSE, the conservation quantity is proportional to the classical photon number, while the NLSE conserves the pulse energy. It is demonstrated that the CQE method increases the computational efficiency by up to $\sim 50\%$ relative to the original LEM when the RK4IP scheme is used for integration.

3.3.1. Review of the Local Error Method

Generally, using an integration method with local error of order η, and given the field A at a distance z, which is discretized into N temporal gridpoints, there exists a constant k for each gridpoint so that the calculated field at $z + h$ can be expressed as

$$A_{\text{calc}}(z + h, T) = A_{\text{true}}(z + h, T) + k(T)h^{\eta} + O(h^{\eta+1}), \tag{3.15}$$

where A_{true} is the exact solution. Here $\eta = 3$ for the SSFM and $\eta = 5$ for the RK4IPM. The relative local amplitude error is now defined as

$$\delta_A(h) = \frac{\parallel A_{\text{calc}} - A_{\text{true}} \parallel}{\parallel A_{\text{true}} \parallel}. \tag{3.16}$$

Here the norm $\parallel A \parallel = (\int \mid A(T) \mid^2 \mathrm{d}T)^{1/2}$ is used. The error of each calculated step is thus explicitly dependent on a power of the step size h^{η}. This dependence can be used to limit the error to a predefined goal error δ_G by adjusting h. However, the true local error can generally not be computed, because A_{true} is unknown. Therefore, the algorithm tries to estimate the local error by taking a full step to compute a coarse solution and then independently taking two half steps resulting in a fine solution . The true local error δ_A from (3.16) can then be approximated by

$$\delta = \frac{\parallel A_{\text{fine}} - A_{\text{coarse}} \parallel}{\parallel A_{\text{fine}} \parallel}. \tag{3.17}$$

The step size h is adaptively adjusted with the aim to keep δ in the range $(\delta_G, 2\delta_G)$, where δ_G is the predefined acceptable error (goal error). If $\delta > 2\delta_G$, the solution is discarded and the step is repeated with half the step size. If δ is in the range $(\delta_G, 2\delta_G)$, h is divided by $2^{(1/\eta)}$ for the next step. If $\delta < 1/2\delta_G$, and h is multiplied by $2^{(1/\eta)}$ for

the next step.

An additional advantage of the local error method is the possibility to construct a higher order solution $A_{\eta+1}$ from an appropriate linear combination of coarse and fine solution

$$\begin{aligned} A_{\eta+1} &= \frac{2^{\eta-1}}{2^{\eta-1}-1}A_{\text{fine}} - \frac{1}{2^{\eta-1}-1}A_{\text{coarse}}, \\ &= A_{\text{true}} + O(h^{\eta+1}). \end{aligned} \tag{3.18}$$

Local extrapolation consists of accepting the higher order solution $A_{\eta+1}$, even though the error estimate δ applies strictly only to A_{coarse}. Note that $A_{\eta+1}$ converges asymptotically towards A_{fine} for increasing η, so that the advantage of local extrapolation decreases for highly accurate integration schemes.

3.3.2. Introduction of the Conservation Quantity Error Method

The LEM assumes that no information is available about the true solution and thus requires the computation of both coarse and fine solutions to estimate the local amplitude error, creating an overhead of 50% more Fourier transforms in comparison to the standard integration without step size adaption. Since no assumption is made about the system, the LEM may be applied to a variety of problems. However, in the specific case of the GNLSE there is additional information available about the true solution which can be used to improve the efficiency of the adaptive step size algorithm.

If loss in the fiber is neglected, Blow and Wood showed that the GNLSE conserves the optical photon number P during propagation,

$$\begin{aligned} \frac{\partial P}{\partial z} &= \frac{\partial}{\partial z}\left[\int \pi(z,\omega)\,\mathrm{d}\omega\right] \\ &= \frac{\partial}{\partial z}\left[\int S(\omega)\,\frac{\mid \tilde{A}(z,\omega)\mid^2}{\omega}\mathrm{d}\omega\right] \\ &= 0, \end{aligned} \tag{3.19}$$

where $\pi(z,\omega)$ is the spectral photon density, $\tilde{A}(z,\omega)$ is the Fourier transform of $A(z,T)$ and $S(\omega) = n_{\text{eff}}(\omega)A_{\text{eff}}(\omega)$ [58]. Note that different versions of the GNLSE may have a slightly different definition of the conserved quantity [62]. If the frequency dependence of both n_{eff} and A_{eff} is neglected, the term $S(\omega)$ can be taken out of the integral. P is then equivalent to the classical photon number in the optical wave.

Since the GNLSE conserves the photon number, the photon number $P(z)$ of the initial spectrum $\tilde{A}(z,\omega)$ is also the true value $P_{\text{true}}(z+h)$ of the photon number after one computational step,

$$P_{\text{true}}(z+h) = P(z). \tag{3.20}$$

It is therefore possible to calculate the absolute photon number error

$$\Delta_{\mathrm{Ph}} = |P_{\mathrm{calc}}(z+h) - P_{\mathrm{true}}(z+h)| \tag{3.21a}$$

$$= \left| \int \left(\mid \tilde{A}_{\mathrm{calc}}(z+h,\omega) \mid^2 - \mid \tilde{A}_{\mathrm{true}}(z+h,\omega) \mid^2 \right) \frac{S(\omega)}{\omega} \mathrm{d}\omega \right|, \tag{3.21b}$$

$$= \left| \int \left(\mid \tilde{A}_{\mathrm{calc}}(z+h,\omega) \mid^2 - \mid \tilde{A}(z,\omega) \mid^2 \right) \frac{S(\omega)}{\omega} \mathrm{d}\omega \right|, \tag{3.21c}$$

where $P_{\mathrm{calc}}(z+h)$ is the photon number calculated with the spectrum $\tilde{A}_{\mathrm{calc}}(z+h,\omega)$. In (3.21b), the definition of the photon number in (3.19) was inserted. (3.21c) makes additional use of the identity (3.20). In practice, Δ_{Ph} is simply calculated by taking the absolute difference between the photon numbers of two consecutive computational steps.

In order to relate Δ_{Ph} to the local error of the computational step, (3.15) is rewritten in the frequency domain and using intensities instead of amplitudes:

$$\mid \tilde{A}_{\mathrm{calc}} \mid^2 = \mid \tilde{A}_{\mathrm{true}} \mid^2 + \Delta_I(h,\omega), \tag{3.22}$$

where $\Delta_I(h,\omega) = k'(\omega)h^\eta + O(h^{\eta+1})$ is the absolute local intensity error of each frequency bin. Substituting (3.22) into (3.21b), one obtains

$$\Delta_{\mathrm{Ph}}(h) = \left| \int \Delta_I(h,\omega) \frac{S(\omega)}{\omega} \mathrm{d}\omega \right|. \tag{3.23}$$

The photon number error Δ_{Ph} is thus a measure of $\Delta_I(h,\omega)$, integrated over the frequency window and weighed by $S(\omega)/\omega$, which is merely a scaling factor. Thus an estimation of the true local error of A has been found, which can simply be computed by comparing the photon numbers of two consecutive steps. Further, the calculation of the photon number for each step is a simple integration over the frequency window and therefore does not create any overhead. Like the local error, the photon number error is proportional to h^η, so that it can be controlled by adjusting h. In an adaptive step size algorithm, it is useful to control a relative quantity, so Δ_{Ph} is normalized by P_{true} to define the relative photon error

$$\delta_{\mathrm{Ph}} = \frac{\Delta_{\mathrm{Ph}}}{P_{\mathrm{true}}}, \tag{3.24}$$

where (3.20) can be used for the actual calculation. The step size is then adjusted similar to the LEM. If $\delta_{\mathrm{Ph}} > 2\delta_G$, the solution is discarded and the step is repeated with half the step size. If δ_{Ph} is in the range $(\delta_G, 2\delta_G)$, h is divided by $2^{(1/\eta)}$ for the next step. If $\delta_{\mathrm{Ph}} < 0.1\delta_G$, the h is multiplied by $2^{(1/\eta)}$ for the next step.

It should be noted that $\Delta_I(h,\omega)$ in (3.23) can assume positive and negative values in each frequency bin which can cancel each other when integrated. The resulting δ_{Ph} may be small, even if there are substantial local errors present in the calculation. Especially for small scale errors, δ_{Ph} will underestimate the true local error, resulting in a tendency of the algorithm to set the value of h too high for the next step. Further, the method keeps the value of δ_{Ph} close to the predefined goal error δ_G. It was found in practice,

however, that in rare cases during the propagation the value for δ_{Ph} can drop close to zero and then recovers again to its original value close to δ_G. This effect can be attributed to a continuous sign change of the term in the modulus in (3.23), which could not be linked to any physical effect and appears to be a numerical issue. The result is a spiking of the step size which deteriorates the accuracy of the method. Both of the aforementioned problems are resolved by setting the threshold for the increase of the step size to the relatively low value of $0.1\delta_G$. This value was chosen in such a way that the spiking of the step size is suppressed to a large extent, while the method is still sufficiently sensitive to genuinely required increments of the step size. Further, it is expected that the performance of the algorithm improves in connection with highly accurate integration schemes, because the error introduced by the overestimated longitudinal step size decreases with higher order integration methods. Indeed, it is shown in the next section that the RK4IPM with $\eta = 5$ is required in order for the algorithm to work efficiently even for highly accurate solutions, the SSFM with $\eta = 3$ is generally not sufficient.

As mentioned above, the photon number conservation (3.19) is only valid in the absence of linear loss ($\alpha = 0$). However, linear loss can easily be included into the presented concept. Following the discussion in [58] leading to the deduction of (3.19), the photon number change in the presence of linear loss can be expressed as

$$\frac{\partial P}{\partial z} = -\int \alpha(\omega)\pi(z,\omega)\,\mathrm{d}\omega, \tag{3.25}$$

which can be calculated exactly. The true photon number at distance $z + h$ in (3.20) - (3.24) is modified to

$$P_{\mathrm{true}}(z+h) = P(z) + \frac{\partial P}{\partial z}h. \tag{3.26}$$

To complete the discussion, the concept of employing a conserved quantity in an adaptive step size algorithm can be extended to other equations as well. In the case of the NLSE, for example, the energy $E = \int \mid \tilde{A}(\omega) \mid^2 \mathrm{d}\omega$ is conserved if loss in the fiber is neglected. The above discussion for the photon number conservation can entirely be applied to the energy conservation in case of the NLSE. Defining an energy error Δ_E in a similar fashion to (3.21b) and inserting (3.22), one obtains

$$\Delta_{\mathrm{E}}(h) = \left| \int \Delta_I(h,\omega)\mathrm{d}\omega \right|. \tag{3.27}$$

The relation of the energy error to the local error Δ_I is thus even simpler than in the case of the GNLSE and the photon number error (3.23).

3.3.3. Performance

In this section, the performance of the adaptive step size algorithms described in section 3.3 are compared. For this purpose, a typical example of supercontinuum generation in photonic crystal fiber and a soliton collison are simulated using CQEM and LEM as well as a constant step size for comparison. Both RK4IPM and SSFM are employed

to determine if the accuracy of the integration scheme changes the performance of the adaptive step size methods. In the following, the combinations of RK4IPM with the CQEM, LEM and constant step size methods will be denoted as RK4IP-CQE, RK4IP-local and RK4IP-constant, respectively. Equivalent denotation is used when the SSFM is used for integration.

To compare the different methods, first a reference spectrum $\tilde{A}_{\mathrm{ref}}$ is computed at machine precision with the RK4IP-constant method using a step size smaller than the smallest step size chosen by the adaptive methods. Then the numerical solutions $\tilde{A}_{\mathrm{calc}}$ for the different methods are compared to the reference solution by calculating the global average relative intensity error

$$\epsilon = \frac{\int \left| \mid \tilde{A}_{\mathrm{calc}} \mid^2 - \mid \tilde{A}_{\mathrm{ref}} \mid^2 \right| \mathrm{d}\omega \, / N}{\int \mid \tilde{A}_{\mathrm{ref}} \mid^2 \mathrm{d}\omega}, \tag{3.28}$$

where N is the number of frequency gridpoints. ϵ is then plotted versus the total computational time, normalized by the time required to evaluate one FFT. The required error sensible for studying physical processes is typically $\epsilon \leq 10^{-5}$.

Supercontinuum Generation

Solutions of the GNLSE are computed for a typical broadband SC generation process in a highly nonlinear PCF structure, pumping in the anomalous dispersion regime. The parameters of the fiber and the input pulse are taken from [25] and are similar to those used in section 2.2. Loss in the fiber and frequency dependence of A_{eff} are neglected. The time and frequency windows were discretized into $N = 2^{13}$ bins and the reference spectrum was computed with a constant step size of ca. 30 nm.

Fig. 3.1 (a) and (b) illustrate the temporal and spectral evolution of the SC generation process over 10 cm length of PCF, while (c) and (d) show the error estimations of the LEM, (3.17), and the CQEM, (3.24), when the simulation is run with a relatively large constant step size of 40 μm and the error estimations between two consecutive computational steps are recorded over the propagation distance. It is evident that the largest errors occur in the range of the most extreme spectral broadening due to soliton fission between 0.7 - 1.5 cm. After ca. 2 cm, the broadening of the spectrum is essentially concluded, only the Raman-induced self-frequency shift of the highest peak power soliton extends the spectrum further into the infrared. Hence, the numerical errors are much smaller in this section and assume a minimum at around 5 cm, before a slight increase of errors is recorded for the remaining propagation distance due to continuing broadening and increasing complexity of the temporal pulse profile. The error estimation of the CQEM is generally about three to four orders of magnitude smaller than the one of the LEM. However, only the relative variation of the error estimation is important, because the absolute values can be set by adjusting the local goal error δ_G. The similarity of the graphs in Figs. 3.1 (c) and (d), on both large and small scales, confirms that the CQEM indeed gives an error estimation comparable to the one of the LEM. It should

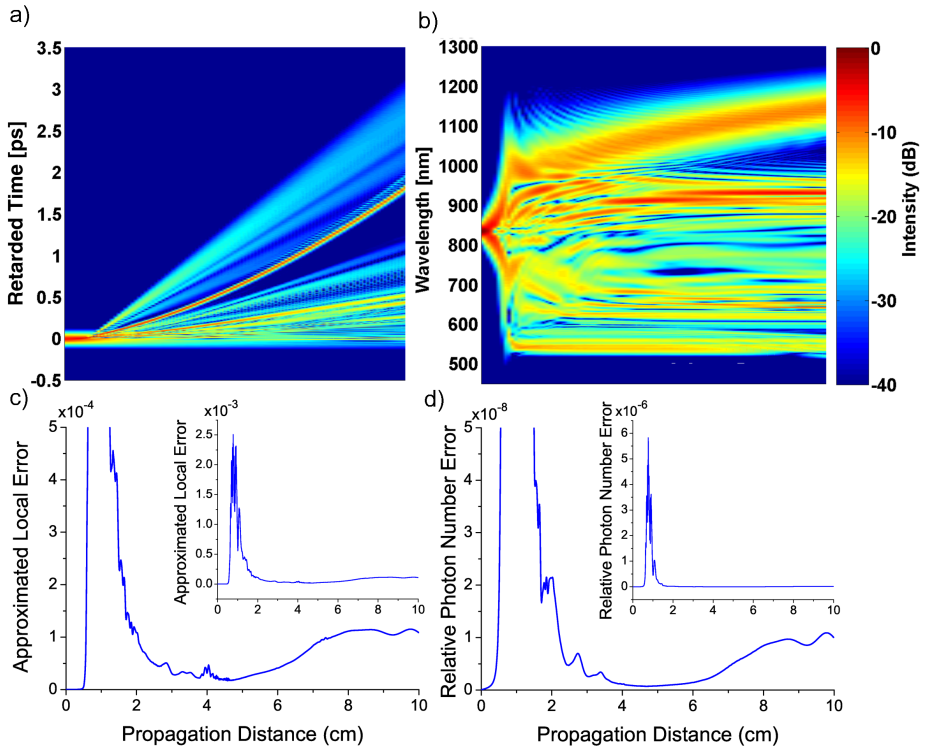

Figure 3.1. – Results from numerical simulation of supercontinuum generation in PCF, showing (a) temporal and (b) spectral evolution of the pulse over the propagation distance of 10 cm. In (c) and (d) the error estimations between two consecutive computational steps are plotted for the LEM and CQEM method, when the simulation is run with a constant step size of 40 μm. The inlays show the complete graphs, while the main figures focus on an enlarged section to compare the small scale errors. Error estimations and temporal and spectral evolutions are depicted with the same x-axis to facilitate the comparison of the graphs.

however be noted that the ratio of the small scale errors to the maximum recorded errors is smaller for the CQE method than for the local error method, indicating that the CQE method slightly underestimates the small scale errors, as is expected from the discussion in section 3.3.2.

In order to compare the computational performance, the local goal error is varied and ϵ is recorded as a function of computational time for each method. Typical values for δ_G are in the range $[10^{-1}, 10^{-10}]$ for the LEM and $[10^{-4}, 10^{-14}]$ for the CQEM. The starting values of the step size were chosen by the algorithms, i.e. the initial step size was set to a high level so that it would be rejected and accordingly adjusted by the algorithms. The results are given in Fig. 3.2, where the performance of constant step sizes is also plotted for comparison. Machine precision is reached at $\epsilon \approx 10^{-12}$.

When the SSFM is employed for integration, the different step size methods generally achieve similar results. For low accuracies $\epsilon \geq 10^{-7}$, the CQEM is the most effi-

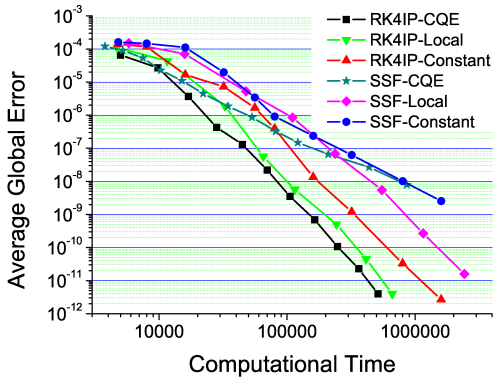

Figure 3.2. – Global average error ϵ plotted against computational time, normalized by the time required to evaluate one FFT, for the supercontinuum generation process in PCF.

cient and partially even outperforms the higher order RK4IPM using constant step size. However, due to the discussed underestimation of small scale errors the CQEM is not efficient for computing highly accurate solutions and converges towards the results of the SSF-constant method. The local extrapolation of the SSF-local method in (3.18) is advantageous only for highly accurate solutions with $\epsilon \leq 10^{-7}$, where it clearly separates from the other SSF schemes, while it achieves similar performance to the SSF-constant method for lower accuracies. Examining the slopes of the curves, the SSF-local method generally reaches third order global accuracy which is even improved to fourth order for $\epsilon \leq 10^{-8}$, while the CQEM and constant step size methods achieve only the expected second order precision.

Due to the higher order accuracy, the step size methods using the RK4IP scheme follow an overall more efficient trend than the methods using the SSF integration scheme, which is especially evident from the performance for $\epsilon \leq 10^{-6}$. In this case, the advantage of the local extrapolation applied by the LEM is only marginal and all RK4IP methods exhibit approximately fourth-order global accuracy.

As expected, the underestimation of small scale errors by the CQE method is compensated by the high precision of the RK4IPM, making the RK4IP-CQE combination the most efficient of all tested methods over the complete accuracy range tested. It requires only about 30% of the computational time needed by the constant step size algorithm to reach equal global accuracies. The achieved performance increase relative to the RK4IP-local method ranges between 25 - 40 %. Calculations for a range of different fiber designs and input pulse parameters were conducted and the CQE method was always the more efficient algorithm, with increasing efficiency improvement for more complex problems (e.g. increasing soliton number of the input pulse).

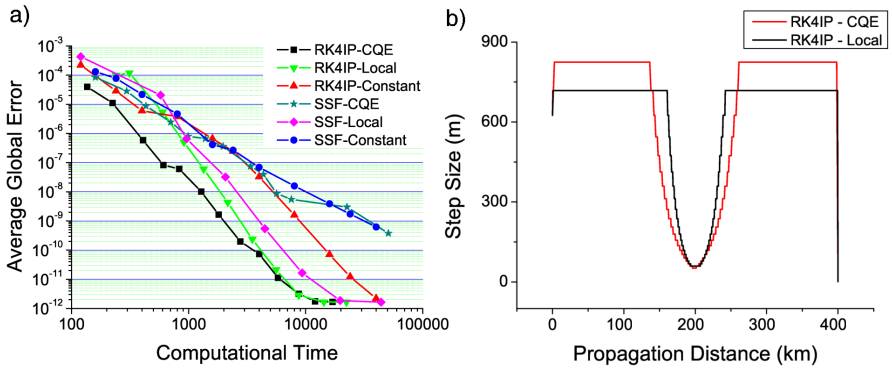

Figure 3.3. – (a) Global average error ϵ plotted against computational time for the collision of two fundamental solitons. (b) Step size chosen by the CQEM and LEM in combination with the RK4IPM. The achieved global accuracy and the required computational time are identical for both methods ($\epsilon \approx 3 \times 10^{-12}$, ca. 8500 FFTs).

Soliton Collision

In this section, the applicability of the CQEM to the NLSE is investigated. In this case, the appropriate conservation quantity is the pulse energy, as discussed towards the end of section 3.3.2. It has been shown that a large constant longitudinal step size in the SSFM can lead to the generation of spurious spectral peaks which are numerical artefacts and can be seen as fictitious four-wave mixing (FWM) [71]. A soliton collision is therefore used as the test scenario, because the cancellation of this spurious four-wave mixing after the collision is very sensitive to numerical errors. Two solitons, separated by 100 ps and a central frequency difference of 800 GHz, are launched into a fiber with anomalous dispersion $\beta_2 = -0.1\text{ps}^2/\text{km}$. The pulse parameters are $P_0 = 8.8$ mW and $T_0 = 2.27$ ps, corresponding to fundamental solitons with intensity FWHM of 4 ps. $N = 3072$ discretization bins are used and the propagation is observed over a distance of 400 km. The parameters are identical to those used by Sinkin et. al. [72].

Fig. 3.3 (a) shows the computational performance of the tested numerical methods. When the SSFM is used, the SSF-local method is most efficient and the calculation of a higher order solution in (3.18) proves to be effective for this simpler problem, which is evident from the steeper slope of the curve compared to the other SSF-methods. It achieves fourth order global accuracy and even higher efficiency than the RK4IP-constant method, thus outperforming an higher order integration scheme. The SSF-CQE method offers almost no improvement compared to the SSF-constant method, both show second order global accuracy.

In combination with the RK4IP integration scheme, the CQEM proves to be most efficient, reaching equal accuracies up to 45% faster than the local error method in the range $\epsilon \simeq 10^{-6} - 10^{-7}$. The two methods converge just before machine precision is reached at $\epsilon \approx 10^{-12}$. The RK4IP-local method achieves the expected fifth-order global

accuracy due to effective local extrapolation, while the other RK4IP methods show a fourth-order trend. The RK4IP-CQE is again the most efficient of all tested methods, which shows that the concept of applying a conserved quantity for adaptive step size control can also be successfully transferred to the numerical calculation of the NLSE.

The above mentioned numerical artefact of spurious FWM could be observed for solutions with $\epsilon \geq 10^{-7}$, with increasing spectral side peaks for larger ϵ. It can clearly be seen that all the adaptive step size schemes, with exception of the SSF-CQE, cross this boundary significantly earlier than the methods employing constant step size. In fact, the RK4IP-CQE reaches the necessary accuracy for eliminating spurious FWM almost one order of magnitude faster than the RK4IP-constant method.

Finally, a typical example of the functionality of the adaptive step size methods is shown in Fig. 3.3 (b). The step size is plotted versus the propagation distance for the RK4IP-CQE and RK4IP-local combinations, with both equal accuracy ($\epsilon \approx 3 \times 10^{-12}$) and required computational time ($\sim$ 8500 FFTs). The general shapes of the graphs are similar: after the algorithm finds a constant step size during the first few steps and retains it while the two pulses approach each other, the step size is significantly decreased around 200 km where the collision occurs; after the two pulses have crossed each other, the step size is restored to its original value. The graphs also illustrate the main difference between the two methods: the CQE method is less sensitive to the small scale errors outside the collision area and sets the step size accordingly higher than the local error method. In the collision area, however, the CQE is more sensitive, reacts earlier to the occurring errors and consequently models this region more accurately than the local error method. Both effects combined explain why the CQE method performs better for more complex problems, as was mentioned in section 3.3.3.

3.4. Summary

This chapter provided the details of the numerical model employed in this work to simulate ultrashort pulse propagation in optical fibers. It was shown that the GNLSE in the frequency domain formulation offers various advantages over the time domain formalism. The options to include the frequency dependence of A_{eff} and the validity limits of an envelope based scalar propagation were discussed.

An adaptive step size method based on a conservation quantity error was introduced for the numerical solution of NLSE and GNLSE. It is specifically designed for the use with an higher order integration algorithm like the RK4IPM and yields an estimation of the local error without the necessity of step size doubling. The performance of the CQEM was compared to the established LEM in combination with both SSFM and RK4IPM integration for the process of broadband supercontinuum generation and soliton collision. In both cases, the CQEM minimizes the computational effort if the RK4IPM is used for integration, while the original LEM performs best in connection with the SSFM integration, especially if highly accurate solutions are desired. The RK4IP-CQE combination is found to be the most efficient of all tested methods, with increasing

performance improvement for more complex problems. It is therefore especially suited for the fast and accurate modeling of supercontinuum generation in PCF.

A MATLAB® implementation of the RK4IP-CQE method was developed for the Free Optics Project in collaboration with A. Rieznik (Instituto Tecnológico de Buenos Aires) and is freely available for download [73]. After publication, the CQEM has been used by several authors for computationally intensive work, e.g. for studying the life cycle of optical rogue waves [74].

4. Design of photonic crystal fibers for coherent supercontinuum generation

This chapter presents an extensive survey of possible PCF designs for pulse-preserving and spectrally uniform broadband coherent SC generation. As explained in chapter 1, the transition region from fibers exhibiting a convex dispersion profile with two ZDWs to all-normal dispersion (ANDi) fibers appears to be especially suited to fulfill the optimization criteria.

Tremendous progress has been made recently in the development of ultrashort pulse fiber lasers, and femtosecond pulse energies well above 10 nJ and peak powers in excess of 200 kW are now readily available from Ytterbium doped fiber oscillators emitting in the vicinity of 1080 nm [75, 76, 77, 78]. With the longterm goal of developing a compact fiber-integrated coherent SC source, these fiber lasers present themselves as attractive pump sources.

This chapter focuses therefore on the numerical investigation of SC generation in PCF with two ZDWs and ANDi PCF with dispersion-flattened profiles near 1080 nm and considering femtosecond pulses with peak powers up to 270 kW. The influence of fiber design and input pulse parameters on the generated spectrum and resulting pulse profile is examined in detail, and design criteria are established to maximize temporal coherence, spectral bandwidth and uniformity as well as temporal recompressibility of the generated SC pulse.

Parts of this chapter were published in [79].

4.1. Numerical Method

In this study, PCF with solid core and hexagonal lattice of air holes are considered, with the geometrical design parameters pitch Λ and relative hole size d/Λ in the ranges Λ=1.45 - 1.70 μm and d/Λ = 0.3 - 0.43, leading to flattened dispersion profiles in the vicinity of 1080 nm. All fibers fulfill the condition for endlessly single-mode propagation [46]. For the optimization of the fiber design parameters, the SC generation process is first simulated for the different fiber designs with fixed input pulse parameters. The influence of the fiber design on the generated SC spectrum and the output pulse profile is then analyzed. Once an optimized fiber design has been found that fulfills the above stated criteria, the influence of varying input pulse parameters is investigated.

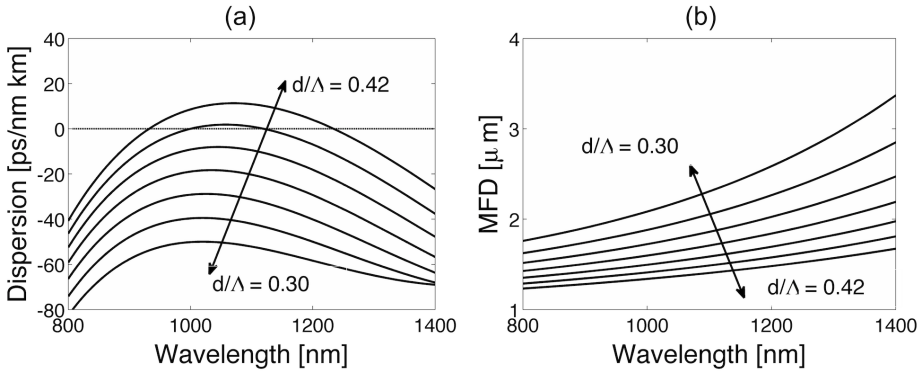

Figure 4.1. – Calculated dispersion parameter (a) and effective MFD (b) of PCF with Λ = 1.55 μm and values of d/Λ ranging between 0.3 and 0.42 in steps of 0.02.

The dispersion profile and effective mode field area of the investigated PCFs were generated with the analytical method devised in [47], after its validity over the investigated geometrical parameter range was confirmed by a numerical multipole mode solver [45]. Pulse propagation in the PCFs is simulated using the frequency formulation of the GNLSE (3.12), the RK4IPM (A.5) for integration as well as the CQEM (section 3.3.2) for the adaption of the longitudinal step size. Sufficient accuracy of the calculations was assured by setting the relative photon error $\delta_{\mathrm{Ph}} = 10^{-8}$ (3.24). Loss in the fiber is neglected. The frequency dependence of the effective mode field area A_{eff} is regarded in an approximate manner by including the frequency dependent nonlinear parameter $\gamma(\omega)$ (3.13) directly into the GNLSE. This treatment is sufficient here, because it has been carefully checked that the differences to the more rigorous method in (3.14) are marginal in the considered cases and do not affect the key findings in this chapter. For the investigation of temporal fine structure and pulse recompression, a time resolution of less than 1 fs is chosen in the calculation and the simulation window is divided into 2^{13} bins. Where average power values are given, a repetition rate of 80 MHz is assumed.

4.2. Influence of fiber parameters

In order to focus on the influence of fiber design on the SC generation process, the input pulse parameters are fixed in this section, while the fiber parameters are varied. A Gaussian input pulse shape with intensity full width at half maximum (FWHM) of 50 fs duration and pulse energy of 5 nJ is considered in this section. This corresponds to a peak power of 90 kW.

4.2.1. Relative air hole diameter d/Λ

First, a set of PCFs with common pitch Λ = 1.55 μm but different relative hole sizes between d/Λ=0.3 - 0.43 is considered. Fig. 4.1 shows a selection of corresponding calculated dispersion profiles and effective mode field diameters (MFD). The dispersion is normal

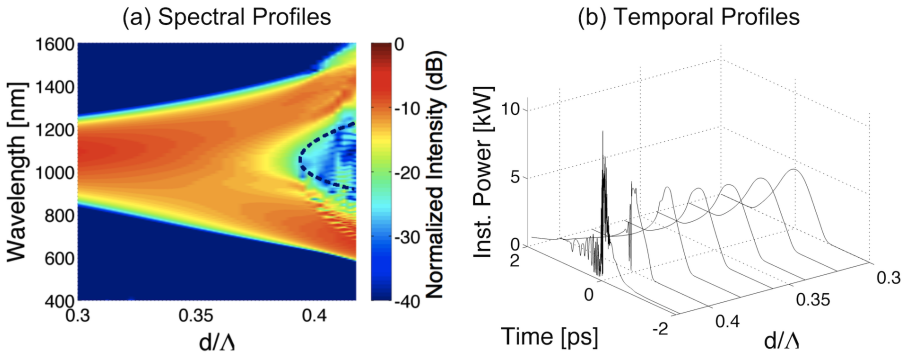

Figure 4.2. – (a) Dependence of the generated SC spectrum on the relative air hole diameter d/Λ in PCF with pitch Λ = 1.55 μm in a logarithmic density plot. An input pulse of 50 fs duration with 5 nJ energy propagating through a 10 cm piece of fiber is considered. The blue dotted line indicates the ZDWs: the dispersion is anomalous in the enclosed region and normal elsewhere. (b) Corresponding pulse profiles at the end of the fiber for selected d/Λ values in linear scale.

at all wavelengths for d/Λ ≤ 0.395, while above this value the dispersion is anomalous at the pump wavelength and two ZDWs with increasing separation for larger d/Λ exist. The effective mode field diameter generally decreases with shorter wavelengths and with increasing d/Λ values at a particular wavelength. Although a smaller mode field diameter leads to larger nonlinearity, the variations here are modest. The critical property distinguishing the different considered PCFs is therefore the dispersion profile, as it determines the physical effects participating in the SC generation process.

Fig. 4.2 a) shows the generated SC spectra in dependence of the d/Λ value of the fiber after 10 cm propagation of the pump pulse. The fiber length was chosen such that the spectra reach a steady state, i.e. there are no significant changes for further propagation beyond 10 cm. For this figure, 52 individual spectra were calculated and summarized in a logarithmic density plot which is truncated at -40 dB relative to the maximum intensity value. The dotted blue line indicates the position of the ZDWs, with the dispersion being anomalous inside this curve and normal elsewhere. Fig. 4.2 b) shows the corresponding pulse shapes at the end of the fiber. In the following, ANDi PCF with d/Λ ≤ 0.395 and PCF with two ZDWs will be analyzed separately.

For the fibers with two ZDWs, two distinct spectral parts are generated on the normal dispersion side of each ZDW, while the enclosed wavelength region of anomalous dispersion is almost completely depleted. The separation of the spectral peaks increases linearly with the separation of the ZDWs for larger d/Λ values. In the time domain, the peak power of the pulse at the end of the fiber is higher compared to the ANDi PCF due to partial compression in the anomalous dispersion. However, the pulse acquires a considerable modulation and an increasing tail with larger d/Λ values. The physics of SC generation in PCF with two closely spaced ZDWs has been studied in detail, and the

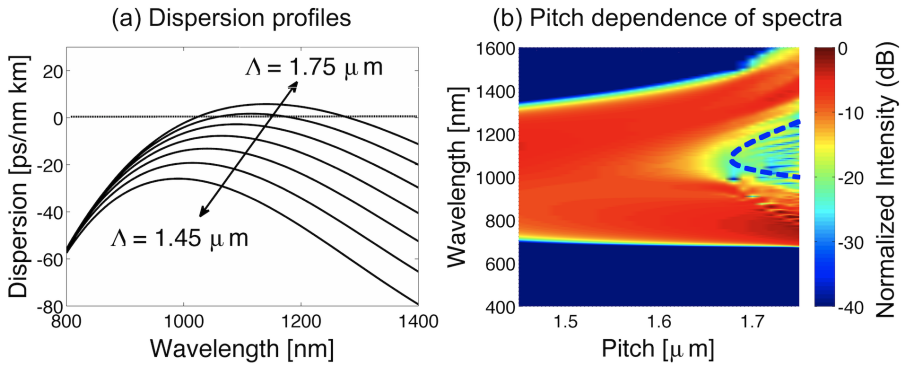

Figure 4.3. – (a) Calculated dispersion parameter of PCF with d/Λ=0.37 and selected pitch values in the range Λ=1.45 - 1.75 μm in 0.05 μm steps. (b) Dependence of the generated SC spectrum on fiber pitch in a logarithmic density plot. Input pulse parameters are identical to Fig. 4.2. The blue dotted line indicates the position of the ZDWs.

creation of the two distinct spectral parts has been attributed mainly to SPM [31]. Although this indicates good coherence properties of the generated spectrum and a smooth spectral phase [30], the missing spectral bandwidth in between the two spectral peaks and the modulation on the output pulse are not ideal for pulse compression. In addition, only the parts with high spectral power density are in practice useful for spectroscopy applications.

In the case of the ANDi PCF, the spectral bandwidth of the generated SC increases for larger d/Λ values as shown in Fig. 4.2. Comparison with Fig. 4.1 a) shows that increasing d/Λ corresponds to the dispersion profile essentially being shifted upwards, i.e. the normal group velocity dispersion (GVD) at the pump wavelength decreases. The spectra are continuous and smooth with steep edges and exhibit only minor intensity variations $<$ 3 dB over their bandwidth for d/Λ $<$ 0.37. A single pulse with clean and smooth profile is maintained in the time domain, which acquires an increasing asymmetry due to a longer trailing edge with increasing d/Λ. An analysis using spectrograms shows that this pulse tail contains predominantly blue wavelength components, so that the tail is a result of the increased spectral bandwidth towards the blue side. The pulse broadens considerably during its propagation, the intensity FWHM at the end of the fiber ranges between 1.07 ps for d/Λ=0.3 and 530 fs for d/Λ=0.39. It is interesting to note that the spectrum starts to split up and develop two distinct parts separated by a dip greater than 10 dB already for d/Λ $>$ 0.37, i.e. still in the all-normal dispersion regime as the peak dispersion of the fiber approaches zero. This spectral splitting is usually associated with PCF possessing two ZDWs, as was discussed above. The fiber with d/Λ = 0.37 offers the best compromise between spectral flatness and bandwidth. Since the dispersion is normal at all wavelengths, all the spectra are highly coherent over the entire bandwidth.

4.2.2. Pitch Λ

A set of PCF with pitch values between $\Lambda = 1.45$ μm and $\Lambda = 1.75$ μm and the common relative air hole diameter of $d/\Lambda = 0.37$ is considered. A selection of corresponding dispersion profiles is shown in Fig. 4.3 a). An ANDi profile exists for $\Lambda < 1.68$ μm. Similar to Fig. 4.2 a), Fig. 4.3 b) shows the dependence of the SC spectrum on the selected pitch value in a logarithmic density plot, summarizing 31 individual spectra. Again it is evident that the splitting of the spectrum into two distinct parts commences already in fibers with all-normal dispersion profiles. Smooth and continuous flat-top spectra exist for $\Lambda \leq 1.6$ μm, and in this region the pitch of the fiber has only negligible influence on the spectral shape and bandwidth.

4.2.3. Optimized fiber design

From the above discussion on the influence of the fiber design parameters on the generated SC pulse properties it can be concluded that the optimized fiber design has to to meet the following criteria:

- the fiber should exhibit normal dispersion at all wavelengths. This ensures smooth spectral and temporal profiles and suppresses soliton dynamics and MI gain entirely. The spectra can therefore be expected to be highly coherent;
- the maximum of the dispersion curve should be close to the pump wavelength to ensure minimum temporal spreading of the input pulse and maximum bandwidth;
- for maximizing spectral flatness: the maximum dispersion should be slightly normal, for the investigated input pulse parameters D $\leq$ -10 ps/(nm km);
- for maximizing spectral bandwidth: the maximum dispersion should be close to zero. However, this results in the formation of a depletion region around the maximum dispersion wavelength with a dip in spectral intensity larger than 10 dB.

In the investigated fiber design parameter range, there are several combinations that fulfill these criteria. Exemplary, in the following discussion the case Λ =1.55 μm, d/Λ = 0.37 is considered. Fig. 4.4 shows the simulated properties of the SC pulse for these parameters. On a logarithmic scale, the spectrum is almost rectangular with a smooth flat-top profile and steep edges. While the spectrum spans over one octave from 700 - 1400 nm, a constantly high average power density is achieved which never falls below 0.5 mW/nm and varies only about $\pm$ 1 dB from its mean value over the entire bandwidth. The top section of Fig 4.4 a) shows the modulus of the complex first-order degree of coherence at zero path difference $\left|g_{12}^{(1)}(\lambda, t_1 - t_2 = 0)\right|$ defined in (3.11), calculated from an ensemble average of 20 independent simulations with random noise seeds. It is evident that the spectrum is perfectly coherent over the entire generated bandwidth.

As shown already in Fig. 4.2 b), a single pulse with smooth profile is maintained in the time domain, which broadens to about 800 fs after 10 cm of propagation. The pulse predominantly acquires a linear chirp which can be compressed using a simple grating

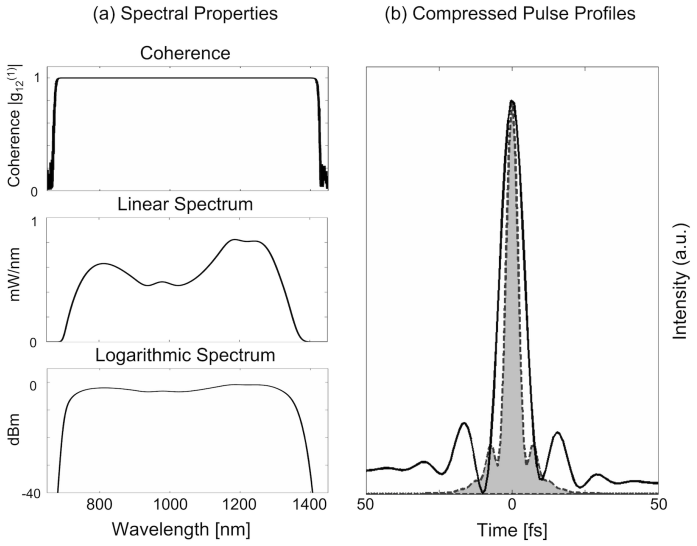

Figure 4.4. – (a) Spectrum and corresponding degree of coherence after 10 cm propagation of a 5 nJ, 50 fs pulse in the PCF with Λ =1.55 μm and d/Λ=0.37. (b) Pulse profiles after full phase compensation (gray shading) and after compensation of only linear chirp.

or prism pair. The resulting pulse profile is shown in Fig. 4.4 b). The FWHM of the main peak is below 10 fs and the pulse exhibits a relatively good quality considered that only simple linear chirp compensation is applied here. Due to the shape of the dispersion profile, the blue wavelength components experience a higher amount of nonlinear chirp and are contained in a low level pedestal which spreads over about 1 ps. The quality and duration of the compressed pulse can be considerably improved by optimizing the fiber length, as will be shown in section 5.5. Using more sophisticated compression methods, the pulse may be compressed to its bandwidth limited pulse duration of 4.4 fs, corresponding to only 1.25 optical cycles. Since all spectral components are contained in the compressed pulse, a peak power spectral density may be defined as the ratio of energy contained in a spectral slice and the pulse duration. This yields continuous peak power spectral densities of up to 2 kW/nm which are sufficient to induce nonlinear effects in materials over the entire bandwidth of the spectrum with immediate applications in nonlinear spectroscopy.

Fabrication tolerances

The analysis in this section also gives insight into the required fabrication tolerances of the optimized PCF design. The primary goal should be to manufacture a fiber with ANDi profile. Although the spectral bandwidth and uniformity of the generated SC varies with fiber design parameters, all-normal dispersion ensures maximum coherence and smoothness of both temporal and spectral profile. If the fiber with Λ =1.55 μm and d/Λ=0.37 is taken as the desired optimum, the required pitch accuracy is determined by

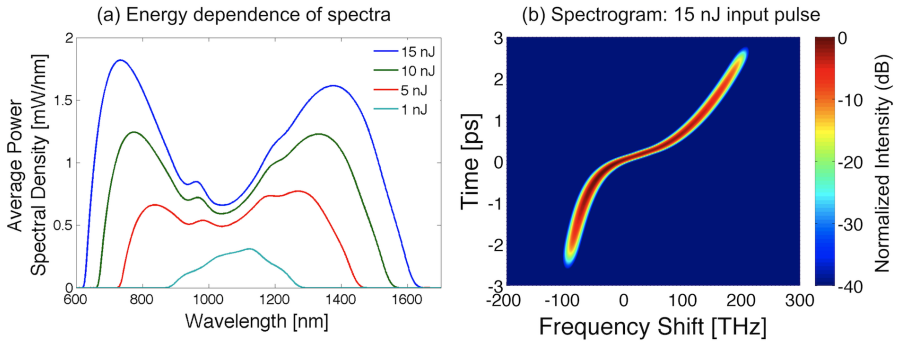

Figure 4.5. – (a) Generated SC spectra for different input pulse energies on linear scale. The pulse duration of 50 fs and propagation distance of 10 cm remain unchanged. (b) Spectrogram of the SC generated with the 15 nJ input pulse. The initial 50 fs pulse was used as the gate function.

the transition to two ZDWs at Λ =1.68 μm, i.e. the acceptable pitch tolerance is $\sim$ 8%. In contrast, a smaller than optimum pitch is uncritical. For the relative hole diameter, $d/\Lambda \leq 0.395$ is required to maintain an ANDi profile, i.e. the acceptable tolerance is $\sim$ 7%. A smaller relative hole diameter leads to drastically reduced bandwidths, therefore care should be taken to achieve high precision for this design parameter.

4.3. Influence of pump pulse parameters

In this section, the influence of a variation of input pulse parameters on the properties of the generated SC is investigated. The ANDi PCF with Λ =1.55 μm, d/Λ = 0.37 will be used for the simulations. Input pulses with Gaussian shape are considered in this section. It should be mentioned here that using input pulses with hyperbolic secant shape generally leads to similar results. Although Gaussian input pulse shape results in a slightly smoother spectrum, properties such as spectral bandwidth, general shape and coherence of the generated SC spectra are only marginally affected by the shape of the input pulse.

4.3.1. Pulse energy

Both spectral bandwidth and power density increase if input pulses with higher peak power are used. Fig. 4.5 a) shows the generated SC spectra on a linear scale for an input pulse duration of 50 fs and varying pulse energies between 1 nJ and 15 nJ, corresponding to peak powers between 18 kW and 270 kW. For high peak powers, the spectrum the peaks on each side of the pump wavelength are stronger developed than the mid section of the spectrum. A better spectral flatness at high peak powers can be achieved by increasing the normal GVD at the pump wavelength, e.g. by using a PCF with lower d/Λ value, but this also results in decreased spectral width. In the time domain, a single pulse is maintained for all investigated input energies. The pulse width at the end of the

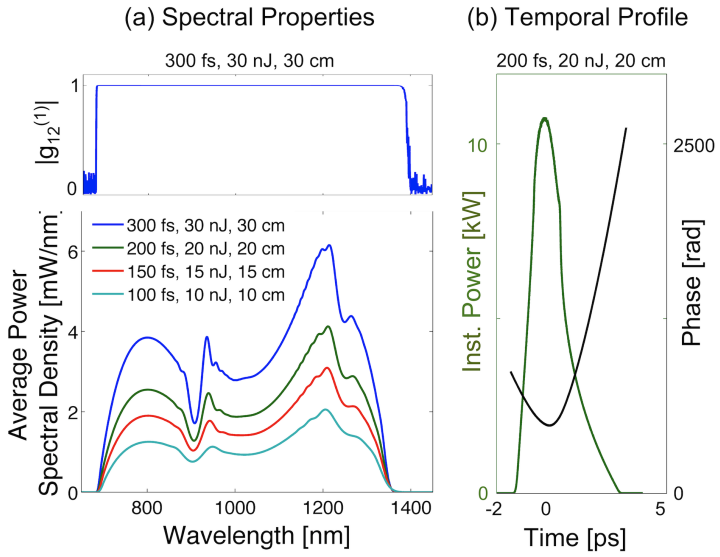

Figure 4.6. – (a) SC spectra generated with different input pulse durations. The pulse energies are adjusted in order to keep the peak power constant at about 90 kW. The fiber length is chosen such that the spectrum does not change anymore with further propagation. On top, the degree of coherence is shown for the 300 fs input pulse. (b) Temporal profile and phase of the 200 fs, 20 nJ pulse after 20 cm propagation through the fiber.

10 cm fiber section increases for higher energies due to the larger spectral bandwidth and associated GVD induced spread. As an example, Fig. Fig. 4.5 b) shows the spectrogram of the SC generated with 15 nJ input pulse energy. The pulse has broadened to a FWHM of ca. 2 ps, compared to 800 fs in the 5 nJ case which was discussed in section 4.2.3. The acquired chirp is predominantly linear in the central region of the pulse, with increasing nonlinear contributions for wavelength components further away from the pump. The nonlinear chirp contributions increase for higher input peak powers and the pulses become more difficult to compress. However, full phase compensation would in this case approach the single optical cycle limit.

4.3.2. Pulse duration

Fig. 4.6 a) shows the generated SC spectra for input pulse durations up to 300 fs at constant peak power of 90 kW. The fiber length is chosen such that the spectrum does not change anymore with further propagation. Evidently, the spectral bandwidths as well as the spectral features are identical for all input pulse durations. In order to keep the peak power constant for longer pulse durations, the pulse energy has to be increased so that the spectral power density increases accordingly. The width of the pulses in the time domain at the exit of the fiber increases for longer input pulse durations, but the ratio of linear and nonlinear chirp contributions remains nearly constant. For example, Fig. 4.6 b) shows temporal profile and phase of the 200 fs, 20 nJ pulse after propagation through

20 cm of fiber. The phase remains predominantly quadratic and the compressibility of the pulse is nearly identical to the case shown in Fig. 4.4 b) for the 50 fs, 5 nJ input pulse. Additionally, the top of Fig. 4.6 a) shows the calculated first-order coherence function for the case of the 300 fs input pulse. No degradation of the coherence properties can be observed in comparison to the 50 fs case which was investigated in Fig. 4.4 a). With ANDi PCF it is therefore possible to generate octave spanning, highly coherent SC which are recompressible to the sub-10 fs regime even with pump pulses of 300 fs duration or longer. This is in sharp contrast to the conventional broadband SC generation in fibers with one ZDW and anomalous GVD pumping, where an increase in input pulse duration usually leads to more complex temporal and spectral features and a considerable degradation of the coherence properties.

4.4. Supercontinuum generation dynamics in all-normal dispersion PCF

Since ANDi PCFs exhibit normal dispersion at all wavelengths, the well-known soliton dynamics responsible for the extreme spectral broadening in conventional PCFs with one or more ZDWs are suppressed. Pumping in the normal dispersion regime of a fiber is usually associated with drastically reduced spectral bandwidths [25, 43], and it is initially surprising that more than octave-spanning spectra can be generated in ANDi PCF. In this section the SC generation dynamics in ANDi PCF are therefore investigated in detail and the physical effects dominating the broadening process are identified. The above observations about the dependence of the generated SC spectrum on fiber design and input pulse parameters is explained. As representative example, the fiber with Λ =1.55 μm, d/Λ = 0.37 is considered. A 200 fs, 20 nJ input pulse is chosen, because the dynamics are slowed down for longer pulse durations and the physical effects are easier to be identified. Note, however, that the generated spectrum and therefore also the dynamics are identical for all input pulses with the same peak power, as was shown in Fig. 4.6.

Fig. 4.7 shows the spectral evolution of the SC generation process over a propagation distance of 20 cm. The initial evolution of the spectrum shows the broadening characteristics of SPM, but with a clear asymmetry towards the blue side of the spectrum. After ca. 2.5 cm of propagation, energy is suddenly transferred to a wavelength band around 750 nm, which rapidly gains in intensity and merges with the SPM induced peak around 900 nm. At 7 cm, a similar but not as pronounced process happens on the long wavelength side, generating a wavelength band around 1300 nm. The result is a uniform spectral structure spanning from 700 nm to 1350 nm. After 10 cm, the broadening of the spectrum is essentially concluded, only further smoothening takes place up to the 20 cm propagation distance which was considered in the analysis of Fig. 4.6.

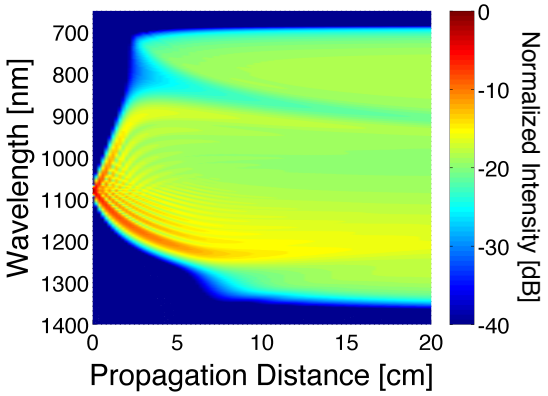

Figure 4.7. – Spectral evolution of a 200 fs, 20 nJ pulse with propagation distance in the ANDi PCF with Λ =1.55 μm, d/Λ = 0.37 in a logarithmic density plot.

Spectrogram analysis

A deeper understanding of the SC generation dynamics can be obtained by following the evolution of the pulse in a spectrogram representation, shown in Fig. 4.8. During the initial propagation in the fiber, the spectral broadening is dominated by SPM, as mentioned above. The spectrogram in Fig. 4.8 a) exhibits the SPM-characteristic *S*-shaped feature with a red-shift on the leading and a blue-shift on the trailing pulse edge, as explained in section 2.1.2. The spectrum also displays the typical oscillatory structure associated with SPM, which is created by spectral interference of identical spectral components being present at different temporal positions within the pulse.

The second part of the involved dynamics is governed by the dispersion profile of the fiber: since the fiber exhibits normal dispersions at all wavelengths, the blue-shifted wavelength components created by SPM in the intermediate trailing section of the pulse experience a higher amount of GVD than the center frequency of the pulse and hence travel slower than the pulse tail. The faster tail eventually overtakes the slower intermediate section, which leads to the steepening of the trailing pulse edge and the onset of optical wave breaking (OWB) [80]. The temporal overlap of two pulse components with different instantaneous frequencies leads to (i) interference beats in the temporal pulse profile and (ii) the nonlinear generation of new frequency components at

$$\omega_{\mathrm{FWM}} = 2\omega_{\mathrm{pump}} - \omega_{\mathrm{seed}} \tag{4.1}$$

via a degenerate four-wave mixing (FWM) process [48, 81]. The steepening of the pulse edge, temporal beats and nonlinear frequency generation are evident in Fig. 4.8 b). The SPM generated components around 900 nm act as pump and the pulse tail at 1080 nm acts as seed and create the new wavelength band around 750 nm. The sudden emergence of the wavelength band at 750 nm in Fig. 4.7 can therefore be attributed to OWB. After further propagation, OWB also occurs on the leading pulse edge (Fig. 4.8 c)) and

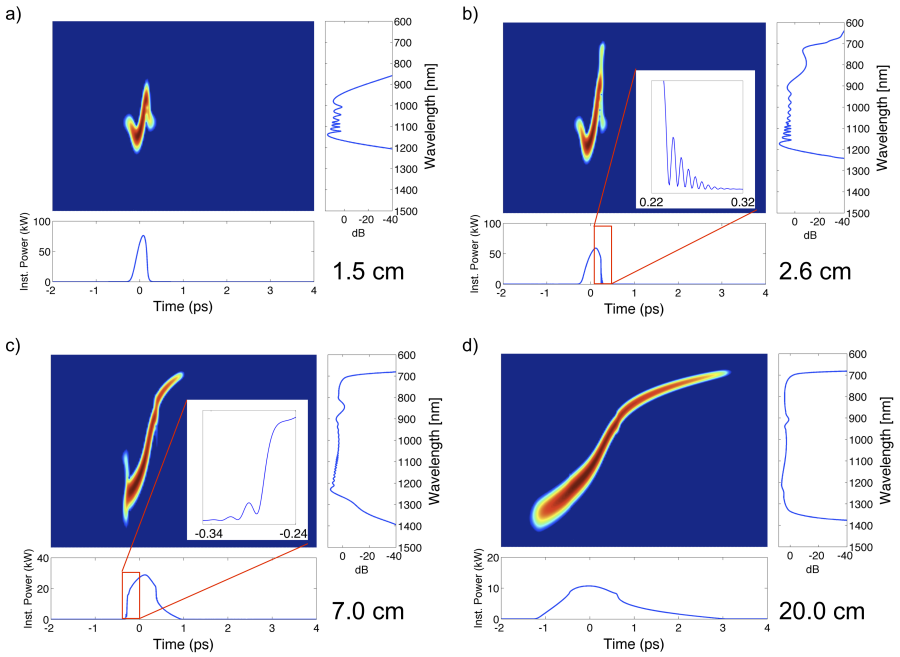

Figure 4.8. – Simulated spectrogram representation of the pulse evolution of a 200 fs, 20 nJ pulse at different propagation lengths inside the ANDi PCF with Λ =1.55 μm, d/Λ = 0.37. The projections show temporal and spectral intensity profiles.

generates new wavelengths up to a maximum of 1350 nm. The OWB process is more pronounced on the short wavelength side, because the initial SPM-induced broadening occurred slightly asymmetric towards the short wavelengths. During further propagation, energy is redistributed from the central frequency to the spectral wings until smooth, continuous and flat temporal and spectral profiles are generated with a well-defined phase distribution, Fig. 4.8 d). No interference structures are present in neither temporal nor spectral profile as the OWB process assigns each wavelength to a unique temporal position within the pulse. OWB is therefore responsible for the generation of the extreme wavelengths on both sides of the spectrum as well as for the resulting smooth temporal and spectral profiles.

Note that the OWB induced FWM processes are not phase-matched. The FWM energy transfer occurs only in the instant of temporal overlap of pump and seed, which propagate with different phase velocities. Therefore there is no restriction on the achievable bandwidth of the spectrum - it solely depends on the amount of SPM-induced broadening before OWB occurs. The wider the separation between SPM generated components and the original center wavelength of the pulse at the point of OWB, the broader the spectrum will be, according to (4.1). Flat dispersion slopes, higher pump power or higher nonlinearity therefore enhance spectral broadening.

Since the pumping occurs in the region of very low normal dispersion, (2.1) can be applied as a qualitative expression for the SPM-induced spectral broadening, which de-

pends on nonlinearity, peak power, pulse slope and propagation distance. If the peak power is kept constant and the pulse duration is increased, as is done in section 4.3.2, the pulse slope and spectral broadening are reduced. However, the spectral bandwidth can be restored by increasing the propagation distance. Since the achievable bandwidth of the generated SC depends on the amount of SPM-induced broadening before OWB occurs, this explains why the generated spectra are virtually independent of the input pulse duration for identical peak power, if the fiber length is increased accordingly.

Influence of various physical effects

The interplay between SPM and OWB can explain the observed SC generation dynamics in ANDi PCF. However, it is not obvious which physical processes cause the initial asymmetry in the SPM-induced broadening, which is responsible for the more pronounced OWB on the short wavelength side and is connected to a strong steepening of the trailing pulse edge. In fact, there are at least three different physical effects which can cause the steepening of pulse slopes: (a) optical wave breaking alone due to the interplay between SPM and normal GVD [81], (b) self-steepening due to the intensity dependence of the group velocity, which is included in the GNLSE (3.12) by the shock term $(\omega-\omega_0)/\omega_0$, and (c) the frequency dependence of the effective mode field area A_{eff}, which is represented by the frequency dependent nonlinear parameter $\gamma(\omega)$ (3.13). In addition, the Raman effect plays an important role in SC generation in conventional PCF, but it is not clear if it has the same importance in ANDi PCF. In order to assess which role these effects play in the observed dynamics, the simulation of the spectral evolution in Fig. 4.7 is repeated with the following restrictions and displayed in Fig. 4.9: (a) only SPM and the dispersion profile are regarded, i.e. both shock term and delayed Raman contributions are taken out of the GNLSE and $\gamma = \gamma(\omega_0)$ is kept constant for all frequencies. Therefore, any observed steepening of the pulse slopes is due to wave breaking; (b) as (a), but the shock term is included into the GNLSE so that self-steepening and wave breaking act together; (c) as (a), but with the full frequency dependence of $\gamma(\omega)$ taken into account, so that the frequency dependent A_{eff} and wave breaking act together; in (d), all effects are combined and reproduce the result in Fig. 4.7, but without the contribution of the delayed Raman effect ($R(t) = \delta(t)$ in (3.9)). In (e), a comparison of the linear spectrum obtained with and without delayed Raman response is shown.

It is evident from Fig. 4.9 a) that wave breaking alone cannot be responsible for the asymmetry of the spectrum towards the short wavelength side. In contrary, if SPM and dispersion act alone, the final spectrum shows a slight asymmetry on the long wavelength side. The initial SPM induced broadening appears quite symmetric, and OWB occurs first on the leading pulse edge at 3.5 cm of propagation and generates a new wavelength band around 1400 nm. On the trailing edge, OWB occurs only after 5 cm with a new wavelength band generated at around 800 nm. Fig. 4.9 b) and c) show that the effect of self-steepening and the frequency dependence of A_{eff} are quite similar. In both cases, the trailing pulse edge experiences a much more substantial steepening, OWB occurs now earlier on the blue side and the generated new wavelengths are shifted to shorter

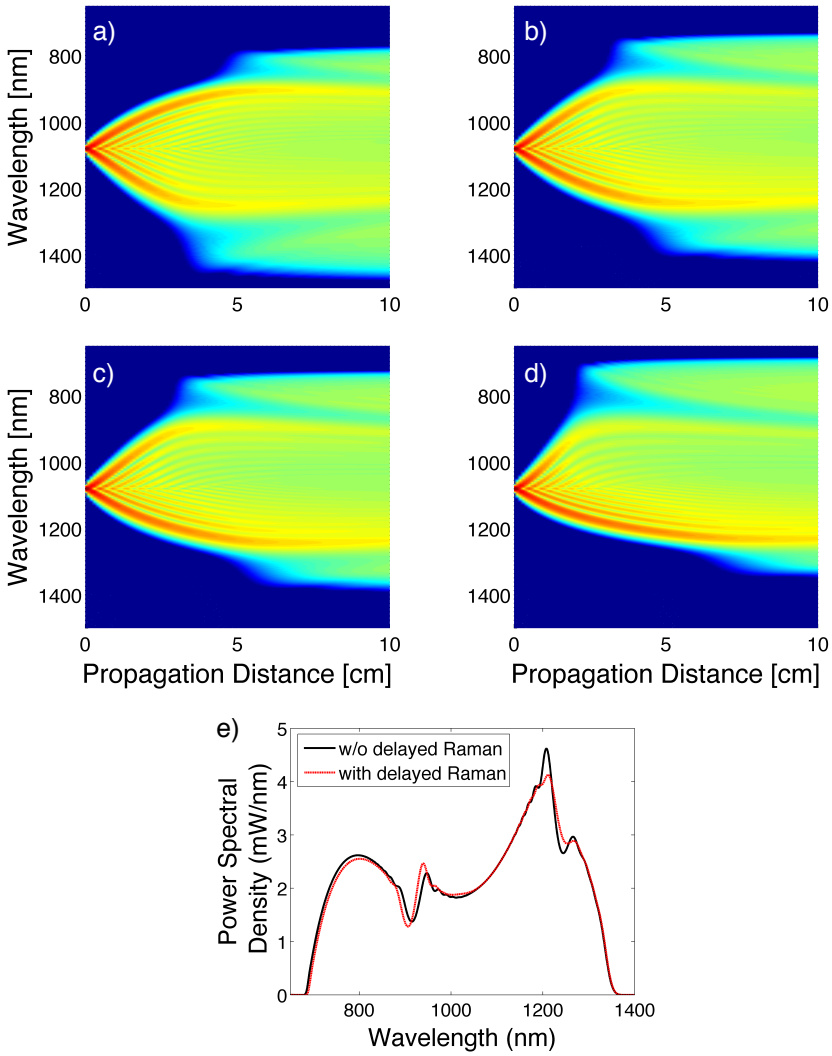

Figure 4.9. – Recalculation of the spectral evolution with input pulse and fiber parameters identical to those used in Fig. 4.7, but only certain effects are included into the calculations: (a) SPM and GVD; (b) SPM, GVD, and self-steepening; (c) SPM, GVD, and frequency dependence of A_{eff}; and (d) all of the above. (e) shows a comparison of the linear spectrum after 20 cm propagation distance obtained with and without delayed Raman response, but including all other effects.

wavelengths compared to (a). Both effects amplify each other when acting together, as shown in Fig. 4.9 d). It is evident from e) that the Raman effect does not play a significant role in the observed dynamics.

In conclusion, both self-steepening and the frequency dependence of A_{eff} contribute equally to the steepening of the trailing pulse edge, which results in enhanced initial SPM broadening of the blue side of the spectrum. These newly created short wavelength components act then as pump in the subsequent FWM process induced by OWB. Following (4.1), the higher the pump frequency, the higher is the frequency of the generated FWM products. Consequently, increased steepening of the trailing pulse edge in the initial broadening stage also leads to the FWM products being generated further towards shorter wavelengths. Applied to the set of investigated ANDi PCF this has the following implications: since the nonlinear steepening of the trailing pulse slope is counteracted by an increased value of GVD that broadens the tail, the steepening is less pronounced in fibers with lower d/Λ value or smaller pitch Λ that exhibit higher GVD at the pump wavelength. The FWM products are generated closer to the center of the spectrum, which results in a narrower but continuously flat spectrum. In fibers with higher d/Λ or larger pitch Λ with peak dispersion close to zero, the steepening is more prominent and the FWM products are generated further away from the main spectrum, resulting in a distinct peak on the short wavelength side, a depletion of the central region of the spectrum and a complementary OWB peak on the long wavelength side. This explains the observed spectral properties in Figs. 4.1 and 4.3. The same dynamics also govern the SC generation in PCF with two ZDWs, if the separation between the ZDWs is small enough to prevent soliton formation. Then SPM transports energy very quickly into the normal dispersion sections of the PCF, where the involved processes are the same as in the discussed case of ANDi PCF. Nonlinear steepening increasingly dominates over dispersive broadening for higher input pulse peak power, which results in the observed development of the spectral double peak structure in Fig. 4.5.

4.5. Summary and outlook

PCF design criteria were established to obtain broadband coherent SCs. It was shown that coherent and flat-top spectra spanning over more than one octave can be generated with optimized PCF designs that exhibit a convex dispersion profile with low normal dispersion at the pump wavelength. Spectral flatness of ± 1 dB and average power densities of several milliwatts/nanometer can be achieved over the entire bandwidth. SPM and OWB were identified as dominating effects in the SC generation process, which conserves a single pulse in the time domain that may be externally recompressed to the sub-10 fs regime even with simple means such as a grating or a prism pair. The single optical cycle limit is approached with full phase compensation. One of the major advantages of SC generation in ANDi PCFs is the independence of coherence properties, spectral bandwidth and temporal compressibility on the input pulse duration. In fact, longer high energy pulses with moderate peak power as well as moderate GVD at the pump

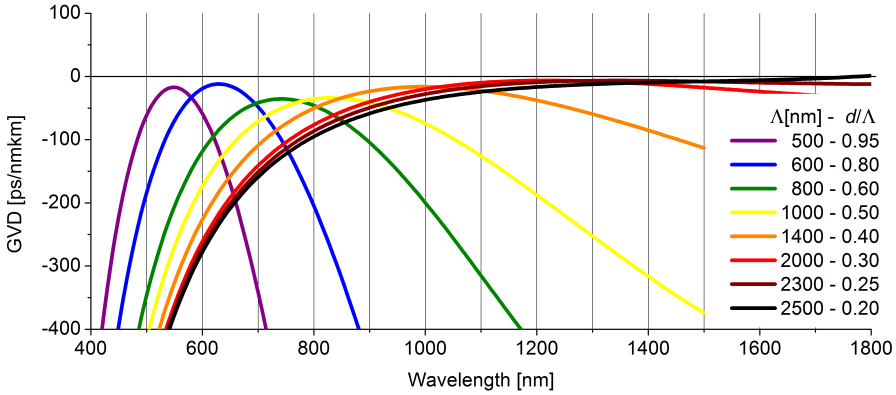

Figure 4.10. – Variety of possible ANDi PCF designs, optimized for various pump wavelengths in the visible and near-infrared spectral regions [82].

wavelength deliver the best results if flat spectra with continuously high spectral power densities are required. The broadest possible spectral bandwidth may be reached by maximizing the input peak power and minimizing the GVD at the pump wavelength, but at the cost of decreased spectral flatness. In practice, both spectral power density and bandwidth are only limited by the available pump laser and the damage threshold of the PCF.

Using the criteria established in this chapter, optimized ANDi PCF designs can be found for pump wavelengths other than 1080 nm as well. Fig. 4.10 demonstrates the full versatility of the concept, which is discussed in detail in [83]. The maximum of the dispersion profile, which should be close to the pump wavelength, can be shifted from short wavelengths around 500 nm up to about 1300 nm. A small pitch and large relative hole diameters are required for the maximum to be located at short wavelengths, while large pitches and small relative hole diameters are necessary to shift the maximum further into the near-infrared. Note that the absolute diameter d of the air holes stays almost constant at about 500 nm for every design. Relative air hole diameters near unity are approached for pumping at short wavelengths, which corresponds to a freestanding silica strand in air with submicron diameter. This concept will be further investigated in chapter 6. On the long wavelength side, where small air filling fractions are required, a limit is imposed by the material dispersion of silica. Therefore, it is not possible to shift the maximum further than around 1300 nm into the near-infrared. In this range, ultra-flattened designs with low dispersion of around 10 ps/(nm km) over several hundred of nanometers are possible, which should result in ultra-broadband SC generation. However, the large confinement loss for the small air filling fraction requires the fabrication of a large number of rings.

If the traditional PCF design is modified and a hybrid core with threefold symmetry is introduced, the mentioned limit of 1300 nm can be overcome and the maximum of the dispersion profile can be shifted further towards the infrared. This was demonstrated in [84], where a dispersion flattened design with a maximum at 1.55 μm, -2 ps/(nm km)

and dispersion variations smaller than 1 ps/(nm km) in the range 1465-1655 nm were presented.

5. Demonstration and application of coherent supercontinua generated in all-normal dispersion PCF

In this chapter, the numerical predictions of the previous chapter are experimentally verified and the first detailed demonstrations of octave-spanning SC generation in two realizations of ANDi PCF optimized for pumping in the visible and near-infrared spectral regions are presented. A nanostructured ANDi PCF with extremely small air hole diameters in the order of 400 nm is used to generate flat and temporally recompressible visible SC spectra down to 420 nm wavelength. For the first time the conservation of a single temporal pulse with smooth and stable phase distribution during the SC generation process is confirmed experimentally. The applicability of these SC pulses in ultrafast transient absorption spectroscopy is demonstrated, where they enable probing in the direct vicinity of the pump wavelength, which is not possible with bulk generated SC pulses usually employed in this technique. In the last section of this chapter, the temporal recompression of the generated SC pulses to sub-two cycle durations using only linear chirp compensation is experimentally demonstrated, and further scaling possibilities to even shorter durations are discussed.

Parts of this chapter were published in [85, 86, 87].

5.1. Fiber properties

In the following experiments two PCFs (A and B) are used with hexagonal lattice geometry and convex all-normal dispersion profiles, shown in Fig. 5.1. Fiber A was manufactured by NKT Photonics (Denmark) with a core diameter of 2.3 μm, pitch Λ = 1.46 μm and relative air hole diameter d/Λ = 0.39, resulting in a peak dispersion parameter of D = -11 ps/(nm km) at a wavelength of 1020 nm [88]. These parameters are within the optimized range for broadband near-infrared SC generation considered in the numerical study in the previous chapter. Fig. 5.1 a) shows the measured dispersion profile of PCF A, supplied by the manufacturer, as well as the calculated mode field diameter (MFD) obtained from a fully vectorial finite element mode solver (Comsol Multiphysics). Fiber B was drawn in-house at the IPHT and has a core diameter of 1.05 μm and design parameter Λ = 0.67 μm and d/Λ = 0.6. Due to input coupling difficulties into the small core, a measurement of the fiber's dispersion properties was not possible and Fig. 5.1 b) shows the calculated profile, obtained from an idealized reproduction of the fiber structure. The

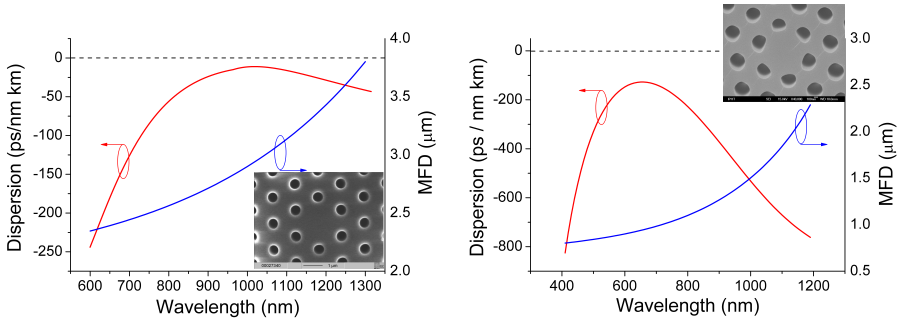

Figure 5.1. – Measured dispersion parameter and calculated MFD for PCF A with design parameters $\Lambda = 1.44$ μm, d/$\Lambda = 0.39$ and 2.3 μm core diameter. b) For PCF B, both dispersion and MFD are calculated. The fiber has design parameters $\Lambda = 0.67$ μm, d/$\Lambda = 0.6$ and 1.05 μm core diameter. The insets show scanning electron microscope (SEM) pictures of the respective PCF cross sections, courtesy of A. Dellith (IPHT Jena).

dispersion curve assumes its maximum at 650 nm with D = -127 ps/(nm km). Due to its smaller core diameter, fiber B exhibits a smaller MFD and therefore a larger nonlinearity than fiber A. The dispersion calculations were supplied by A. Hartung (IPHT Jena).

5.2. Numerical Model

In order to interpret the experimental results and compare them with the numerical results, the model with identical implementation as described in the previous chapter is employed, with the exception that all simulations presented in this chapter were calculated neglecting the wavelength dependence of the nonlinear parameter, i.e. $\gamma(\omega) = \gamma(\omega_0)$ (3.13), where ω_0 is the angular frequency of the pump. This point is discussed in in section 5.3.1. The simulation was divided into 2^{13} bins for PCF A and 2^{14} bins for PCF B. Sufficient accuracy was guaranteed by setting the acceptable photon error of the CQEM to $\delta_{\mathrm{Ph}} = 10^{-8}$ (3.24).

For the initial condition for the simulations, a complex temporal chirped Gaussian input pulse envelope $A(t) = \sqrt{P_0}\exp[(1-\sigma t)(t/t_0)^2]$ was assumed, where t is the time, σ the chirp factor and t_0 is connected with the FWHM pulse duration $t_{\mathrm{FWHM}} = \sqrt{2\ln 2}t_0$. The peak power is calculated as $P_0 = 0.94E_p/t_{\mathrm{FWHM}}$, where E_p is the pulse energy. t_{FWHM} is determined from the time-bandwidth product of the chirped Gaussian pulse $t_{\mathrm{FWHM}}\Delta f = 0.44\sqrt{1+\sigma}$, where $\Delta f = c/\lambda_0^2\Delta\lambda$ with Δf and $\Delta\lambda$ the FWHM spectral widths measured in frequency and wavelength, respectively. λ_0 is the central wavelength of the pulse and c the vacuum speed of light. σ introduces a linear frequency chirp across the pulse and accounts for the propagation through beam guiding optics and variable attenuation prior to the injection into the fiber. Typical values are in the range $\sigma = 0.5 - 1$. This definition of the pump pulse is a realistic model of the experimentally obtained pulses from an optical parametric amplifier (OPA) system and makes it possible to use $\Delta\lambda$, E_p and λ_0 as the primary input parameters for the simulation, which are

directly accessible from spectrum and power measurements.

When comparing simulations to experiments for anomalous dispersion pumping, ensemble averages have to be calculated in order to achieve good agreement due to the noise-sensitive pulse-to-pulse fluctuations, which can be significant as shown in section 2.3. Since the generated spectra in ANDi PCF are highly coherent, the ensemble average and a single shot simulation are virtually identical and cannot be separated on the given scales. Therefore, single shot simulations are depicted in all subsequent figures.

5.3. Spectral measurements

It was established in the previous chapter that the broadest spectra can be expected when pumping occurs close to the maximum of the fiber dispersion curve. Therefore, fiber A is employed for near-infrared SC generation pumped at 1050 nm, while fiber B is more suitable for visible SC generation pumped at 650 nm. In addition, the performance of both fibers is investigated at 790 nm, a typical operating wavelength of Ti:Sapphire femtosecond laser systems.

5.3.1. Near-infrared supercontinuum generation with PCF A

A Coherent OPerA OPA system was used to generate ultrashort pulses of ca. 50 fs duration at central wavelengths of 1050 nm and 790 nm with 1 kHz repetition rate. After variable attenuation, the pulses were coupled into a ca. 0.5 m long piece of PCF A and the spectrum after the fiber was recorded with an optical spectrum analyzer. Using an 8 mm focal length aspherical lens, input-coupling efficiencies as high as 40% could be achieved.

Fig. 5.2 shows the experimentally recorded spectra for various pump pulse energies on a logarithmic scale. For the 1050 nm pump, the broadening occurs almost symmetrically around the pump wavelength. With the highest applied pump pulse energy of 7.8 nJ, a spectral bandwidth of 905 nm (-20 dB) is achieved, which corresponds to almost 1.5 octaves. This is the broadest spectrum generated in the normal dispersion regime of an optical fiber to date. While for lower and medium pump energies the spectra exhibit a flat-top structure with only marginal intensity variations over the entire bandwidth ($<$ $\pm$1.5 dB), at higher energies a "dip" is forming around the pump wavelength whose depth increases with pump energy and reaches ca. -10 dB for 7.8 nJ. This effect was predicted and analyzed in detail in sections 4.3.2 & 4.4.

When pumping the fiber at 790 nm, i.e. far away from the maximum of the dispersion curve, the broadening occurs asymmetrically. A broad shoulder is formed towards the maximum of the dispersion curve on the long wavelength side. At comparable pump energies the spectrum is narrower than in the case of pumping close to the dispersion maximum, at 8 nJ a -20 dB spectral bandwidth of 670 nm is achieved. When the pump energy is increased to 12.5 nJ, the bandwidth expands to 880 nm and the spectrum spans from 540 nm to 1420 nm.

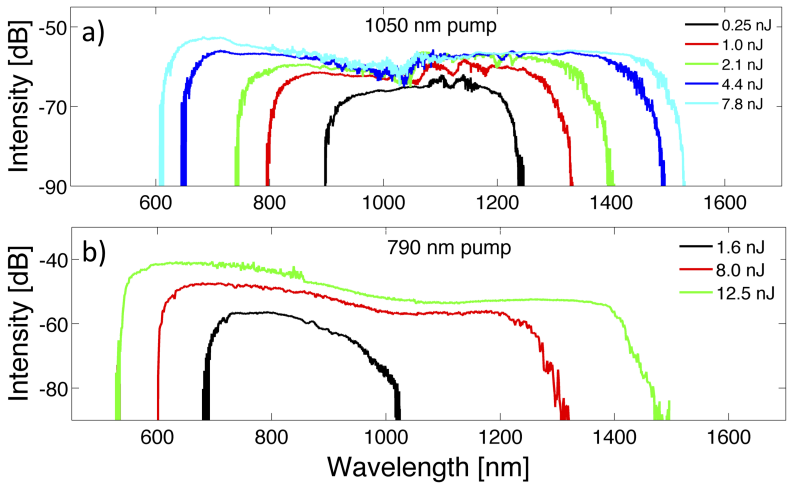

Figure 5.2. – Experimentally recorded supercontinuum spectra after 0.5 m of PCF A in dependence of the pulse energy for a central pump wavelength of 1050 nm (a) and 790 nm (b). The pump pulse duration is in the order of 50 fs in all cases.

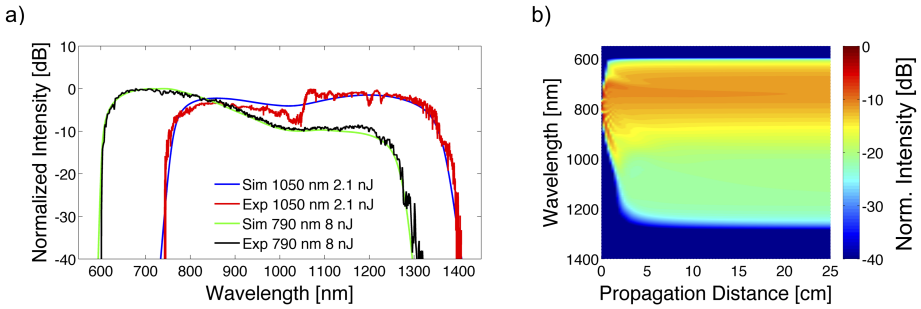

Figure 5.3. – Comparison of simulated and experimental spectra for both 790 nm and 1050 nm pumping. b) Simulated spectral evolution for the 8 nJ pump pulse at 790 nm in a logarithmic density plot.

In order to interpret the experimental results, numerical simulations were performed with the experimentally determined FWHM spectral width of the pump source $\Delta\lambda$ = 42 nm for 1050 nm pumping and $\Delta\lambda$ = 15 nm for 790 nm pumping. The remaining parameters matched the stated experimental conditions and loss in the fiber was neglected. In Fig. 5.3 a) the comparison between experimental and numerical results is presented, which shows remarkable agreement both in bandwidth and shape of the spectrum. The modulation around the 1050 nm pump is most likely caused by higher order phase modulations and imperfections of the input pulse generated by the OPA and cannot be reproduced by the simulation. Fig. 5.3 b) shows the simulated spectral evolution for the example of the 8 nJ pump pulse at 790 nm over a propagation distance of 25 cm. The full spectral bandwidth is generated within the first 3 cm of propagation and after ca. 10 cm a steady state is reached, i.e. the spectrum does not change significantly with

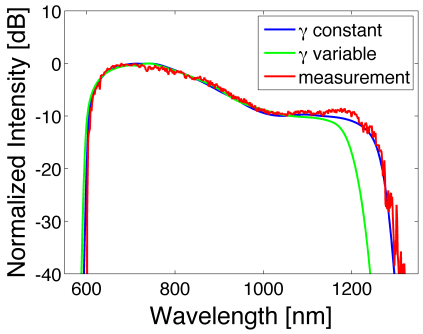

Figure 5.4. – Experimental results for 790 nm, 8 nJ, 50 fs pumping of PCF A compared with corresponding simulations assuming a constant nonlinear parameter $\gamma(\omega_0)$ and frequency dependent $\gamma(\omega)$, taking into account the full variation of the MFD shown in Fig. 5.1.

further propagation. An analysis of the spectrogram evolution reveals that the interplay of SPM and OWB dominates the spectral broadening process [85], as was discussed in detail in section 4.4.

Numerical observation: influence of the variable effective mode field area

In section 5.2 it was mentioned that all numerical simulations in this chapter are performed assuming a constant nonlinear parameter $\gamma(\omega_0)$ for all wavelengths. Since the frequency dependence of γ mainly originates from the variation of the effective mode-field area A_{eff}, this assumption neglects the varying MFD shown in Fig. 5.1. If this variation is included into the simulation using the modified GNLSE 3.14 with a rigorous treatment of the frequency dependent MFD, the comparison with the experimental results reveals a significant underestimation of the spectral bandwidth for long wavelengths in the order of 80 - 100 nm, as exemplary shown in Fig. 5.4 for 790 nm pumping of PCF A. In contrast, the calculation assuming constant γ agrees perfectly with the measurement. In this case the short wavelength edge is also well reproduced with variable γ due to the small variation of the MFD in the range 600 - 800 nm. In the case of the symmetric broadening with 1050 nm pumping, a variable γ also produces an overestimation of the bandwidth on the short wavelength side, which is in the order of 30 - 40 nm, i.e. generally smaller than the differences on the long wavelength edge.

The observation that the experimental results are much better represented by a constant nonlinear parameter is in a first approach a numerical issue, which could have several imaginable reasons not connected to any physical effect. However, this fact was observed in all the measurements with ANDi PCF, with both fibers A and B, as well as in the experiments with tapered suspended core fibers with ANDi profile, which will be discussed in the next chapter. As an initial hypothesis for explaining this observation, the following mechanism is proposed. SPM and OWB generate new wavelength components where the pump intensity is highest, i.e. in the center of the mode field area of the pump. A variable γ would imply that these new wavelength components assume their

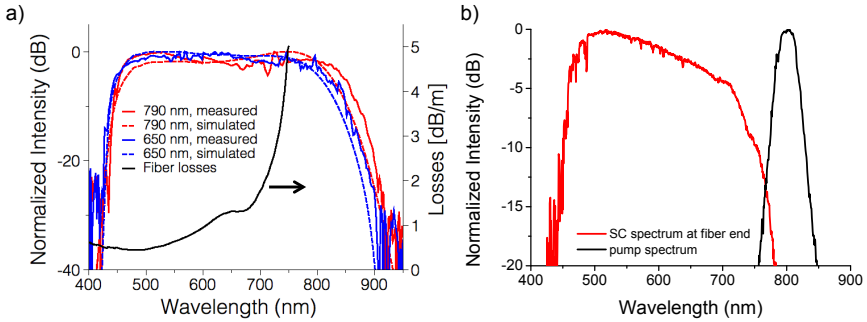

Figure 5.5. – a) Measured and simulated spectra generated in a 18 cm piece of PCF B pumped with 50 fs pulses at 650 nm and 790 nm. The pulse energy at the fiber end was measured to 1.1 nJ (650 nm) and 0.9 nJ (790 nm), respectively. Experimentally determined losses are quantified on the right ordinate. b) If the fiber length is increased to 50 cm, the generated SC spectrum does not contain any components at the pump wavelength of 790 nm. Here the pulse energy at the fiber end is 0.6 nJ.

equilibrium MFD instantaneously. Instead, the hypothesis is that the new components initially propagate in the mode-field area of the pump that creates them and only assume their equilibrium MFD after some propagation distance. Since the SC generation dynamics are very fast in the investigated cases, this would explain why the generated spectrum is better explained by a constant MFD. The variable effective mode field area has been shown to be of importance in dynamics involving soliton self-frequency shift [89], but these are much slower dynamics than observed in the present case. However, these numerical observations are in no way a proof of this initial hypothesis and it will be tested in future research.

5.3.2. Visible supercontinuum generation with PCF B

PCF B was used for visible and near-infrared supercontinuum generation in an identical setup as described in the previous section. The OPA was set to generate 50 fs pulses at the fiber dispersion maximum of 650 nm as well as at 790 nm. Due to its small core diameter, the input coupling efficiency was only 15 - 20%.

Fig. 5.5 a) shows the experimentally recorded and simulated spectra in a 18 cm long piece of PCF B. Interestingly, the generated spectra seem to be almost independent of the pump wavelength. Both spectra, generated with either 650 nm or 790 nm central pump wavelength, span from ca. 425 nm to 900 nm (-20 dB) over more than one octave. The intriguing similarity is caused by the exponentially increasing fiber loss above 700 nm, which dampens wavelength components generated in this region. In addition, the large dispersion slope prevents significant broadening for shorter wavelengths. The unusual loss profile can be explained by the fact that the confinement loss in PCF structures increases with wavelength and becomes significant already at 700 nm in this case due to the extremely small structures of the fiber. The agreement between simulation and experiment is again excellent. In this case, the full loss profile is included into the simulations

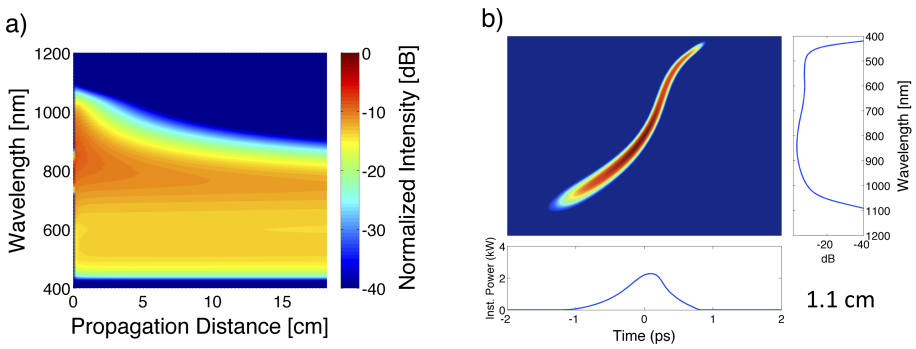

Figure 5.6. – a) Simulated evolution of the SC spectrum over propagation distance through PCF B when pumped at 790 nm. The properties of the input pump pulse are identical to Fig. 5.5 a). b) Simulated spectrogram of the SC pulse after 1.1 cm of propagation

and slight deviations between experiment and simulation are caused by uncertainties in the fiber loss measurement for the high loss region.

The high fiber losses above 700 nm wavelength can lead to the unusual phenomenon that the SC spectrum at the end of the fiber does not contain any components of the pump wavelength, which is depicted in Fig. 5.5 b). Here the fiber was also pumped at 790 nm, but a longer 0.5 m fiber piece was used in the experiment. Note that the coupled pump pulse energy was less than in Fig. 5.5 a) which explains the slightly narrower spectrum on the short wavelength side.

The fact that a broad SC spectrum is generated even when pumping occurs in the high loss region indicates that the SC generation dynamics must be extremely fast. The numerical simulation of the spectral evolution, shown in Fig. 5.6 a), confirms this: the spectrum is generated within the first few millimeters of propagation. It remains constant on the short wavelength side but its extent decreases on the long wavelength side due to the high losses. If the fiber length is kept to a few centimeters, a spectrum spanning from ca. 400 - 1100 nm can be obtained. The SC generation dynamics are identical to those discussed in section 4.4, but they are accelerated due to the large nonlinearity of PCF B. The spectrogram of the generated SC pulse is shown in Fig. 5.6 b). Due to the uncomplicated phase distribution, temporal recompression should be realizable.

5.4. Ultrafast transient absorption spectroscopy

Up to this point the temporal characteristics of the generated SC pulse were inferred from numerical simulations. Since the agreement between experiment and simulation is excellent in the spectral domain, it is fair to assume that the same is valid in the temporal domain. However, the experimental validation of the numerical predictions is critical for many applications, especially the conservation of a single temporal pulse and the generation of a smooth and stable phase distribution need to be confirmed.

The SC pulses are temporally characterized and at the same their application is demon-

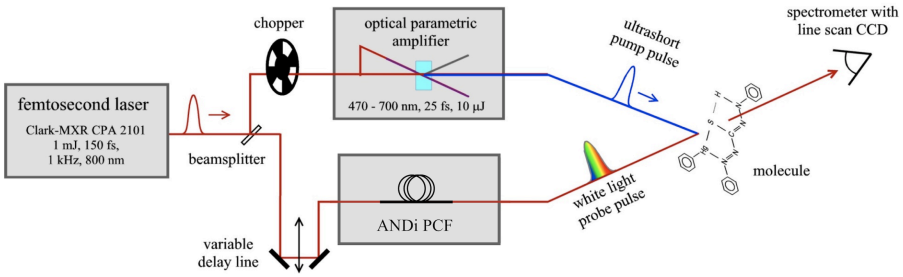

Figure 5.7. – Experimental setup of the transient absorption spectroscopy experiment used to determine the temporal characteristics of the generated SC pulse.

strated using a pump-probe ultrafast transient absorption spectroscopy (UTAS) measurement [90]. A photo-induced process is investigated by exciting sample molecules with a short laser pulse. The dynamics of the excited sample molecule are then probed by a second light pulse that monitors the photo-induced transmission changes in dependence of the time delay between pump and probe pulse. If a SC pulse is used as probe and the full spectrum is recorded at each delay step [91, 92], the chirp of the pulse is directly accessible from the measurement [93].

The key benefit of using SCs generated in ANDi PCF for UTAS is the possibility of probing in the direct vicinity of the wavelength used for pumping the SC generation process. This is not possible with bulk-generated SC pulses usually employed in this technique, because the low conversion efficiency in bulk requires filtering of the fundamental, which creates a spectral gap not accessible for probing molecular dynamics [93].

Experimental setup

Fig. 5.7 a) illustrates the experimental setup. As the central light source we use a Ti:Sapphire regenerative amplifier system (Clark MXR 2101) emitting 150 fs pulses at 775 nm with a repetition rate of 1 kHz. A fraction of the available output power drives a noncollinearly phase-matched optical parametric amplifier (NOPA) capable of generating pulses of ca. 25 fs duration at 600 nm wavelength, which will excite the sample molecules in the subsequent UTAS measurement and define its temporal resolution. About 5 nJ of the CPA output at 775 nm is coupled into a 20 cm piece of PCF A to generate the SC used as probe pulse. The fiber length was determined by experimental constraints, in principle it would be possible to use much shorter fibers. The generated SC spectrum is narrower than discussed in section 5.3.1 and spans from 620 - 1100 nm due to the longer input pulse duration. After passing through the sample, the probe is analyzed in a spectrometer with a fast line-scan CCD camera capable of single shot measurements. The time delay Δt between NOPA pump and SC probe pulse can be controlled with a retro reflector mounted on a linear stage.

In order to generate a large signal-to-noise ratio, a sample mixture of two laser dyes (1:1 ratio of Rhodamine 700 and Styryl 9 dissolved in methanol) with strong absorption

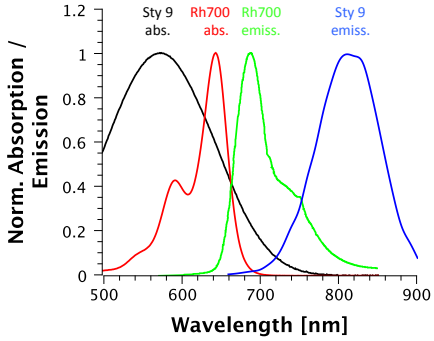

Figure 5.8. – Normalized steady-state absorption and fluorescence spectra of Rhodamine 700 and Styryl 9.

and fluorescence characteristics was used. The normalized steady-state absorption and fluorescence spectra of both dyes are shown in Fig. 5.8. The absorption spectra were measured with a spectrophotometer and the emission spectra were obtained from literature [94, 95]. Since both dyes can be excited at 600 nm, the NOPA was set to generate pump pulses at this wavelength. Rhodamine 700 has a broad fluorescence band around 700 nm, while the fluorescence peak of Styryl 9 is centered around 800 nm. Since the upper range limit of the used spectrometer was 900 nm, the mixture was sufficient to generate a transient signal over the accessible bandwidth of the generated SC spectrum. Note, however, that the absolute absorbance and emittance values for Rhodamine 700 are much higher than for Styryl 9, so that stronger signals are expected from the wavelength range covered by Rhodamine 700.

A chopper wheel in the pump beam blocks every second excitation pulse so that the normalized transmission T_N of the sample can be calculated as

$$T_N(\Delta t, \lambda) = \frac{I^*(\Delta t, \lambda)}{I_0(\lambda)}, \tag{5.1}$$

where I^* and I_0 are the intensities of the transmitted probe light through the excited and unpumped sample, respectively. Δt is changed in such a way that the NOPA pump pulse is slowly shifted through the SC probe pulse from trailing to leading edge. Note that this procedure leads to the fact that wavelengths generating a signal at earlier time delays propagate at the trailing edge of the SC pulse, which is contrary to the usual convention in numerical simulations.

Temporal characterization of the supercontinuum pulses

Fig. 5.9 a) shows the experimentally recorded normalized transmission in dependence of wavelength and time delay Δt between NOPA pump and SC probe pulse. Such a plot is usually used to extract molecular dynamics, but this is beyond the scope of the thesis. This analysis focusses on the onset of an increased T_N between -4 ps and +1 ps delay. T_N can only increase if the NOPA pump pulse arrives first at the sample,

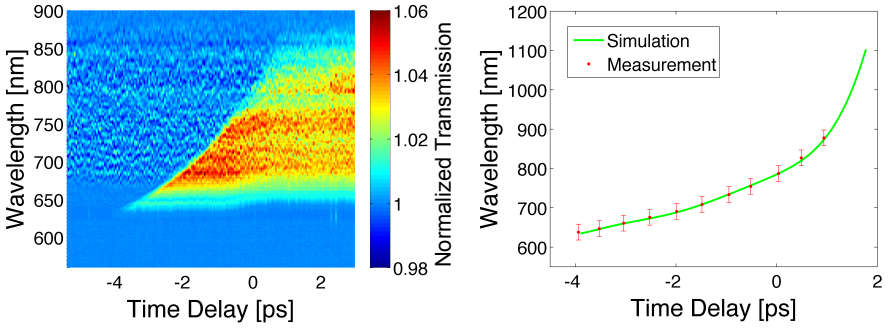

Figure 5.9. – a) Experimentally recorded normalized transmission T_N of a Rhodamine 700 / Stryryl 9 mixture dissolved in methanol in dependence of wavelength and time delay between pump and probe pulse. b) Comparison of chirp determined from a) and extracted from a spectrogram simulation matching the experimental conditions. The time delay is arbitrarily set to zero for the input wavelength into the ANDi fiber of 775 nm. Note that wavelengths at earlier time delays propagate at the trailing edge of the SC pulse, which is contrary to the usual convention.

excites the fluorescent molecules and causes either ground state bleach or stimulated emission is generated by a specific wavelength component of the SC probe pulse. Due to its chirp, the different wavelength components of the SC pulse arrive at different times at the sample. Therefore also the delay for the onset of increased T_N signal is wavelength dependent. This specific delay is also called Òtime zeroÓ, as it corresponds to the exact temporal overlap between the short pump pulse and the specific probe pulse component, if the excitation of the sample molecules is assumed to be instantaneous. In the present case this is a valid assumption, because the NOPA pump pulses are extremely short compared to the SC probe pulse and the excitation time of Rhodamine 700 is in the order of a few femtoseconds [96]. By extracting the wavelength dependent time zero from Fig. 5.9 a), the temporal position of each wavelength component within the probe pulse, i.e. the chirp of the SC pulse, can be determined. This is a well-understood procedure for the temporal characterization of bulk-generated SC pulses in UTAS measurements [93]. In Fig. 5.9 b), the experimentally determined chirp is compared to the chirp extracted from a numerically simulated spectrogram after adaption to the experimental conditions. The comparison shows again the excellent agreement between simulation and experiment, both in spectral and temporal domain. This measurement therefore confirms the numerical prediction of the conservation of a single ultrashort pulse in the time domain with deterministic phase distribution. The SC pulse is stretched to nearly 6 ps after propagation through the 20 cm of PCF A. Note that the choice of fiber length was purely due to experimental constraints. As discussed in section 5.3.1, the SC generation dynamics are quite fast and a much shorter piece of fiber could be used to generate the same bandwidth, reducing chirp and pulse duration accordingly.

Finally, some molecular dynamics can be extracted from Fig. 5.9 a). The measurement exhibits two major wavelength bands with elevated T_N: one in the range 700 - 750 nm,

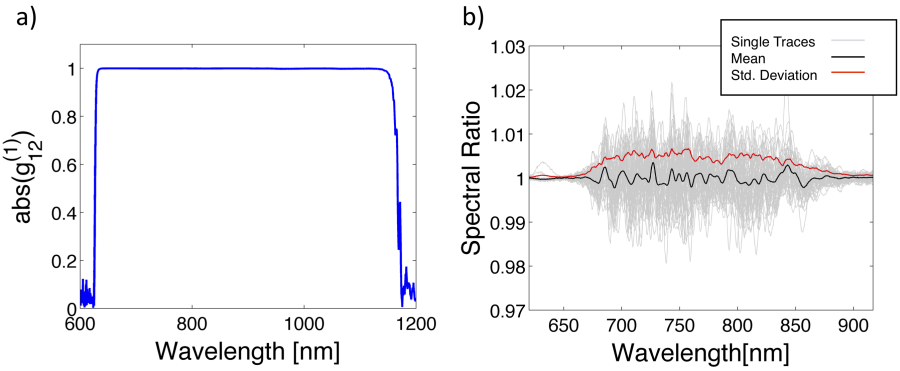

Figure 5.10. – a) Simulated first order coherence function $|g_{12}^{(1)}(\lambda, t_1 - t_2 = 0)|$ for the SC generated with 150 fs, 5 nJ pulses at 775 nm used for the UTAS measurement. b) Pulse-to pulse spectral intensity fluctuations extracted from Fig. 5.9 a).

whose intensity is decreasing with time delay, and another wavelength band around 820 nm, whose intensity increases with time delay. Comparison with the steady-state spectra in Fig. 5.8 allows the attribution of the 700 - 750 nm structure to the fluorescence emission band of Rhodamine 700, while the signature around 820 nm can be identified as the Styryl emission. Consequently, $T_N > 1$ can be attributed to stimulated emission from excited molecules. The steady-state spectra also reveal that the broad absorption band of Styryl 9 overlaps with the peak emission wavelength of Rhodamine 700. The observed dynamics in the measurement can therefore be explained by a fast energy transfer between the dyes through re-absorption of the Rhodamine 700 fluorescence by Styryl 9. This happens within a few picoseconds from the initial excitation.

Coherence and stability

The SC generation dynamics in ANDi PCF are dominated by SPM and OWB, which create new frequency components with a deterministic phase relation to the injected pulse. Consequently, the resulting spectrum is expected to be highly coherent. This argumentation is verified by including input pulse shot noise and spontaneous Raman noise into the numerical simulation and computing the complex degree of first order coherence $|g_{12}^{(1)}(\lambda, t_1 - t_2 = 0)|$ (3.11). Fig. 5.10 a) shows the simulation for the SC used for the UTAS measurement pumped with 150 fs, 5 nJ pulses at 775 nm. As expected, $|g_{12}^{(1)}(\lambda)| = 1$ over the entire bandwidth, which corresponds to perfect coherence.

Important information about the coherence properties can be extracted from the UTAS measurement in Fig. 5.9 a). Firstly, the SC pulses need to be extremely stable in pulse duration and phase in order to produce the sharp chirp line visible in the experiment. Since the measurement takes about 10 minutes to complete, this already implies high stability and temporal coherence of the generated SC pulses. Secondly, the pulse-to-pulse intensity fluctuations can be extracted from early time delays for which the probe pulse arrives before the pump pulse at the sample. Then two subsequent SC pulses passing

through the unpumped sample are referenced to each other according to (5.1). Fig. 5.10 b) shows the wavelength dependent fluctuations for 50 individual traces over the bandwidth of the measurable spectrum as well as the average and standard deviation of the ensemble. While fluctuation spikes are present up to ± 2%, the standard deviation is well below 1%. This is consistent with amplitude stability measurements of the CPA pump system used in the experiment. Therefore it can concluded that the observed fluctuations of the SC spectrum are induced by the noise of the pump system and no obvious additional noise has been added during the SC generation process. Significantly better fluctuation stability can be expected if the fiber is pumped directly from a modelocked oscillator instead of a CPA system, because the amplitude fluctuations of the input pulse arising from the amplification stage and subsequent attenuation can be avoided. It is interesting to note that the measured fluctuations decrease towards the edges of the spectrum. While this can be attributed to the reduced sensitivity of the spectrometer close to its range limit at 900 nm, the increased stability below 680 nm was clearly visible and is also evident in the measurement of Fig. 5.9 b). Simulations including pump pulse amplitude fluctuations could not reproduce this effect, and it will be investigated further in the future.

5.5. Sub-two cycle pulse compression

Up to this point it has been successfully demonstrated that the SC generation process in ANDi PCF is highly coherent, preserves a single pulse in the time domain and provides ultra-broad spectra with smooth intensity and phase. These are ideal properties for the temporal recompression to few optical cycle pulses by spectral phase compensation.

Few-cycle pulse generation has been subject to intense recent research efforts due to a wide range of applications, for instance in time-resolved studies of fundamental processes in physics, chemistry and biology [97]. High energy few-cycle pulses, typically generated by gas-filled hollow fiber compression (HFC) [98] or optical parametric chirped pulse amplification [99, 100], allow for applications such as high harmonic generation and attosecond pulse generation [101].

Although commercial few-cycle Ti:sapphire based oscillators are available, the generation of high quality sub-two cycle pulses is still challenging. The shortest pulses (2.6 fs, 1.3 cycles) have been generated using spectral broadening via SC generation in gas-filled hollow core fibers and compression with an active phase shaping device [98], but this generally requires amplified pulses with >100 μJ pulse energy. In contrast, solid core fibers allow for sufficient spectral broadening and potential pulse compression already at nanojoule pulse energies. If a short piece of standard single-mode fiber is employed, pulse energies in the order of 10 nJ can generate spectral broadening sufficient to compress to less than 5 fs duration [102]. However, higher order phase compensation is required and the achievable pulse width is restricted by the material dispersion of silica, which leads to strong dispersive temporal broadening for pulses with 800 nm central wavelength and therefore limits the obtainable spectral width for low energy pulses. In both hollow core

fiber and single-mode fiber compression, pumping occurs deep in the normal dispersion regime generating coherent spectra with deterministic phase distribution, which allows reliable recompression.

The ultrabroad spectra generated in conventional PCF with very low energy pulses are in principle of great interest for few-cycle pulse compression, but have so far found only limited application. By using a 5 mm piece of PCF, which exhibits a single ZDW in the vicinity of the pump, compression to 5.5 fs has recently been demonstrated employing active phase shaping and 2.7 nJ, 15 fs pump pulses [103]. The problem is, however, that the sensitivity of the SC generation dynamics to pump pulse fluctuations leads to variations in spectral structure and phase, which ultimately limit the pulse duration and quality achievable by compression [22, 103, 104]. The resulting fundamental limits to few-cycle pulse generation from compression of SC spectra generated in PCF with single ZDW were theoretically studied in [28]. Impressive results down to sub-two cycle durations have also been achieved using soliton self-compression in PCF, which takes advantage of the initial stage of spectral broadening and temporal compression of higher order soliton propagation, thus obviating the need of post-compression devices [105]. The scaling of this concept to the single cycle regime has also been theoretically investigated [106]. Input pulse parameters and fiber length are chosen to prevent pulse break-up and maintain coherence, but this usually limits the application of the scheme to subnanojoule pulses. In addition, the resulting pulses typically suffer from considerable side peaks and pedestals.

In this section it is demonstrated that the special temporal properties of the SC generated in ANDi PCF allow compression to high quality sub-two optical cycle pulses simply by linear chirp compensation with a compact chirped mirror compressor. In addition it is shown that the previously reported limits to few-cycle pulse generation from compression of SC spectra generated in conventional PCFs do not apply for ANDi PCF due to the excellent coherence properties, which are independent of fiber length and input pulse parameters. Finally, the scalability of the concept to single cycle pulses is numerically investigated.

Experimental setup

The experimental setup is shown in Fig. 5.11. The seed laser is a cavity-dumped Kerr lens mode-locked Ti:sapphire oscillator delivering up to 10 nJ pulse energy at 800 nm central wavelength and 2 MHz repetition rate. An output pulse width of 15 fs is measured using a commercial broadband SPIDER device (VENTEON Laser Technologies GmbH, Germany) with a measurement range from 600 - 1200 nm. The pulses are coupled into a 1.7 mm long piece of PCF A via a 6.5 mm focal length aspheric lens with up to 40% efficiency on a piezo-controlled translation stage. The dispersion of the lens is precompensated with chirped mirrors so that pulses of 15 fs duration are expected at the input of the fiber.

The SC spectrum generated in the fiber is collimated with a gold-coated 25 mm focal length off-axis parabolic mirror and the resulting large beam diameter is reduced by a

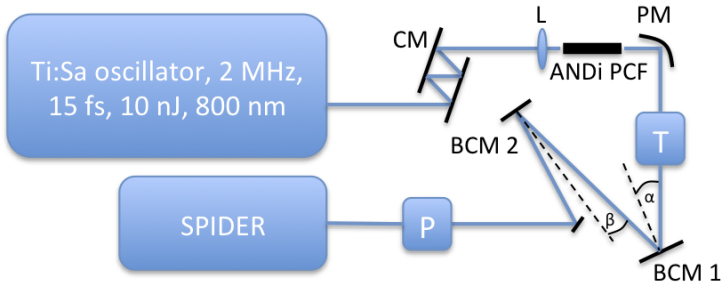

Figure 5.11. – Schematic experimental pulse compression setup. CM chirped mirrors; L aspheric lens; PM parabolic mirror; T telescope; BCM broadband chirped mirror; P periscope.

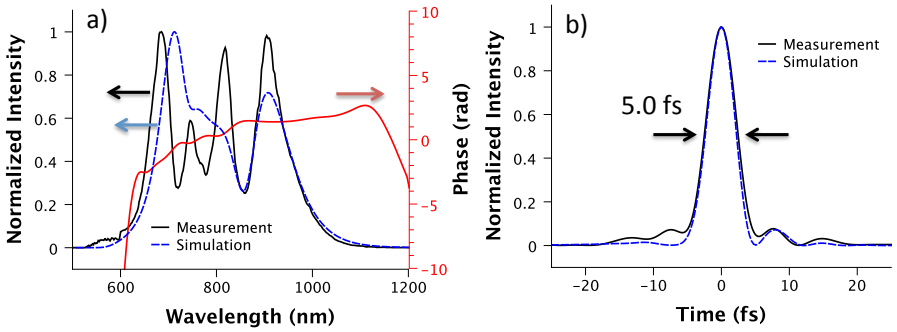

Figure 5.12. – a) Measured spectrum at 1.7 nJ pulse energy, comparison with numerical simulation and measured spectral phase after compression. b) Reconstructed temporal pulse envelope and corresponding simulation result.

telescope consisting of two silver-coated spherical mirrors. The use of mirrors instead of lenses, the short fiber length and the stable SC spectrum allow pulse compression to sub-two cycle durations simply by linear chirp compensation with a compact broadband chirped mirror compressor (UltraFast Innovations GmbH, Germany), designed to provide constant negative GVD of -30 fs^2 per bounce in the range 650 - 1250 nm. Oscillations of the GVD curves are effectively minimized by using two different incident angles of $\alpha = 20^o$ and $\beta = 5^o$, as indicated in Fig. 5.11. After adaption of the polarization by a periscope, the compressed pulses are characterized using the SPIDER device described above.

Compression results

The generated spectrum for 1.7 nJ input pulse energy is depicted in Fig. 5.12 a). It spans over more than one octave from 530 nm to 1100 nm and agrees well with numerical simulations. Slight deviations are caused by uncertainties in the phase of the input pulse, which is not known exactly after passing through the focusing lens. The measured spectral phase after compression is flat over the bandwidth of the spectrum, only in the fraction below 650 nm the chirped mirrors are not able to compensate the phase appropriately

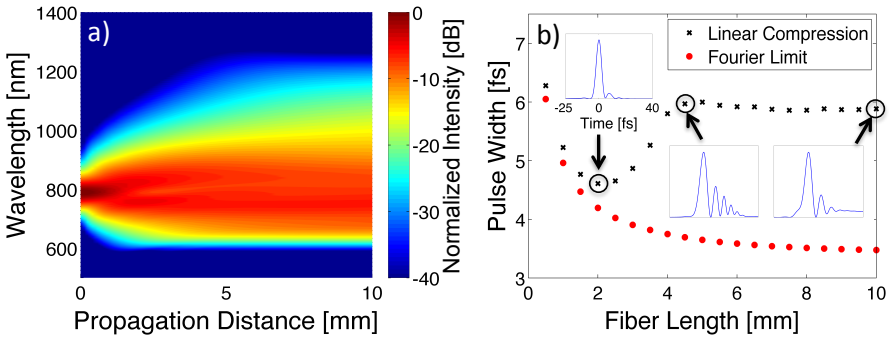

Figure 5.13. – a) Simulated spectral evolution over 10 mm propagation distance for 1.7 nJ, 15 fs input pulse. Achievable pulse width using linear compression only (black cross) and full phase compensation (red dot). The insets show examples of compressed pulse profiles for linear compression.

due to their range limit.

The simulation assumes a complex chirped sech-shaped temporal input pulse field envelope $A(t) = \sqrt{P_0}\,\mathrm{sech}^{(1-i\sigma)}(t/t_0)$ with $t_{\mathrm{FWHM}} = 2\ln(1+\sqrt{2})t_0 = 15$ fs duration. This definition of the chirp parameter σ introduces a linear chirp over the central part of the pulse with increasing higher order contributions in the wings, which is more realistic for broadband Ti:Sapphire oscillators than a pure linear chirp assumption [107]. The rest of the implementation is identical to the description in section 5.2.

The reconstructed pulse shape is shown in Fig. 5.12 b) with a FWHM pulse duration of (5.0±0.3) fs, corresponding to 1.85±0.11 optical cycles. The measurement was stable and repeatable with only minor fluctuations in the reconstructed pulse shape and duration. A SPIDER signal was obtained for the entire bandwidth of the spectrum with good fringe visibility. Considering that only linear chirp compensation is applied, the pulses exhibit an exceptional quality. The main peak contains more than 80% of the total pulse energy in a ±5 fs wide temporal window. The measured pulse profile is also in excellent agreement with the simulation, which was obtained from the simulated spectrum in Fig. 5.12 a) by compensation of quadratic phase only. Note that the Fourier-limited pulse duration of the measured spectrum is 3.9 fs, which could be obtained by using higher order chirp compensation.

Fiber length optimization

In order to minimize the pulse duration achievable by linear compression, the fiber length was optimized by numerical simulation. The generated spectrum was calculated for 1.7 nJ input pulse energy in dependence of the fiber length (Fig. 5.13 a)), and the pulse width was determined for linear chirp compensation as well as for full phase compensation (Fig. 5.13 b)). While the spectrum broadens and consequently the Fourier limited pulse duration decreases with propagation distance, the minimum achievable pulse width of 4.6 fs for linear compression is reached at a fiber length of about 2 mm. For shorter fiber

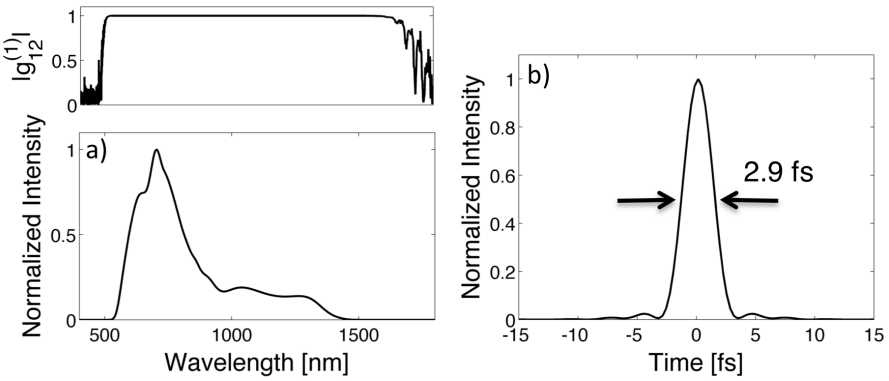

Figure 5.14. – a) Mean spectrum and degree of coherence for 4 nJ, 15 fs input pulses and 10 mm fiber length, calculated over the simulation ensemble. b) Mean compressed pulse obtained using an ideal compressor based on the median spectral phase.

lengths, the spectral bandwidth is not sufficient to support shorter pulses. For longer fibers, the pulse acquires considerable higher order chirp components, which cannot be compensated simply by linear compression. The insets in Fig. 5.13 b) show that the compressed pulse develops significant side lobes or even broad low level pedestals if the fiber length is chosen too long. The same calculation for higher input pulse energies or shorter input pulse widths leads to shorter compressed pulse durations, but also the optimum fiber length decreases to impractical dimensions. In addition, the range limit of the chirped mirrors needs to be taken into account, so that the combination of 1.7 nJ pulse energy with 1.7 mm fiber length chosen in the experiment are optimum parameters for the presented setup. Hence the measured pulse duration of 5.0 fs is close to the theoretical limit.

Scalability to single cycle pulse compression

Shorter pulse durations approaching the single optical cycle limit can be obtained by using full phase compensation with active phase shaping. In order to demonstrate the scaling potential of the ANDi PCF based compression scheme, numerical simulations with 4 nJ input pulses are performed, which is the highest pulse energy available in the presented experiment. A fiber length of 10 mm is chosen, for which the SC bandwidth is fully developed. Since fluctuations of the spectral phase due to the noise sensitivity of the SC generation process can limit the achievable pulse duration, we follow the procedure outlined in [28] for simulating a realistic compression experiment including noise-seeded fluctuations.

Input pulse shot noise and spontaneous Raman noise are included into the simulation, as explained in section 3.1.2, and multiple simulations are carried out to obtain an ensemble of 20 independent spectra generated from different noise seeds. The SC spectral phase stability is then characterized by calculating the complex degree of first order coherence $|g_{12}^{(1)}(\lambda, t_1 - t_2 = 0)|$ (3.11), which is critically connected to the compressibility

of the SC pulses. Since it is impossible for a realistic compression device to follow and compensate pulse-to-pulse phase fluctuations, a realistic multi-shot compression experiment is simulated by calculating the median spectral phase over the ensemble and using the corresponding phase conjugate as transfer function of an ideal compressor. The term "ideal compressor" refers to the fact that resolution and bandwidth limits of a real device are not considered here. The procedure yields shot-to-shot distributions of the temporal characteristics of the compressed pulses, from which the average compressed pulse can be calculated that would be expected in a realistic experiment.

Fig. 5.14 a) shows the calculated degree of coherence $|g_{12}^{(1)}(\lambda)|$ as well as the mean generated spectrum. As expected for ANDi PCF, $|g_{12}^{(1)}(\lambda)| = 1$ over the entire bandwidth, which corresponds to perfect coherence and maximum phase stability. Compensating the median spectral phase results in 2.9 fs pulses of excellent quality, as shown in Fig. 5.14 b). Due to the high phase stability of the generated SC, the displayed ensemble averages are virtually undistinguishable from single shot simulations.

These temporal coherence properties of the generated SC in ANDi PCF are distinctly different from SC generated in PCF with single ZDW. Therefore, the fundamental limits to pulse compression outlined in [22, 28, 103, 104] do not apply in this case. The achievable pulse duration is not limited by the coherence properties of the generated SC, but only by the capabilities of the employed compression device and pump laser stability. In addition, there are no limits on input pulse parameters or fiber length to maintain coherence, which means that this concept can also be applied to input pulses with higher energy and longer pulse durations, as was recently demonstrated in [108]. Using a 4 cm long piece of a similar ANDi PCF and 400 fs, 20 nJ input pulses, compression to less than 30 fs was achieved after a simple prism compressor.

5.6. Summary

In the first parts of this chapter, ultra-broadband SC generation in the visible and near-infrared spectral regimes in two different ANDi PCF realizations was presented. The experimental results are in excellent agreement with previous numerical predictions and highlight the exceptional temporal properties of the generated SC pulses. The highly coherent and phase-stable spectrum is only limited by the input pulse stability. The generated SC pulses were temporally characterized with an UTAS measurement and the applicability of the generated SC pulses for the study of molecular dynamics was demostrated. Due to the resulting smooth temporal phase distribution and good coherence properties, ANDi PCFs are suitable even for applications in which fiber-based white light sources are currently hardly used, e.g. in optical parametric amplification, high quality single cycle pulse generation or time-resolved spectroscopy applications.

In the last section of the chapter, ANDi PCF was employed in a nonlinear pulse compression setup and high quality sub-two optical cycle pulses were obtained by applying linear chirp compensation. The results are close to the theoretical limit obtainable using linear compression only. It was numerically demonstrated that the SC temporal coherence

properties allow the scaling of this pulse compression concept down to the single-cycle regime using an active phase shaping device. These results have high immediacy to the research in the field, because the achievable pulse durations and quality in an already existing nonlinear pulse compression setup can be immediately improved by simply using an ANDi PCF for spectral broadening, while the rest of the setup can essentially be left unchanged.

6. Coherent supercontinuum generation in tapered all-normal dispersion fibers

6.1. Photonic nanowires

It was shown in chapter 4 that an all-normal dispersion profile with a maximum at very short wavelengths can be obtained in PCF with extremely small pitch values $\Lambda \approx 500$ nm and relative air-filling ratio approaching unity. In the extreme case of $d/\Lambda = 1$, this corresponds to a pure silica strand with submicron diameter suspended in air. These nanofibers, also called photonic nanowires, are usually obtained by tapering of standard optical fibers. Hence the nanofiber is situated in an optical fiber taper configuration, in which the waist of constant submicron diameter is located between two taper transitions (Fig. 6.1). The strong concentration of the light in the nanowire waist causes high intensities and consequently nonlinear effects that can be order of magnitudes larger than in conventionally sized silica fibers. Therefore, nanowires are a promising candidates to extend the concept of coherent supercontinuum generation in ANDi fibers towards the short wavelength regime, possibly even into the ultraviolet (UV) region.

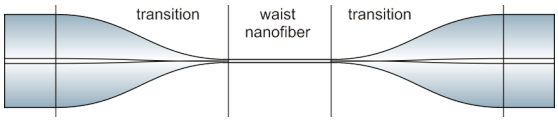

Figure 6.1. – Schematic representation of a photonic nanowire located in the waist of an optical fiber taper configuration [109].

Especially applications in spectroscopy and fluorescence microscopy require light sources in the UV, as many photo-induced processes are excited in this wavelength region [110]. Therefore, recent studies have tried to extend the bandwidth of the generated SC bandwidth on the short wavelength edge [111, 112, 113, 114, 115]. However, none of these approaches succeeded in generating significant spectral power densities below 350 nm wavelength, mainly due to the fact that they rely on dispersive wave generation from soliton effects. This requires phase matching with the original soliton, which is difficult to achieve for short wavelengths. In addition, relatively long fibers are required so that the material losses become significant, which rise sharply for wavelengths below 350 nm. In contrast, the generation of short wavelengths in ANDi fibers is extremely fast and

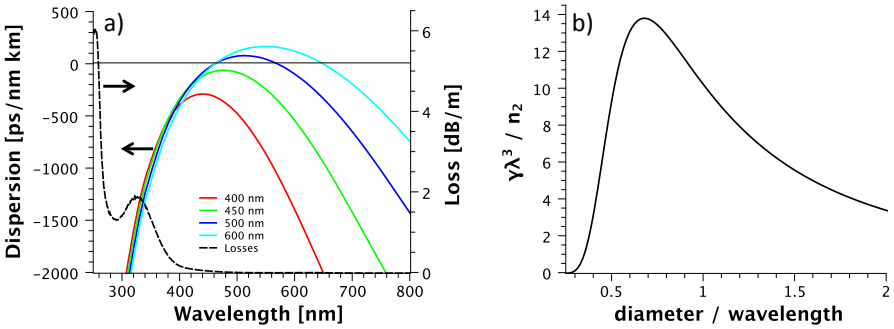

Figure 6.2. – a) Diameter dependent dispersion profiles of photonic nanowires and measured losses of a 105/125 μm, which is taken as the material loss of silica. b) Normalized nonlinearity as a function of diameter for a silica rod in air.

independent of any phase matching condition, and could therefore overcome the present spectral limitations on the short wavelength edge of fiber-generated SCs. The work on optical fiber tapers was done in close collaboration with A. Hartung of IPHT Jena, and the collective results are briefly discussed in this chapter, which was partly published in [109].

Dispersive and nonlinear properties

The dispersion profiles of photonic nanowires (excluding taper transitions) in dependence of their diameter are shown in Fig. 6.2 a), calculated using a fully vectorial FEM mode solver (Comsol Multiphysics). All dispersion and fiber parameter calculations shown in this chapter were performed by A. Hartung. An ANDi profile is obtained for diameters $d < 490$ nm, while the dispersion profile exhibits two ZDWs with increasing separation for larger diameters. The maximum of the dispersion profile shifts towards shorter wavelengths and increasing normal dispersion for decreasing nanofiber diameters. It is located at about 480 nm, -70 ps/(nm km) for 450 nm and at 440 nm, -290 ps/(nm km) for 400 nm fiber diameter. Although not located exactly in the maximum of the dispersion profile, a pump wavelength of 400 nm is convenient for nanowires, because it can easily be generated by frequency-doubling of standard Ti:Sapphire oscillators.

The wavelength dependent loss of a 105/125 μm fiber was measured and is also displayed in Fig. 6.2 a). In the following simulations, this measurement data is used as the material loss of silica. For $\lambda < 400$ nm, it quickly rises to 2 dB/m and even higher to above 6 dB/m for $\lambda < 300$ nm. If a significant SC spectral power density is desired in these wavelength regions, the fiber length needs to be minimized in order to reduce the influence of material losses. The quick broadening dynamics of SC generation in ANDi fibers could therefore prove advantageous for extending the bandwidth of fiber generated SCs into the deep UV region.

In photonic nanowires, a significant part of the modal power is situated in an evanescent field which directly interacts with the silica-air surface of the waist. Any surface roughness, imperfections or contaminations lead to scattering losses in addition to the

material loss. The fraction of modal power in the evanescent field increases for longer wavelengths, and therefore higher losses are expected. For example, loss measurements for a 400 nm diameter taper waist show sharply increasing losses for $\lambda > 700$ nm [116]. In this study, however, the focus lies on the extension of the SC bandwidth into the UV region with high material absorption, where the scattering losses can be ignored due to their relatively small contributions in this region.

The normalized nonlinearity of the nanowire as a function of its diameter is displayed in Fig. 6.2 b). As the diameter of the nanowire decreases, the mode field diameter follows suit and therefore the nonlinearity increases. As the fiber dimensions are further reduced, the evanescent field begins to dominate, the modal power is not tightly confined inside the silica core anymore and the nonlinearity drops sharply [117]. The maximum nonlinearity is reached for a diameter-wavelength ratio of about 0.67. For a pump wavelength of 400 nm, this would correspond to a nanowire diameter of about 270 nm. However, for such small dimensions the dispersion profile is located too deep in the normal regime to expect significant spectral broadening. More realistic are the dimensions already displayed in Fig. 6.2 a). If both fiber diameter and pump wavelength are fixed at 400 nm, γ assumes a value of about 4 $(\mathrm{Wm})^{-1}$, which is more than two orders of magnitude larger than in the case of the PCFs investigated in the previous chapters.

Numerical details

Pulse propagation in the nanofiber is simulated using (3.14) with rigorous treatment of the wavelength dependent nonlinear parameter, implemented using the RK4IPM for integration and the CQEM with $\delta_{Ph} = 10^{-8}$ for adaptive stepping. The full measured loss profile is included into the calculation. The simulation window is divided into 2^{15} bins. A non-chirped hyperbolic secant input pulse intensity profile is assumed, the pump wavelength is fixed at 400 nm.

Although it has been argued that the scalar GNLSE is inadequate for describing ultrashort pulse propagation in waveguides with structures on wavelength-scale and high index contrast [64], in section 6.2 it will be shown that a good agreement between simulated and experimental spectral bandwidth and shape was obtained in tapered suspended core fibers with core diameters similar to the ones discussed here for nanofibers. Therefore, the model is considered sufficient for the fiber parameters discussed in the context of this thesis.

In the case of ANDi PCF, and also in the case of tapered suspended core fibers discussed in section 6.2, it was found that the model with constant nonlinear parameter $\gamma(\omega) = \gamma(\omega_0)$ delivered better agreement with experimental results than the model with varying nonlinear parameter. However, it has not been proven that this observation is generally valid for all situations of SC generation in fibers with ANDi profile, and therefore the frequency dependent variation of γ is included into the model used for the simulation of pulse propagation in nanofibers in this section. Similar to the comparison between the models shown in Fig. 5.4 for ANDi PCF, in the case of nanofibers the differences are mainly located on the long wavelength edge of the spectra, where the model with varying

γ predicts slightly narrower bandwidths. The spectral extent into the UV regime is not affected significantly by the choice of constant or varying nonlinear parameter.

6.1.1. Influence of fiber parameters

In this section, the nanofiber diameter is varied while the input pulse with 100 fs FWHM duration and 1.5 nJ energy at a central wavelength of 400 nm remains unchanged. This corresponds to a peak power of about 13.5 kW. Taper transitions are disregarded here, but their influence is investigated in section 6.1.3.

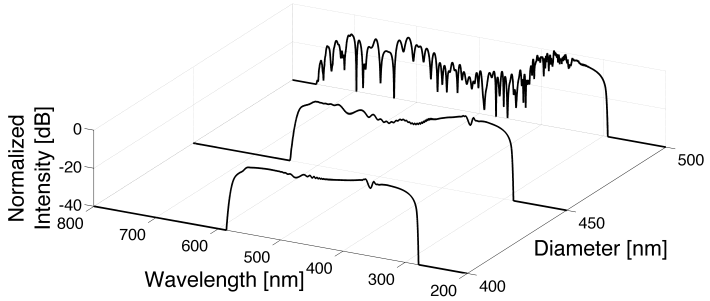

Figure 6.3. – Single-shot simulations of the SC spectra generated in nanofibers with diameters between 400 nm and 550 nm. In all cases, the propagation of a 100 fs, 1.5 nJ pulse through 2 cm of fiber is considered.

Fig. 6.3 shows single-shot simulations of the SC spectra generated in nanofibers with diameters between 400 nm and 550 nm, when the input pulse is propagated over a 2 cm distance inside the fiber. For the fibers with 400 nm and 450 nm diameter, which exhibit an all-normal dispersion profile, the spectrum is smooth and almost rectangular with a flat top and steep edges. In the 400 nm fiber, the spectrum spans over one octave from 280 nm to 580 nm (-20 dB bandwidth). The spectrum generated in the 450 nm fiber is similar, but slightly narrower on the blue side and broader on the red side. In general it can be observed that the spectral extension into the UV wavelengths slightly decreases with increasing fiber diameter. Fundamentally different spectra can be observed in the nanofibers with diameters of 500 nm and above, which have two relatively closely spaced ZDWs. The spectral complexity and fine structure increases significantly, while the bandwidth is extended further towards the visible and near-infrared. In the 500 nm diameter fiber the spectrum spans from ca. 300 nm up to 750 nm wavelength.

The significant differences between the SC spectra generated in nanofibers with ANDi profile and nanofibers with two ZDWs can be explained by fundamentally different dynamics, which are very similar to the dynamics discussed in chapter 4 for PCFs. Fig. 6.4 shows the single-shot spectral evolution over the propagation distance for both 400 nm and 500 nm diameter fibers. The white horizontal lines indicate the ZDWs. The initial evolution is quasi identical for both fibers, because the pump wavelength lies in the normal dispersion regime even for the fibers with two ZDWs. The first few millimeters of propagation are characterized by SPM induced spectral broadening. After ca. 2

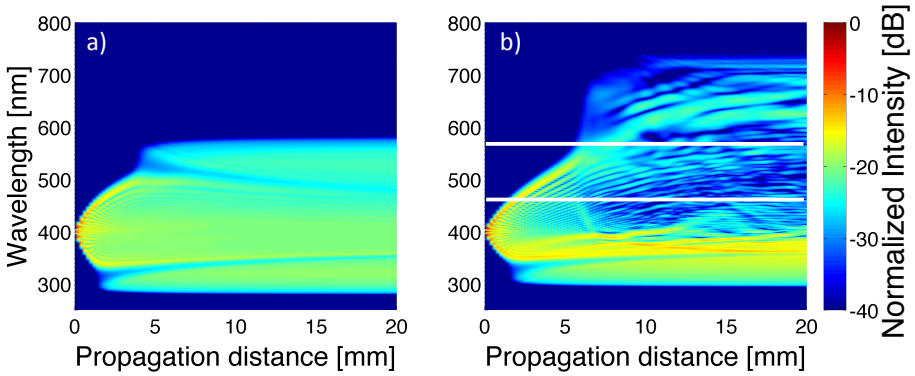

Figure 6.4. – Spectral evolution over a propagation distance of 20 mm of a 100 fs, 1.5nJ pulse in optical nanofibers with (a) 400 nm and (b) 500 nm diameter. The white horizontal lines indicate the position of the zero dispersion wavelengths.

mm, energy is transferred to a wavelength band around 300 nm due to OWB occurring at the trailing edge of the pulse and the associated FWM processes. In the case of the 400 nm diameter fiber, OWB also occurs on the leading pulse edge after ca. 5 mm of propagation, which is evident from the emergence of a 550 nm wavelength band on the red side of the spectrum. The OWB process on both leading and trailing edge is also responsible for the overall smooth appearance of the spectrum in the fibers with ANDi profile. The spectrum reaches a steady state after ca. 10 mm of propagation, whereafter only further smoothening takes place. In the 500 nm diameter fiber, however, SPM induced broadening transfers a significant part of the spectral energy to the anomalous dispersion regime in between the two ZDWs, where OWB is suppressed and instead pulse compression, soliton dynamics and phase matched FWM processes dominate. This leads to a much more irregular spectrum on the long wavelength side and additional variations for further propagation.

These differences in the SC generation dynamics also influence the temporal coherence properties. The transfer of significant energy to the anomalous dispersion region and the associated dynamics in the 500 nm diameter fiber increase the noise sensitivity and consequently the pulse-to-pulse fluctuations of both spectral and temporal profile, as shown in Fig. 6.5. The spectrum remains stable and coherent on the normal dispersion side of the short-wavelength ZDW, but exhibits strong noisy fluctuations and low coherence over the remaining bandwidth. The temporal pulse shape is characterized by a strongly spiking and fluctuating leading edge and a stable tail. The spectrogram computed from a single-shot simulation shown in Fig. 6.6 reveals that the pulse tail is correlated with the coherent short wavelength section of the spectrum. The anomalous dispersion region gives rise to temporal recompression, so that many wavelengths overlap in time and cause the spiking structure on the leading pulse edge. In contrast, the spectrum generated in the 400 nm fiber with ANDi profile is perfectly coherent over the entire bandwidth, does not exhibit pulse-to-pulse fluctuations in neither spectral nor temporal domain and main-

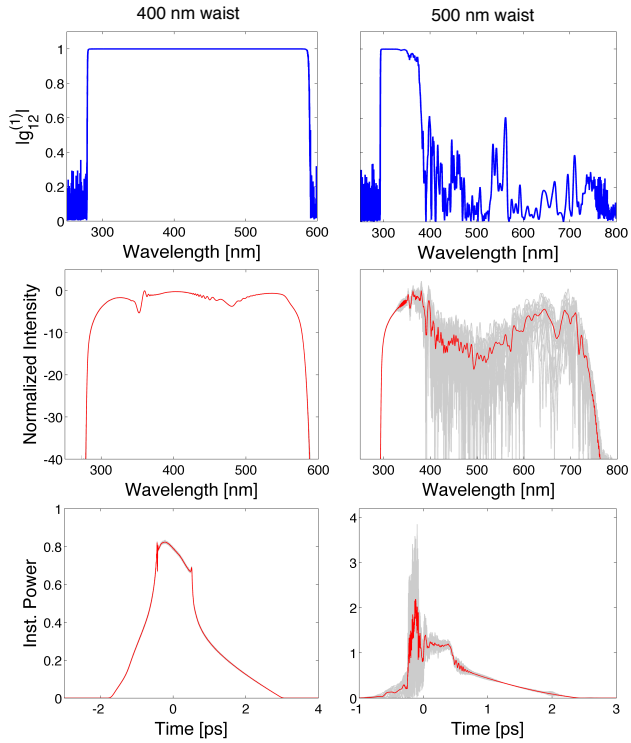

Figure 6.5. – Temporal coherence and stability calculations from an ensemble of 20 individual simulations including noise for the nanofibers with 400 nm and 500 nm diameter. The other fiber and pump pulse parameters are identical to Fig. 6.4. Top: coherence function $|g_{12}^{(1)}|(\lambda)$. Center: individual spectra (grey) and mean spectrum (red). Bottom: individual (grey) and mean temporal pulse profiles (red). For the 400 nm fiber with ANDi profile, the fluctuations are not distinguishable from the mean profiles on the given scales.

tains a well-defined phase distribution. It is therefore possible to temporally recompress the SC generated in the 400 nm fiber down to less than 10 fs even with simple linear chirp compensation if a low level pedestal spanning over ca. 1 ps and containing the short wavelength components is acceptable. Full phase compensation leads to compression approaching the single optical cycle regime. Compression attempts with the SC generated in the 500 nm fiber will result in highly structured, longer and fluctuating pulses.

6.1.2. Influence of pump pulse parameters

In this section, the influence of a variation of input pulse parameters on the properties of the generated SC is investigated. The focus is on fibers with ANDi profile and therefore the nanofiber with 400 nm diameter is used here as representative example.

The bandwidth of the generated SC spectrum broadens asymmetrically towards longer wavelengths if pump pulses with higher peak power are used. Fig. 6.7 a) shows spectra generated with an input pulse duration of 100 fs and varying pulse energies between 0.5

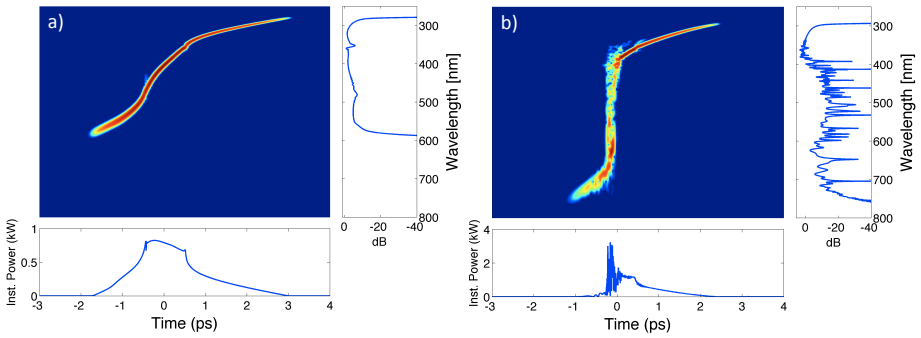

Figure 6.6. – Spectrogram of the resulting supercontinuum pulse after 20 mm of propagation through the nanofibers with diameters of 400 nm (a) and 500 nm (b). A gate pulse with 50 fs duration is used to generate the spectrograms. The colour bar is identical to Fig. 6.4.

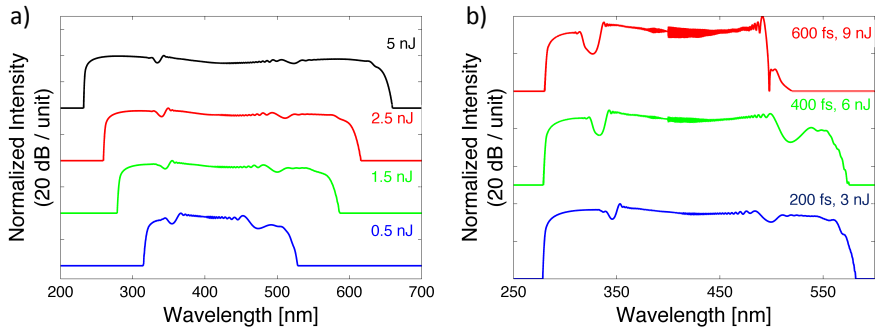

Figure 6.7. – Dependence of the generated spectrum on the input pulse parameters. a) Pulse energy: an input pulse duration of 100 fs and 10 mm propagation distance through a nanofiber with 400 nm diameter are considered. b) Pulse duration: The peak power of 13.5 kW and 20 mm propagation distance through a 400 nm diameter fiber are kept constant in all cases. All spectra are normalized and displayed with an offset to enhance clarity.

- 5 nJ, corresponding to peak powers between 4.5 - 45 kW. For higher pulse energies, the spectrum begins to broaden further into the UV wavelengths below 300 nm. For moderate energies between 1.5 - 2.5 nJ, the blue edge of the spectrum can be expected between 250 - 300 nm, while the spectrum extends even below 250 nm for the highest considered energy of 5 nJ or 45 kW peak power. At this energy, the spectrum spans over more than 400 nm up to 650 nm.

Fig. 6.7 b) shows the generated SC spectra after 20 mm of propagation for input pulse durations of up to 600 fs at a constant peak power of 13.5 kW. The blue wavelength edge is not affected by the change in pump pulse duration and reaches ca. 280 nm in all cases. However, the red wavelength side of the spectrum changes considerably for pulse duration above 400 fs, the spectrum becomes narrower and the spectral structure increases. The origin of the spectral changes is explained by the fact that the spectral broadening dynamics are delayed for the longer pulse durations, as already discussed in

chapter 4 for the case of ANDi PCF. Both SPM and OWB are not only influenced by the peak power of the pulse, but also by the slope of the pump pulse intensity which decreases for longer pulse durations (2.1). OWB on the trailing pulse edge, which leads to the emergence of the wavelength band around 300 nm, only takes place after 10 mm of propagation for the 600 fs, 9 nJ pulse, compared to ca. 2 mm in the case of the 100 fs pulse. OWB on the leading pulse edge is just about to occur after the 20 mm propagation distance considered here, i.e. the displayed spectra generated by longer pump pulses have not reached their steady state yet. However, the spectra will be identical if the propagation distance inside the nanofiber is increased proportional to the pump pulse duration. Therefore, broadband coherent UV supercontinua can in principle be generated even with relatively long pulses around 500 fs if nanofibers with adequate length can be manufactured and sufficient pump pulse energy can be coupled into the fiber.

6.1.3. Influence of taper transitions

Up to now, only pulse propagation in the optical nanofibers was considered. In an experimental setup, however, these nanofibers are typically situated in an optical fiber taper configuration where the waist of constant diameter is located between two taper transitions with varying diameter. It is therefore crucial to investigate the influence of this taper transition on the SC generation dynamics. Clearly, the ideal taper transition should have minimum influence on the temporal and spectral characteristics of the input pulse before it reaches the waist.

A commercially available single mode fiber with initial cladding diameter of 125 micron and 2.9 micron mode field diameter at 400 nm wavelength (Nufern S405-HP) is considered, tapered down to a waist diameter of 400 nm. In principle, two fundamentally different transition shapes can be assessed: (i) an easily manufacturable exponential transition, and (ii) a more complex adiabatic transition.

An adiabatic transition is able to maintain all the power in the fundamental mode HE_{11}, and its shape can be calculated from the local adiabaticity criteria $\mathrm{d}r/\mathrm{d}z = r(\beta_1 - \beta_2)/2\pi$, where r is the cladding radius at distance along the fiber z, and β_1 and β_2 are the propagation constants of the HE_{11} and the first higher order mode with the same azimuthal symmetry HE_{12}, respectively [118]. Due to the cylindrical shape of the fiber, higher order modes with different azimuthal symmetry are not expected [119]. The corresponding calculation for the S405-HP was conducted by A. Hartung and is shown in Fig. 6.8 together with the calculated mode field radius. Clearly, the reduction of the mode field radius is a two step process. Initially, the light propagates in the fiber core with decreasing radius over propagation distance, but as the core size is further reduced, a transition from core to cladding guiding is observed and the mode field radius increases. Finally the mode field follows the decreasing cladding radius to the final nanofiber size.

Fig. 6.8 also displays the corresponding exponential transition together with the behavior of the mode field radius. While the transition from core to cladding guiding in the

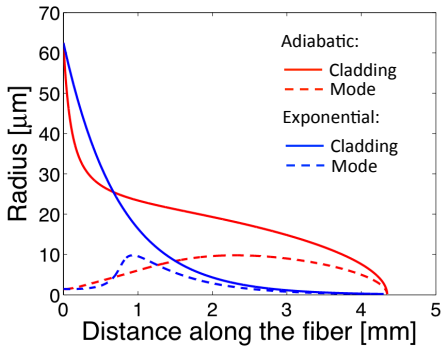

Figure 6.8. – Cladding diameter and mode field radius for light with 400 nm wavelength in adiabatic and corresponding exponential taper transitions. Considered is the tapering of the single mode fiber Nufern S405-HP from its initial radius of 62.5 μm to a taper waist of 200 nm radius.

adiabatic transition is continuous and smooth, the core cut-off in the exponential transition occurs quite suddenly around 1 mm distance. The subsequent continuous reduction of the cladding diameter leads to a prolonged section with very small mode field area before the actual taper waist is reached. The resulting large nonlinearities can significantly alter the spectral and temporal properties of the input pulse before it reaches the waist. In contrast, the adiabatic transition minimizes the sections with small mode field diameters and consequently is expected to give a much better performance in delivering the input pulse to the waist as undistorted as possible.

The 100 fs input pulse with 5 nJ energy considered above is chosen to evaluate the performance of the taper transitions. The behaviour of the mode field radius illustrated in Fig. 6.8 is used for the calculation of A_{eff}, which is then included into the simulation. For cladding diameters $d_{\text{clad}} > 1.5\mu$m, the fiber dispersion is assumed to be identical to the material dispersion of silica and the frequency variation of the nonlinear parameter is neglected, i.e. $\bar{\gamma}(\omega) = \bar{\gamma}(\omega_0)$ in (3.14). This is a good approximation, because the dependence of the GVD on the cladding diameter around the pump wavelength of 400 nm is negligible for larger diameters and the spectral bandwidth of the propagating pulse is still narrow. For $\mathrm{d}_{\text{clad}} < 1.5\mu$m, the dispersion profile and frequency dependent A_{eff} are calculated in diameter steps of 50 nm and fully included into the simulation.

In Fig. 6.9, the simulated pulse properties at the end of adiabatic and exponential transitions with 4.3 mm length are shown, which is the shortest theoretically possible adiabatic transition length for the S405-HP. Clearly, the propagation through the exponential transition drastically changes the characteristics of the input pulse. The spectrum has broadened to more than 100 nm bandwidth due to SPM in the small diameter sections of the transition and the temporal pulse shape shows clear signatures of nonlinear distortion, such as the steepening of the trailing pulse edge. The peak power drops from the initial 45 kW to less than 30 kW. In contrast, the characteristics of the pulse propagating through the adiabatic transition are conserved to a large extent. Spectral broadening

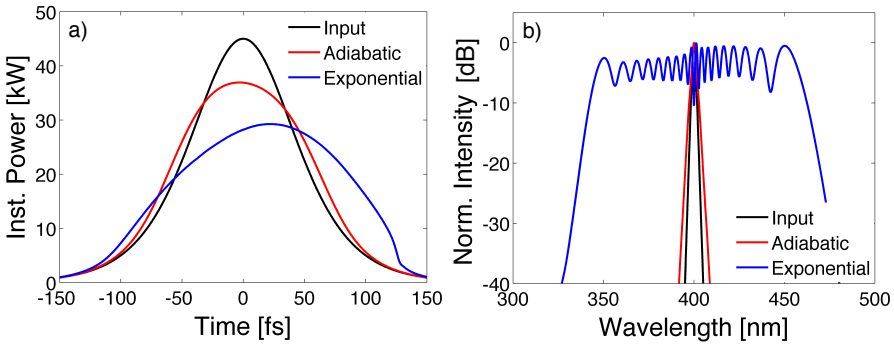

Figure 6.9. – Influence of adiabatic and exponential transition on temporal pulse shape (a) and spectrum (b) of the input pulse.

is only noticeable on a logarithmic scale and the temporal pulse shape exhibits only a small amount of dispersive broadening, reducing the peak power to about 38 kW. Consequently, the adiabatic transition does not change the properties of the generated SC in the complete taper significantly in comparison with the pure nanofiber, while the serious reduction of peak power and pulse distortion in the exponential transition reduces the achievable spectral width of the SC generated in the taper waist.

Note that here an exceptionally short transition was considered, which is extremely challenging to manufacture, and the performance difference between the two transition shapes is already remarkable. In reality, the transition shape will be chosen longer in order to relax manufacturing difficulties, which will increase the distortions of the input pulse even further for the exponential transition. Clearly, the exponential shape is unsuitable for the delivery of ultrashort pulses to submicron diameter taper waists, because the characteristics of the generated SC are increasingly determined by the properties of the transition instead of the carefully designed dispersion profile of the taper waist. Therefore, every effort should be made in the taper drawing process to achieve an adiabatic transition with steep angles at the critical sections, i.e. initial core cut-off and final reduction to nanofiber waist size where the mode field area is small before it reaches the waist. Numerical simulations have confirmed that the transition allows coherent SC generation below 300 nm wavelength even if it is several centimeters long, as long as the basic adiabatic shape is maintained, and input pulse and waist parameters are carefully chosen.

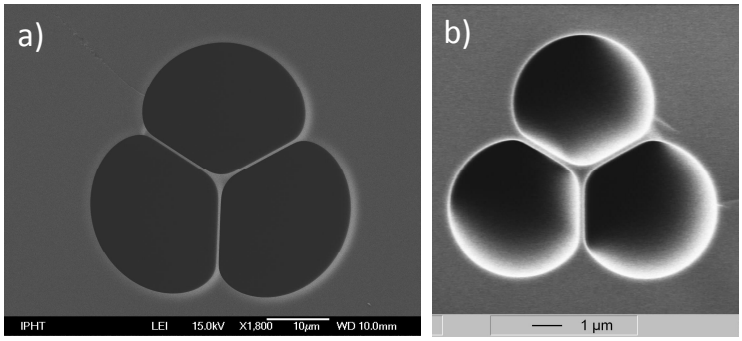

Figure 6.10. – Scanning electron microscope picture of the suspended core fiber used in the subsequent experiments. a) before tapering: the core has an incircle core diameter of 2 μm. b) after tapering: the core has an incircle diameter of 540 nm. Pictures courtesy of A. Dellith (IPHT).

6.2. Suspended core fibers

It was shown in the previous section that optical nanofibers are promising candidates for coherent SC generation in the ultraviolet spectral regime. However, the experimental realization may prove difficult mainly due to the short required taper transitions with complex shape, which are hard to manufacture. A more favorable experimental approach can be expected in suspended core fibers. In these fibers, a core with a diameter of a few micron is suspended in air in the central section of a fiber, connected to the walls typically via three or more silica bridges. A SEM picture of the cross section of a fiber with 2 μm incircle core diameter, which is the diameter of the biggest circle that fits entirely into the core, is shown in Fig. 6.10 a). The fiber was drawn in-house at the IPHT and is used in the following experiments.

Since the core is mostly surrounded by air, similar properties to freestanding nanofibers are expected. In addition, the suspended core design offers the following advantages when tapering is considered:

- the high refractive index difference between the core and the surrounding air cladding prevents the transition from core to cladding guiding, which allows shorter taper transitions in comparison to all-solid designs;
- a tapering ratio of only roughly 1:3 is required to reach core diameters in the order of 500 nm, which can be realized in transitions of only a few millimeters length;
- the tapered core is protected by the surrounding silica cladding, which offers improved stability compared to the freestanding nanofiber and protection against surface contamination.

6.2.1. Dispersion properties

In order to investigate how the dispersive properties are influenced by tapering, the experimentally available fiber design of Fig. 6.10 a) is modeled by A. Hartung with a

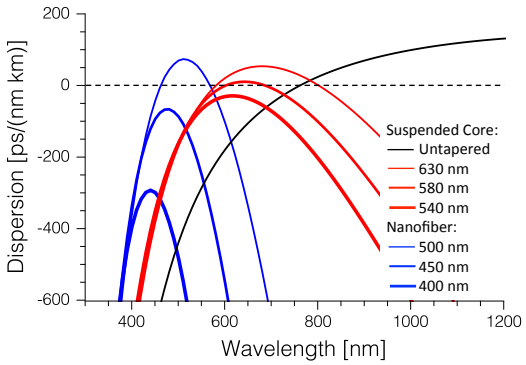

Figure 6.11. – Dependence of fundamental mode dispersion profiles on (incircle) core diameter for suspended core fibers and pure silica nanofibers.

fully vectorial FEM mode solver (Comsol Multiphysics) and scaled down to a smaller geometry to imitate the results of the tapering process. The results are displayed in Fig. 6.11. The dispersion profile for the fundamental mode of the untapered fiber has a single ZDW at about 750 nm wavelength. It is important to note that the untapered fiber is not single-mode, a total of 13 modes are supported by the geometry.

The calculation results for the fundamental modes of the tapered geometries reveal remarkable differences between freestanding nanofibers and suspended core fibers for the position of minimum GVD, which is shifted for suspended core fibers into the region of 600 - 650 nm. It was shown in chapter 5 that pumping close to the minimum GVD results in the broadest bandwidth of the generated SC. Therefore, both types of optical fibers give access to quite different wavelength ranges for coherent SC generation. The required fiber diameters for obtaining an ANDi profile also show significant differences. While the diameter of the freestanding nanofiber has to be below 480 nm, an incircle diameter of 570 nm is sufficient to obtain all-normal dispersion suspended core fibers. Therefore, the suspended core fiber has to be tapered only by a factor of roughly 1:3.5 in order to reduce the incircle diameter from the initial 2000 nm to the required value, which can be realized with a taper transition of just a few millimeters.

The original fiber was scaled down by a factor of 1:3.7 to achieve all-normal dispersion at an incircle diameter of 540 nm. The taper was drawn by A. Hartung at the facilities of the IPHT in Jena with a CO_2 laser heating method described in detail in [119]. The final suspended core fiber taper geometry consists of a 70 mm long waist with 3 mm taper transitions at both ends and 2 mm untapered fiber at the input and output side. A SEM image of the suspended core fiber after the tapering process is shown in Fig. 6.10 b) and comparison with the untapered fiber confirms that the geometry of the fiber was well conserved.

According to the FEM calculations, the tapered waist section can support two modes. However, the second order mode is quite lossy and has a very different dispersion profile compared to the fundamental mode. The dispersion is also normal at all wavelength, but acquires its maximum at 460 nm with a high value of -430 ps/(nm km) compared to the

dispersion of the fundamental mode of > -100 ps/(nm km) at the pump wavelength. If parts of the input pulse are coupled into this mode, the fast temporal broadening prevents a significant contribution to the SC generation dynamics.

6.2.2. Experiments and discussion

The experimental setup is identical to the one described section 5.3, i.e. the tunable Coherent OPerA optical parametric amplifier is used to generate input pump pulses of ca. 50 fs duration. The OPA was set to a wavelength of 625 nm, which is close to the maximum of the dispersion profile for the tapered suspended core fiber taper. The experimental data was recorded by A. Hartung.

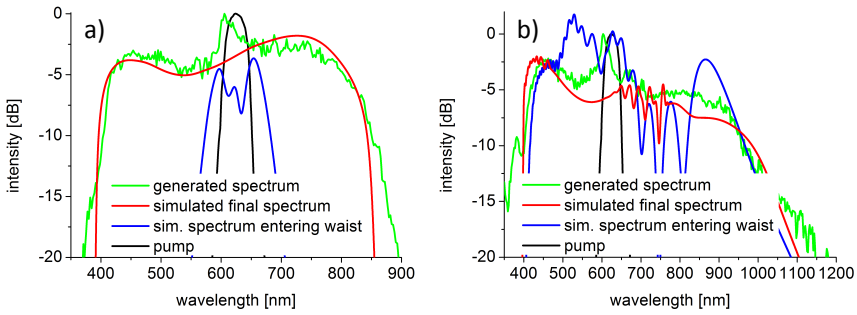

Figure 6.12. – Measured supercontinuum spectrum at output pulse energy of 1.3 nJ and comparison with numerical simulations. The spectrum in a) is mainly generated in waist, while b) is mainly generated in untapered initial piece of fiber

The maximum transmitted pulse energy measured at the taper end before end face destruction was 1.3 nJ. At this energy two distinctly different SC spectra could be generated as seen in Fig. 6.12 just by slightly moving the input coupling optics. In order to clarify the differences in the generated spectra, pulse propagation through the taper geometry was numerically modeled. The model is identical to the previous sections, the nonlinear parameter was assumed to be constant $\gamma = \gamma(\omega_0)$, because better agreement with the experiments could be achieved. This point was already discussed in section 5.3.1. The taper geometry was idealized by starting the pulse propagation in 2 mm of untapered fiber, instantaneously followed by the taper waist and the final untapered fiber section. Due to its short length, the transition between the untapered fiber and the waist section was thus neglected.

The spectrum in Fig. 6.12 a) has a smooth spectral intensity profile and three peaks can be identified around 450 nm and 750 nm, as well as around the pump wavelength of 625 nm. Ranging from 370 nm to 895 nm, a more than octave-spanning spectral bandwidth of 525 nm at the -20 dB level was achieved. The spectrum could be reproduced reasonably well by simulation assuming that the transmitted energy of 1.3 nJ was launched initially into the fundamental mode of the untapered fiber and transmitted into the waist section.

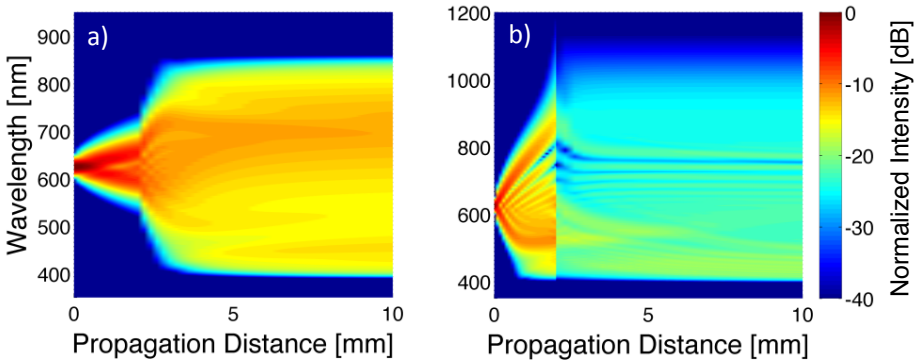

Figure 6.13. – Spectral evolution during propagation a) for the narrow but flat top spectrum mainly generated in the waist and b) the wide spectrum mainly generated in the 2 mm untapered input piece of fiber

Since in separate experiments with the untapered fiber it was possible to launch about 10 nJ pulse energy, it is plausible that higher order modes of the untapered fiber were initially excited and lost in the taper transition. The peak around the pump wavelength could not be reproduced by simulations and is assumed to originate from a small contribution of the second order mode of the taper waist. The short untapered initial part of the fiber contributes only a small amount to the spectral broadening, as seen by the simulated spectrum entering the waist (Fig. 6.12 a) and the simulated spectral evolution (Fig. 6.13 a). Nonlinear processes become significant only when the optical pulse reaches the taper waist. The broadening dynamics are therefore dominated by the all-normal dispersion properties of the waist, where SPM and OWB lead to a flat and smooth octave-spanning spectrum. The spectrogram after 10 mm propagation is shown in Fig. 6.14 a) and is very similar to the ANDi PCF spectrograms of chapter 4. The calculated coherence $g_{12}^{(1)}(\lambda)$ = 1 for the entire bandwidth.

The spectrum in Fig. 6.12 b) ranges from 350 nm to 1150 nm at the -20 dB level. Thus especially on the long wavelength side it is broader than the spectrum in Fig. 6.12 a), but in contrast it does not exhibit a smooth and flat profile but shows significant spectral variations. The main features of the spectrum can be reproduced by the simulation assuming that the entire 10 nJ of energy were initially coupled into the fundamental mode of the untapered fiber and losses occurred at the taper transition resulting in the final 1.3 nJ within the waist. The high energy of 10 nJ leads to an extraordinary SPM-dominated broadening already in the short untapered piece of fiber, indicated by the simulated spectrum entering the waist (Fig. 6.12 b) and the simulated spectral evolution (Fig. 6.13 b). When this broadband pulse reaches the waist and losses are taken into account, only additional spectral smoothing takes place. Therefore, the SC generation dynamics are dominated by the properties of the untapered suspended core fiber with its ZDW around 750 nm. Although energy is transported into the anomalous dispersion regime, no significant soliton dynamics can occur due to the quick transition to the all-normal dispersion of the taper waist. Therefore, the spectrum exiting the fiber is also

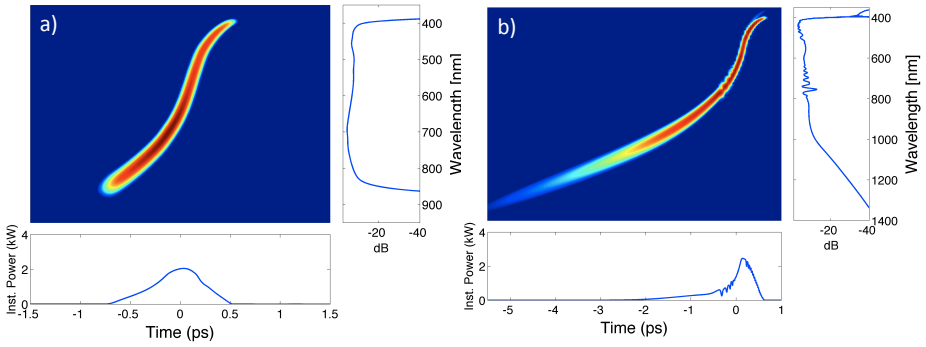

Figure 6.14. – Simulated spectrogram of the SC pulse after 10 mm of propagation through the suspended core taper for the two characteristic spectra a) and b) discussed in Figs. 6.12 and 6.13.

highly coherent over the entire bandwidth. The spectrogram in Fig. 6.14 reveals that also in this case a single pulse is maintained in the time domain, but a long tail containing the long wavelength components is formed, which spans over more than 5 ps.

By performing numerical simulations with the higher order modes of both untapered and tapered fiber it could be established that the fundamental mode dispersion profile is essential for obtaining the experimentally measured spectral bandwidth. The analysis given above can explain the origin of the different spectra, but the assumption of different losses of the fundamental mode in dependence of the guided energy remains an inconsistency, which has to be investigated in future experiments. It is clear from these experiments, however, that the input coupling section needs to be minimized in order to take full advantage of the ANDi profile of the waist, especially for higher pulse energies.

6.2.3. Outlook

Coherent visible SC generation in ANDi tapered suspended core fibers was successfully demonstrated in this section and the advantages compared to freestanding nanofibers were discussed. However, it would be interesting to develop ANDi fibers with dispersion profiles close to the ones of nanofibers to be used for UV SC generation while keeping the advantages of the suspended core geometry. Therefore, the influence of different suspended core fiber designs on the dispersion profile was investigated with FEM calculations [82]. The results are summarized in Fig. 6.15. Displayed is the position of the maximum of the dispersion profile in dependence of the fiber design and the diameter of the fiber. All the calculated profiles are convex, so that an ANDi profile is implied if the maximum is located at $D < 0$ and a profile with two ZDWs if $D > 0$. Similar to the dispersion profiles in Fig. 6.11, the maximum shifts towards lower values of D and shorter wavelengths for smaller fiber diameters for all the investigated designs. It is interesting to note that the dispersion profile depends critically on the geometry of the fiber core. The closer the core geometry resembles a circular shape, the more the dispersion profile is shifted to shorter wavelengths and converges towards the dispersion of the

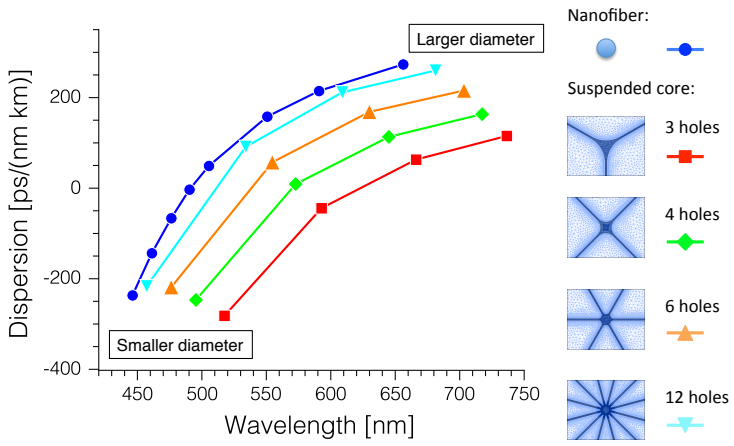

Figure 6.15. – Position of the maximum of the dispersion profile in dependence of the fiber design and the diameter of the fiber. All calculated profiles are convex, so that an ANDi profile is implied if the maximum is located at $D < 0$ and a profile with two ZDWs if $D > 0$.

freestanding nanofibers. If the number of cladding air holes is increased from three to six, the maximum of the dispersion profile shifts about 100 nm to the region around 550 nm wavelength. A further increase in the number of cladding air holes leads to further shifts towards shorter wavelengths, but with smaller increments and increasing manufacturing difficulty. A tapered suspended core fiber design with six cladding air holes is therefore a promising candidate to extend the spectral extent of the generated SC further towards the UV range while keeping a reasonably well manufacturable design.

7. Conclusion and Outlook

The main objective of this thesis was the development of optimized fiber designs for pulse-preserving and spectrally uniform broadband coherent SC generation for ultrafast time-resolved applications. The conventional approach of anomalous dispersion pumping produces ultra-broadband spectra by exploiting pulse break-up by soliton fission, but the existence of noise-seeded MI in the anomalous dispersion regime puts strict criteria in place regarding the soliton number of the input pulse or the fiber length in order to conserve coherence. The main challenge of this work was therefore to find a way to suppress the unwanted pulse break-up and noise sensitivity, while still maintaining ultra-broad bandwidths.

In an extensive numerical study it was shown that an approach using the special design possibilities of PCF to create fibers with optimized all-normal dispersion profiles can achieve the objective. Femtosecond pumping of fibers exhibiting convex and flattened ANDi profiles with minimum GVD at the pump wavelength was shown to produce more than octave-spanning spectra, which are perfectly coherent over the entire bandwidth. Fiber and input pulse parameters can be adjusted to maximize spectral bandwidth or uniformity, and continuously high spectral power densities with flatness of better than $\pm$ 1dB can be achieved. SPM and OWB were identified as the dominant nonlinear effects in the SC generation dynamics, which produce smooth spectral and temporal profiles without significant fine structure and conserve a single recompressible pulse in the time domain with stable phase distribution. Working entirely in the normal dispersion regime suppresses MI and minimizes noise sensitivity. In contrast to SC generation involving soliton dynamics, no limitations on input pulse parameters or fiber length exist to maintain coherence in the SC generation process in ANDi fibers. A wide range of input pulse parameters is suitable for ultra-broadband coherent SC generation in these fibers, and in fact the coherence properties, spectral bandwidth and temporal compressibility are independent of input pulse duration for constant peak power. The results of this thesis therefore overcome the common perception that there is a trade-off between high coherence and broad bandwidth of the generated SC for pump pulses with a few hundred femtoseconds duration.

These numerical results were confirmed in experiments with two realizations of ANDi PCF. In the fiber with minimum normal GVD at 1050 nm, the broadest SC spectra generated in the normal dispersion regime of an optical fiber to date could be demonstrated, spanning over 900 nm or almost 1.5 octaves. The required pulse parameters are achievable with modern Ytterbium doped fiber lasers, making highly coherent ultra-broadband SC generation possible in all-fiber designs. It was also shown that pumping on

the steep flanks of the dispersion profile leads to asymmetric broadening towards the side with decreasing GVD, which can be used to effectively steer the broadening dynamics towards a desired wavelength range for a given pump wavelength. In a second realization of an ANDi PCF with minimum GVD around 650 nm, coherent SC generation spanning the entire visible and partly the near-infrared spectrum was experimentally achieved, demonstrating the versatility of the concept.

In further experiments, the conservation of a single pulse in the time domain was demonstrated using the generated SC as the probe pulse in ultrafast transient absorption spectroscopy. This achievement proves that SCs generated in ANDi PCFs are applicable to the study of time-resolved molecular dynamics and in fact offer multiple advantages over bulk generated SCs, such as order of magnitude lower required pump power, high conversion efficiency and the possibility of probing in the direct vicinity of the pump wavelength. The excellent phase stability of the SC pulses was further exploited in a nonlinear compression experiment, in which the SC spectrum obtained in a short piece of ANDi fiber with pump pulses from a Ti:Sapphire oscillator could be compressed to pulses of 5.0 fs duration with excellent quality by linear chirp compensation only. It was numerically shown that even shorter pulse durations approaching the single cycle limit can be generated using full phase compensation. In contrast to earlier compression demonstrations with single ZDW PCF, the achievable pulse duration and quality is not limited by the SC coherence properties and the concept is scalable to longer input pulse durations and fiber lengths.

The concept of broadband coherent SC generation was further extended into the UV regime by using the design flexibility of tapered optical fibers. It was shown numerically that octave-spanning coherent SC generation with significant spectral power densities at UV wavelengths is possible in freestanding optical nanofibers with submicron diameter and all-normal dispersion profile. In contrast to previous studies using solitonic dispersive wave dynamics, the generation of short wavelengths in ANDi fibers is independent of any phase matching condition, and could therefore overcome the present spectral limitations on the short wavelength edge of fiber-generated SCs. Additionally, the fast dynamics enable the use of short fiber lengths, making it feasible to generate coherent SCs with significant spectral power densities below 300 nm wavelength. Although the taper transitions necessary for efficient input coupling into the nanofibers can distort the pump pulses, an adiabatic transition shape was shown to minimize both nonlinear and dispersive effects on the pump pulse before it reaches the taper waist. Extremely short transitions and increased environmental stability are offered by tapered suspended core fibers. The concept of SC generation in tapered fibers with ANDi profile could be experimentally demonstrated using a fiber with suspended core design, resulting in a smooth spectral profile spanning from 400 nm - 850 nm. Further developments in suspended core fiber design and fabrication can shift the achievable bandwidth further to short wavelengths and should result in an environmentally stable coherent UV light source.

While coherent SC generation in normal dispersion fibers has been demonstrated previously, the work contained in this thesis pushes this concept to new dimensions. The

theoretical understanding of the involved dynamics and the development of clear design criteria has made it possible to increase the bandwidth of normal dispersion SCs to magnitudes previously only known from anomalous dispersion pumping. At the same time, these spectra benefit from low noise-sensitivity, smooth and uniform spectral and temporal profiles, absence of spectral fine-structure as well as recompressible phase distribution, which are characteristic to normal dispersion pumping. The possibility to achieve these characteristics with relatively long pump pulses and the relaxation of previously demanding pump source requirements to maintain coherence increases availability and applicability of broadband coherent SC sources.

The ANDi fiber design concept is an important complement to the fibers with single ZDW conventionally used for SC generation, and both have their unique advantages and drawbacks. Ultimately, the choice of fiber design depends on the application demands. The ANDi design is preferable if coherence, phase stability and spectral flatness are required, but for a given input peak power the achievable spectral bandwidth is narrower in comparison to anomalous dispersion pumping. For applications in which the coherence properties and the presence of fine structure are unimportant, the classic approach of anomalous dispersion pumping close to the single ZDW still provides the broadest achievable spectral bandwidth and allows pump sources from the femtosecond to the CW regime. ANDi fibers do not offer the same flexibility in the choice of pump source, the high peak powers required for substantial spectral broadening put a practical limit on the pump pulse duration and imply a femtosecond pulse source. However, it was detailed in chapter 4 that broader spectra can be achieved by flatter dispersion slopes. It will therefore be a future challenge to design ANDi fibers with ultraflat dispersion profiles, which will allow substantial spectral broadening also for lower peak power pulses in the picosecond regime.

In this thesis, ANDi fibers for coherent SC generation in the near-infrared, visible and UV wavelengths were presented. It was mentioned, however, that the extension of the achievable bandwidth towards the mid-infrared (mid-IR) is limited with the traditional silica PCF designs. However, there is an emerging requirement for coherent sources of mid-IR radiation, i.e. wavelengths longer than 2 microns, for a range of applications in the life sciences, chemical sciences and physics. Current techniques to generate mid-IR radiation, such as thermal or laser sources, cover only a relatively narrow spectral range or offer only very low output power. The transfer of the concept of SC generation in ANDi fibers to the mid-IR region could therefore create an additional source of robust and coherent broad bandwidth light in this wavelength region.

Ultimately, a new degree of freedom needs to be introduced in order to realize ANDi fiber designs beyond 2 μm: the fiber material. Soft glass materials offer low losses in the mid-IR and ZDWs between 1.6 μm for fluoride and 4.8 μm for chalcogenide glasses. The variety of available soft glass materials provides a whole new dimension for the design of ANDi fibers in mid-IR wavelengths, because dispersion design flexibility is not only given by the inclusion of air hole microstructures, but also by combining layers of glass materials with different characteristics in all-solid designs. In addition, soft glasses

typically offer orders of magnitude larger nonlinearity than silica, enabling the use of much lower peak power pump pulses to obtain similar dynamics and bandwidths. As a result, a wide range of potential applications can be identified for broadband coherent SC sources based on soft glass fibers with ANDi profile, including bio-chemical absorption spectroscopy, the generation of seed pulses for mid-IR optical parametric chirped pulse amplification systems to be used in high harmonic generation experiments and the development of coherent transmission sources for the next generation telecommunications networks. Broadband coherent SC generation is also the key enabling technology for extending metrology applications towards the mid-IR spectral regime.

By resolving several challenges regarding coherence properties, stability, uniformity, temporal profile and spectral bandwidth of fiber-based SC sources, the work contained in this thesis therefore lays the foundation for future advancements in fundamental science and modern technology.

Bibliography

[1] J. C. Knight, T. A. Birks, P. S. J. Russell, and D. M. Atkin, "All-silica single-mode optical fiber with photonic crystal cladding," Opt. Lett. **21**, 1547–1549 (1996).

[2] J. C. Knight, "Photonic crystal fibers," Nature **424**, 847–851 (2003).

[3] P. Russell, "Photonic crystal fiber," Science **299**, 358 (2003).

[4] J. Ranka, R. Windeler, and A. Stentz, "Efficient visible continuum generation in air-silica microstructure optical fibers with anomalous dispersion at 800 nm," in "Lasers and Electro-Optics, 1999. CLEO '99. Summaries of Papers Presented at the Conference on," (1999), pp. CPD8/1 –CPD8/2.

[5] J. K. Ranka, R. S. Windeler, and A. J. Stentz, "Visible continuum generation in air-silica microstructure optical fibers with anomalous dispersion at 800 nm," Opt. Lett. **25**, 25–27 (2000).

[6] R. R. Alfano and S. L. Shapiro, "Emission in the region 4000 to 7000 Å via four-photon coupling in glass," Phys. Rev. Lett. **24**, 584–587 (1970).

[7] C. Lin and R. Stolen, "New nanosecond continuum for excited-state spectroscopy," Appl. Phys. Lett. **28**, 216–218 (1976).

[8] R. Alfano, *The supercontinuum laser source* (Springer, New York, 2006).

[9] D. Mogilevtsev, T. A. Birks, and P. S. J. Russell, "Group-velocity dispersion in photonic crystal fibers," Opt. Lett. **23**, 1662–1664 (1998).

[10] J. Knight, J. Arriaga, T. Birks, A. Ortigosa-Blanch, W. Wadsworth, and P. Russell, "Anomalous dispersion in photonic crystal fiber," IEEE Phot. Tech. Lett. **12**, 807 –809 (2000).

[11] N. G. R. Broderick, T. M. Monro, P. J. Bennett, and D. J. Richardson, "Nonlinearity in holey optical fibers: measurement and future opportunities," Opt. Lett. **24**, 1395–1397 (1999).

[12] T. A. Birks, J. C. Knight, and P. S. Russell, "Endlessly single-mode photonic crystal fiber," Opt. Lett. **22**, 961–963 (1997).

[13] L. Provino, J. Dudley, H. Maillotte, N. Grossard, R. Windeler, and B. Eggleton, "Compact broadband continuum source based on microchip laser pumped microstructured fibre," Electronics Letters **37**, 558 –560 (2001).

[14] J. M. Dudley, L. Provino, N. Grossard, H. Maillotte, R. S. Windeler, B. J. Eggleton, and S. Coen, "Supercontinuum generation in air–silica microstructured fibers with nanosecond and femtosecond pulse pumping," J. Opt. Soc. Am. B **19**, 765–771 (2002).

[15] B. A. Cumberland, J. C. Travers, S. V. Popov, and J. R. Taylor, "29 W High power CW supercontinuum source," Opt. Express **16**, 5954–5962 (2008).

[16] S. Coen, A. H. L. Chau, R. Leonhardt, J. D. Harvey, J. C. Knight, W. J. Wadsworth, and P. S. J. Russell, "White-light supercontinuum generation with 60-ps pump pulses in a photonic crystal fiber," Opt. Lett. **26**, 1356–1358 (2001).

[17] D. A. Sidorov-Biryukov, E. E. Serebryannikov, and A. M. Zheltikov, "Time-resolved coherent anti-stokes raman scattering with a femtosecond soliton output of a photonic-crystal fiber," Opt. Lett. **31**, 2323–2325 (2006).

[18] I. Hartl, X. D. Li, C. Chudoba, R. K. Ghanta, T. H. Ko, J. G. Fujimoto, J. K. Ranka, and R. S. Windeler, "Ultrahigh-resolution optical coherence tomography using continuum generation in an air–silica microstructure optical fiber," Opt. Lett. **26**, 608–610 (2001).

[19] S. Smirnov, J. Ania-Castanon, T. Ellingham, S. Kobtsev, S. Kukarin, and S. Turitsyn, "Optical spectral broadening and supercontinuum generation in telecom applications," Optical Fiber Technology **12**, 122 – 147 (2006).

[20] J. Ye and S. Cundiff, *Femtosecond Optical Frequency Comb Technology* (Springer Science + Business Media, 2005).

[21] T. Udem, R. Holzwarth, and T. W. Hänsch, "Optical frequency metrology," Nature **416**, 233–237 (2002).

[22] J. M. Dudley and S. Coen, "Coherence properties of supercontinuum spectra generated in photonic crystal and tapered optical fibers," Opt. Lett. **27**, 1180–1182 (2002).

[23] J. Herrmann, U. Griebner, N. Zhavoronkov, A. Husakou, D. Nickel, J. Knight, W. Wadsworth, P. S. J. Russell, and G. Korn, "Experimental evidence for supercontinuum generation by fission of higher-order solitons in photonic fibers," Phys. Rev. Lett. **88**, 173901 (2002).

[24] K. L. Corwin, N. R. Newbury, J. M. Dudley, S. Coen, S. A. Diddams, K. Weber, and R. S. Windeler, "Fundamental noise limitations to supercontinuum generation in microstructure fiber," Phys. Rev. Lett. **90**, 113904 (2003).

[25] J. M. Dudley, G. Genty, and S. Coen, "Supercontinuum generation in photonic crystal fiber," Rev. Mod. Phys. **78**, 1135–1184 (2006).

[26] X. Gu, L. Xu, M. Kimmel, E. Zeek, P. O'Shea, A. P. Shreenath, R. Trebino, and R. S. Windeler, "Frequency-resolved optical gating and single-shot spectral measurements reveal fine structure in microstructure-fiber continuum," Opt. Lett. **27**, 1174–1176 (2002).

[27] X. Gu, M. Kimmel, A. Shreenath, R. Trebino, J. Dudley, S. Coen, and R. Windeler, "Experimental studies of the coherence of microstructure-fiber supercontinuum," Opt. Express **11**, 2697–2703 (2003).

[28] J. Dudley and S. Coen, "Fundamental limits to few-cycle pulse generation from compression of supercontinuum spectra generated in photonic crystal fiber," Opt. Express **12**, 2423–2428 (2004).

[29] T. Udem, J. Reichert, R. Holzwarth, S. Diddams, D. Jones, J. Ye, S. Cundiff, T. Hänsch, and J. Hall, "A new type of frequency chain and its application to fundamental frequency metrology," in "The Hydrogen Atom: Precision Physics of Simple Atomic Systems," , vol. 570 of *Lecture Notes in Physics*, S. Karshenboim, F. Pavone, G. Bassani, M. Inguscio, and T. Hänsch, eds. (Springer, Berlin, 2000), pp. 125–144.

[30] K. M. Hilligsøe, T. Andersen, H. Paulsen, C. Nielsen, K. Mølmer, S. Keiding, R. Kristiansen, K. Hansen, and J. Larsen, "Supercontinuum generation in a photonic crystal fiber with two zero dispersion wavelengths," Opt. Express **12**, 1045–1054 (2004).

[31] M. Frosz, P. Falk, and O. Bang, "The role of the second zero-dispersion wavelength in generation of supercontinua and bright-bright soliton-pairs across the zero-dispersion wavelength," Opt. Express **13**, 6181–6192 (2005).

[32] E. R. Andresen, H. N. Paulsen, V. Birkedal, J. Thøgersen, and S. R. Keiding, "Broadband multiplex coherent anti-stokes raman scattering microscopy employing photonic-crystal fibers," J. Opt. Soc. Am. B **22**, 1934–1938 (2005).

[33] P. Falk, M. Frosz, and O. Bang, "Supercontinuum generation in a photonic crystal fiber with two zero-dispersion wavelengths tapered to normal dispersion at all wavelengths," Opt. Express **13**, 7535–7540 (2005).

[34] K. Mori, H. Takara, S. Kawanishi, M. Saruwatari, and T. Morioka, "Flatly broadened supercontinuum spectrum generated in a dispersion decreasing fibre with convex dispersion profile," Electronics Letters **33**, 1806 –1808 (1997).

[35] G. Genty, S. Coen, and J. M. Dudley, "Fiber supercontinuum sources (invited)," J. Opt. Soc. Am. B **24**, 1771–1785 (2007).

[36] G. Genty, C. de Sterke, O. Bang, F. Dias, N. Akhmediev, and J. Dudley, "Collisions and turbulence in optical rogue wave formation," Physics Letters A **374**, 989 – 996 (2010).

[37] M. Nakazawa, K. Tamura, H. Kubota, and E. Yoshida, "Coherence degradation in the process of supercontinuum generation in an optical fiber," Optical Fiber Technology **4**, 215 – 223 (1998).

[38] K. Chow, Y. Takushima, C. Lin, C. Shu, and A. Bjarklev, "Flat super-continuum generation based on normal dispersion nonlinear photonic crystal fibre," Electronics Letters **42**, 989–991 (2006).

[39] N. Nishizawa and J. Takayanagi, "Octave spanning high-quality supercontinuum generation in all-fiber system," J. Opt. Soc. Am. B **24**, 1786–1792 (2007).

[40] J. M. Dudley and J. R. Taylor, eds., *Supercontinuum generation in optical fibers* (Cambridge University Press, 2010).

[41] J. C. Travers, M. H. Frosz, and J. M. Dudley, "Nonlinear fibre optics overview," in "Supercontinuum generation in optical fibers," , J. M. Dudley and J. R. Taylor, eds. (Cambridge University Press, New York, 2010), chap. 3, pp. 32–51.

[42] J. M. Dudley, G. Genty, and S. Coen, "Fibre supercontinuum generation overview," in "Supercontinuum generation in optical fibers," , J. M. Dudley and J. R. Taylor, eds. (Cambridge University Press, New York, 2010), chap. 4, pp. 52–61.

[43] K. P. Hansen, "Introduction to nonlinear photonic crystal fibers," Journal of Optical and Fiber Communications Research **2**, 226–254 (2005).

[44] W. H. Reeves, D. V. Skryabin, F. Biancalana, J. C. Knight, P. S. J. Russell, F. G. Omenetto, A. Efimov, and A. J. Taylor, "Transformation and control of ultra-short pulses in dispersion-engineered photonic crystal fibres," Nature **424**, 511–515 (2003).

[45] T. P. White, B. T. Kuhlmey, R. C. McPhedran, D. Maystre, G. Renversez, C. M. de Sterke, and L. C. Botten, "Multipole method for microstructured optical fibers. I. Formulation," J. Opt. Soc. Am. B **19**, 2322–2330 (2002).

[46] M. Koshiba and K. Saitoh, "Applicability of classical optical fiber theories to holey fibers," Opt. Lett. **29**, 1739–1741 (2004).

[47] K. Saitoh and M. Koshiba, "Empirical relations for simple design of photonic crystal fibers," Opt. Express **13**, 267–274 (2005).

[48] G. Agrawal, *Nonlinear Fiber Optics* (Academic Press, 2001).

[49] R. H. Stolen and C. Lin, "Self-phase-modulation in silica optical fibers," Phys. Rev. A **17**, 1448–1453 (1978).

[50] L. F. Mollenauer and J. P. Gordon, *Solitons in Optical Fibers* (Elsevier Academic Press, 2006).

[51] P. K. A. Wai, C. R. Menyuk, H. H. Chen, and C. Lee, "Soliton at the zero-group-dispersion wavelength of a single mode fiber," Opt. Lett. **12**, 628–630 (1987).

[52] E. A. Golovchenko, E. M. Dianov, A. M. Prokhorov, and V. N. Serkin, "Decay of optical solitons," JETP Lett. **42**, 74–77 (1985).

[53] Y. Kodama and A. Hasegawa, "Nonlinear pulse propagation in a monomode dielectric guide," IEEE J. Quantum Electron. **23**, 510 – 524 (1987).

[54] F. M. Mitschke and L. F. Mollenauer, "Discovery of the soliton self-frequency shift," Opt. Lett. **11**, 659–661 (1986).

[55] J. P. Gordon, "Theory of the soliton self-frequency shift," Opt. Lett. **11**, 662–664 (1986).

[56] N. Akhmediev and M. Karlsson, "Cherenkov radiation emitted by solitons in optical fibers," Phys. Rev. A **51**, 2602–2607 (1995).

[57] A. M. Heidt, "Efficient adaptive step size method for the simulation of supercontinuum generation in optical fibers," J. Lightwave Tech. **27**, 3984–3991 (2009).

[58] K. Blow and D. Wood, "Theoretical description of transient stimulated raman scattering in optical fibers," IEEE J. Quantum Electron. **25**, 2665–2673 (1989).

[59] R. H. Stolen, J. P. Gordon, W. J. Tomlinson, and H. A. Haus, "Raman response function of silica-core fibers," J. Opt. Soc. Am. B **6**, 1159 (1989).

[60] P. D. Drummond and J. F. Corney, "Quantum noise in optical fibers. I. Stochastic equations," J. Opt. Soc. Am. B **18**, 139–152 (2001).

[61] P. L. Francois, "Nonlinear propagation of ultrashort pulses in optical fibers: total field formulation in the frequency domain," J. Opt. Soc. Am. B **8**, 276 (1991).

[62] J. Laegsgaard, "Mode profile dispersion in the generalised nonlinear Schrödinger equation," Opt. Express **15**, 16110–16123 (2007).

[63] F. Poletti and P. Horak, "Description of ultrashort pulse propagation in multimode optical fibers," J. Opt. Soc. Am. B **25**, 1645–1654 (2008).

[64] S. Afshar and T. M. Monro, "A full vectorial model for pulse propagation in emerging waveguides with subwavelength structures part I: Kerr nonlinearity," Opt. Express **17**, 2298–2318 (2009).

[65] S. Afshar, M. Turner, and T. M. Monro, "Nonlinear optics in emerging waveguides: revised fundamentals and implications," in "Supercontinuum generation in optical fibers," , J. M. Dudley and J. R. Taylor, eds. (Cambridge University Press, New York, 2010), chap. 11, pp. 226–284.

[66] T. Brabec and F. Krausz, "Nonlinear optical pulse propagation in the single-cycle regime," Phys. Rev. Lett. **78**, 3282–3285 (1997).

[67] N. Karasawa, S. Nakamura, N. Nakagawa, M. Shibata, R. Morita, H. Shigekawa, and M. Yamashita, "Comparison between theory and experiment of nonlinear propagation for a-few-cycle and ultrabroadband optical pulses in a fused-silica fiber," IEEE J. Quantum Electron. **37**, 398 –404 (2001).

[68] I. Cristiani, R. Tediosi, L. Tartara, and V. Degiorgio, "Dispersive wave generation by solitons in microstructured optical fibers," Opt. Express **12**, 124–135 (2004).

[69] J. Hult, "A fourth-order runge–kutta in the interaction picture method for simulating supercontinuum generation in optical fibers," J. Lightwave Technol. **25**, 3770–3775 (2008).

[70] B. M. Caradoc-Davies, "Vortex dynamics in Bose-Einstein condensates," Ph.D. thesis, Univ. Otago, Dunedin, New Zealand (2000).

[71] G. Bosco, A. Carena, V. Curri, R. Gaudino, P. Poggiolini, and S. Benedetto, "Suppression of spurious tones induced by the split-step method in fiber systems simulation," IEEE Phot. Tech. Lett. **12**, 489–491 (2000).

[72] O. V. Sinkin, R. Holzlöhner, J. Zweck, and C. R. Menyuk, "Optimization of the split-step fourier method in modeling optical-fiber communications systems," J. Lightwave Technol. **21**, 61 (2003).

[73] www.photonics.incubadora.fapesp.br.

[74] C. Liu, E. J. Rees, T. Laurila, S. Jian, and C. F. Kaminski, "An adaptive filter for studying the life cycle of optical rogue waves," Opt. Express **18**, 26113–26122 (2010).

[75] A. M. Heidt, J. P. Burger, J.-N. Maran, and N. Traynor, "High power and high energy ultrashort pulse generation with a frequency shifted feedback fiber laser," Opt. Express **15**, 15892–15897 (2007).

[76] K. Kieu, W. H. Renninger, A. Chong, and F. W. Wise, "Sub-100 fs pulses at watt-level powers from a dissipative-soliton fiber laser," Opt. Lett. **34**, 593–595 (2009).

[77] N. B. Chichkov, C. Hapke, K. Hausmann, T. Theeg, D. Wandt, U. Morgner, J. Neumann, and D. Kracht, "0.5 μJ pulses from a giant-chirp ytterbium fiber oscillator," Opt. Express **19**, 3647–3650 (2011).

[78] A. Heidt, G. Bosman, M. Becker, M. Rothhardt, K. Schuster, J. Kobelke, and H. Bartelt, "Prospects of high energy ultrashort pulse generation with frequency shifted feedback fiber oscillators," in "CLEO/Europe and EQEC 2009 Conference Digest," (Optical Society of America, 2009), p. CJ P37.

[79] A. M. Heidt, "Pulse preserving flat-top supercontinuum generation in all-normal dispersion photonic crystal fibers," J. Opt. Soc. Am. B **27**, 550–559 (2010).

[80] D. Anderson, M. Desaix, M. Lisak, and M. L. Quiroga-Teixeiro, "Wave breaking in nonlinear-optical fibers," J. Opt. Soc. Am. B **9**, 1358–1361 (1992).

[81] C. Finot, B. Kibler, L. Provost, and S. Wabnitz, "Beneficial impact of wave-breaking for coherent continuum formation in normally dispersive nonlinear fibers," J. Opt. Soc. Am. B **25**, 1938–1948 (2008).

[82] A. Hartung, A. M. Heidt, and H. Bartelt, "Dispersion design of all-normal dispersive microstructured optical fibers for coherent supercontinuum generation," in "Proc. SPIE," , vol. 8073, F. Baldini, J. Homola, R. A. Lieberman, and K. Kalli, eds. (SPIE, 2011), vol. 8073, p. 80732Q.

[83] A. Hartung, A. M. Heidt, and H. Bartelt, "Design of all-normal dispersion microstructured optical fibers for pulse-preserving supercontinuum generation," Opt. Express **19**, 7742–7749 (2011).

[84] K. Hansen, "Dispersion flattened hybrid-core nonlinear photonic crystal fiber," Opt. Express **11**, 1503–1509 (2003).

[85] A. M. Heidt, A. Hartung, G. W. Bosman, P. Krok, E. G. Rohwer, H. Schwoerer, and H. Bartelt, "Coherent octave spanning near-infrared and visible supercontinuum generation in all-normal dispersion photonic crystal fibers," Opt. Express **19**, 3775–3787 (2011).

[86] A. M. Heidt, J. Rothhardt, A. Hartung, H. Bartelt, E. G. Rohwer, J. Limpert, and A. Tünnermann, "High quality sub-two cycle pulses from compression of supercontinuum generated in all-normal dispersion photonic crystal fiber," Opt. Express **19**, 13873–13879 (2011).

[87] J. Rothhardt, A. Heidt, A. Hartung, H. Bartelt, E. Rohwer, J. Limpert, and A. Tünnermann, "Sub-two cycle pulse generation with all normal dispersion photonic crystal fiber and linear chirp compensation," in "CLEO/Europe and EQEC 2011 Conference Digest," (Optical Society of America, 2011), p. CF3.5.

[88] Nonlinear photonic crystal fiber NL-1050-NEG 1, http://www.nktphotonics.com.

[89] B. Kibler, J. Dudley, and S. Coen, "Supercontinuum generation and nonlinear pulse propagation in photonic crystal fiber: influence of the frequency-dependent effective mode area," Appl. Phys. B **81**, 337–342 (2005).

[90] A. H. Zewail, "Femtochemistry: Atomic-scale dynamics of the chemical bond," J. Phys. Chem. A **104**, 5660–5694 (2000).

[91] S. A. Kovalenko, A. L. Dobryakov, J. Ruthmann, and N. P. Ernsting, "Femtosecond spectroscopy of condensed phases with chirped supercontinuum probing," Phys. Rev. A **59**, 2369–2384 (1999).

[92] A. L. Dobryakov, S. A. Kovalenko, and N. P. Ernsting, "Electronic and vibrational coherence effects in broadband transient absorption spectroscopy with chirped supercontinuum probing," J. Chem. Phys. **119**, 988–1002 (2003).

[93] U. Megerle, I. Pugliesi, C. Schriever, C. Sailer, and E. Riedle, "Sub-50 fs broadband absorption spectroscopy with tunable excitation: putting the analysis of ultrafast molecular dynamics on solid ground," Appl. Phys. B **96**, 215–231 (2009).

[94] J. Rau, C. Ferrante, F. W. Deeg, and C. Bräuchle, "Solvation dynamics of rhodamine 700 in the nematogenic liquid octylcyanobiphenyl," J. Phys. Chem. B **103**, 931–937 (1999).

[95] J. Mulders and L. Steenhuysen, "The performance of dyes and dye mixtures of rhodamine 6G/rhodamine 560 and of styryl 8/styryl 9 for single mode cw ring laser operation," Optics Communications **54**, 295 – 298 (1985).

[96] A. L. Dobryakov, S. A. Kovalenko, and N. P. Ernsting, "Coherent and sequential contributions to femtosecond transient absorption spectra of a rhodamine dye in solution," J. Chem. Phys. **123**, 044502 (2005).

[97] F. X. Kärtner, *Few-Cycle Laser Pulse Generation and Its Applications* (Springer, 2004).

[98] E. Matsubara, K. Yamane, T. Sekikawa, and M. Yamashita, "Generation of 2.6 fs optical pulses using induced-phase modulation in a gas-filled hollow fiber," J. Opt. Soc. Am. B **24**, 985–989 (2007).

[99] A. Baltuška, T. Fuji, and T. Kobayashi, "Visible pulse compression to 4 fs by optical parametric amplification and programmable dispersion control," Opt. Lett. **27**, 306–308 (2002).

[100] S. Hädrich, S. Demmler, J. Rothhardt, C. Jocher, J. Limpert, and A. Tünnermann, "High-repetition-rate sub-5-fs pulses with 12 GW peak power from fiber-amplifier-pumped optical parametric chirped-pulse amplification," Opt. Lett. **36**, 313–315 (2011).

[101] F. Krausz and M. Ivanov, "Attosecond physics," Rev. Mod. Phys. **81**, 163–234 (2009).

[102] V. Yakovlev, P. Dombi, G. Tempea, C. Lemell, J. Burgdörfer, T. Udem, and A. Apolonski, "Phase-stabilized 4-fs pulses at the full oscillator repetition rate for a photoemission experiment," Appl. Phys. B **76**, 329–332 (2003).

[103] B. Schenkel, R. Paschotta, and U. Keller, "Pulse compression with supercontinuum generation in microstructure fibers," J. Opt. Soc. Am. B **22**, 687–693 (2005).

[104] G. Chang, T. B. Norris, and H. G. Winful, "Optimization of supercontinuum generation in photonic crystal fibers for pulse compression," Opt. Lett. **28**, 546–548 (2003).

[105] A. A. Amorim, M. V. Tognetti, P. Oliveira, J. L. Silva, L. M. Bernardo, F. X. Kärtner, and H. M. Crespo, "Sub-two-cycle pulses by soliton self-compression in highly nonlinear photonic crystal fibers," Opt. Lett. **34**, 3851–3853 (2009).

[106] A. A. Voronin and A. M. Zheltikov, "Soliton-number analysis of soliton-effect pulse compression to single-cycle pulse widths," Phys. Rev. A **78**, 063834 (2008).

[107] P. Lazaridis, G. Debarge, and P. Gallion, "Time-bandwidth product of chirped sech2 pulses: application to phase-amplitude-coupling factor measurement," Opt. Lett. **20**, 1160–1162 (1995).

[108] L. E. Hooper, P. J. Mosley, A. C. Muir, W. J. Wadsworth, and J. C. Knight, "Coherent supercontinuum generation in photonic crystal fiber with all-normal group velocity dispersion," Opt. Express **19**, 4902–4907 (2011).

[109] A. M. Heidt, A. Hartung, and H. Bartelt, "Deep ultraviolet supercontinuum generation in optical nanofibers by femtosecond pulses at 400nm wavelength," Proc. SPIE **7714**, 771407 (2010).

[110] P. N. Prasad, *Introduction to Biophotonics* (John Wiley & Sons, 2003).

[111] J. H. V. Price, T. M. Monro, K. Furusawa, W. Belardi, J. C. Baggett, S. Coyle, C. Netti, J. J. Baumberg, R. Paschotta, and D. J. Richardson, "UV generation in a pure-silica holey fiber." Appl. Phys. B **77**, 291 – (2003).

[112] A. Kudlinski, A. K. George, J. C. Knight, J. C. Travers, A. B. Rulkov, S. V. Popov, and J. R. Taylor, "Zero-dispersion wavelength decreasing photonic crystal fibers for ultraviolet-extended supercontinuum generation," Opt. Express **14**, 5715–5722 (2006).

[113] M. H. Frosz, P. M. Moselund, P. D. Rasmussen, C. L. Thomsen, and O. Bang, "Increasing the blue-shift of a picosecond pumped supercontinuum," in "Supercontinuum generation in optical fibers," , J. M. Dudley and J. R. Taylor, eds. (Cambridge University Press, New York, 2010), chap. 3, pp. 32–51.

[114] S. P. Stark, A. Podlipensky, N. Y. Joly, and P. S. J. Russell, "Ultraviolet-enhanced supercontinuum generation in tapered photonic crystal fiber," J. Opt. Soc. Am. B **27**, 592–598 (2010).

[115] S. P. Stark, A. Podlipensky, and P. S. J. Russell, "Soliton blueshift in tapered photonic crystal fibers," Phys. Rev. Lett. **106**, 083903 (2011).

[116] M. A. Foster, J. M. Dudley, B. Kibler, Q. Cao, D. Lee, R. Trebino, and A. L. Gaeta, "Nonlinear pulse propagation and supercontinuum generation in photonic nanowires: experiment and simulation." Appl. Phys. B **81**, 363 – 367 (2005).

[117] M. A. Foster, A. C. Turner, M. Lipson, and A. L. Gaeta, "Nonlinear optics in photonic nanowires," Opt. Express **16**, 1300–1320 (2008).

[118] J. Love, W. Henry, W. Stewart, R. Black, S. Lacroix, and F. Gonthier, "Tapered single-mode fibres and devices. I. Adiabaticity criteria," Optoelectronics, IEE Proceedings J **138**, 343 –354 (1991).

[119] A. Hartung, S. Brueckner, and H. Bartelt, "Limits of light guidance in optical nanofibers," Opt. Express **18**, 3754–3761 (2010).

[120] R. G. Smith, "Optical power handling capacity of low loss optical fibers as determined by stimulated raman and brillouin scattering," Appl. Opt. **11**, 2489–2494 (1972).

A. Appendix: Numerical Implementation Details

A.1. Symmetric split-step Fourier method

The SSFM finds an approximate solution to the general pulse propagation equation in time (3.6) or frequency (3.12) formulation by assuming that dispersive and nonlinear operator act independently, while in reality they act together [48]. The dispersive step has an exact solution

$$\frac{\partial \tilde{A}_L}{\partial z} = \hat{D}(\omega)\tilde{A}_L \qquad \leftrightarrow \qquad \tilde{A}_L(z+h,\omega) = \exp[h\hat{D}(\omega)]\tilde{A}_L(z,\omega), \tag{A.1}$$

while the nonlinear step must in general be solved by numerical integration due to its own z-dependence

$$\frac{\partial \tilde{A}_N}{\partial z} = \hat{N}(z,\omega)\tilde{A}_N \qquad \leftrightarrow \qquad A_N(z+h,\omega) = \int_z^{z+h} \hat{N}(z',\omega)\tilde{A}_N(z',\omega)\mathrm{d}z'. \tag{A.2}$$

The SSFM combines the two operations by first taking half a dispersive step, followed by the nonlinear step and the final dispersive half-step

$$\tilde{A}(z+h,\omega) \approx \exp\left(\frac{h}{2}\hat{D}\right)\exp\left(\int_z^{z+h}\hat{N}(z')\mathrm{d}z'\right)\exp\left(\frac{h}{2}\hat{D}\right)\tilde{A}(z,\omega). \tag{A.3}$$

For the nonlinear integration, a fourth-order Runge-Kutta solver is applied, so that the propagation step is explicitly calculated by

$$\begin{aligned}
\tilde{A}_I &= \exp\left(\frac{h}{2}\hat{D}\right)\tilde{A}(z,\omega),\\
k_1 &= \hat{N}\tilde{A}_I,\\
k_2 &= \hat{N}(\tilde{A}_I + \frac{h}{2}k_1),\\
k_3 &= \hat{N}(\tilde{A}_I + \frac{h}{2}k_2),\\
k_4 &= \hat{N}(\tilde{A}_I + hk_3),\\
\tilde{A}(z+h,\omega) &\approx \exp\left(\frac{h}{2}\hat{D}\right)\left[A_I + \frac{h}{6}k_1 + \frac{h}{3}k_2 + \frac{h}{3}k_3 + k_4\right].
\end{aligned} \tag{A.4}$$

One longitudinal step therefore requires four evaluations of the $\hat{N}$, which requires a total of 16 Fourier transforms. The numerical error is introduced because the SSFM ignores the non-commuting nature of the operators $\hat{D}$ and $\hat{N}$resulting in an error term per step of order $O(h^3)$. Note that the total number of steps is inversely proportional to h, so that the global error at the end of the simulation is $O(h^2)$.

A.2. Runge-Kutta in the interaction picture method

The RK4IPM transforms the pulse propagation equation into an interaction picture in order to separate the dispersive terms in $\hat{D}$ from the non-dispersive terms in $\hat{N}$. It is closely related to the SSFM described above and is described in detail in [69]. The algorithm advancing the spectral envelope from z to $z+h$ is given by

$$\begin{aligned}
\tilde{A}_I &= \exp\left(\frac{h}{2}\hat{D}\right)\tilde{A}(z,\omega), \\
k_1 &= \exp\left(\frac{h}{2}\hat{D}\right)\left[h\hat{N}\tilde{A}(z,\omega)\right], \\
k_2 &= h\hat{N}(A_I + \frac{k_1}{2}), \\
k_3 &= h\hat{N}(A_I + \frac{k_2}{2}), \\
k_4 &= h\hat{N}\left[\exp\left(\frac{h}{2}\hat{D}\right)(A_I + k_3)\right], \\
\tilde{A}(z+h,\omega) &\approx \exp\left(\frac{h}{2}\hat{D}\right)\left[A_I + \frac{k_1}{6} + \frac{k_2}{3} + \frac{k_3}{3}\right] + \frac{k_4}{6}.
\end{aligned} \tag{A.5}$$

The RK4IPM also requires four evaluations of $\hat{N}$ with a total of 16 Fourier transforms. The main advantage of (A.5) is the high accuracy of the integration with a dominant local error term of order $O(h^5)$, making it possible to set h much larger than in (A.4) to reach the same accuracy and therefore making the calculation significantly faster than the SSFM.

A.3. General Properties of the Fourier methods

Both SSFM and RK4IPM make use of discrete Fourier transforms to switch between time and frequency domains. The time window width $T_{\max}$ of the simulation is defined by the time resolution Δt and the number of computational points N,

$$T_{\max} = (N-1)\Delta t. \tag{A.6}$$

The properties of the discrete Fourier transform then define the corresponding frequency window with width $F_{\max}$ and resolution $\Delta\nu$,

$$\Delta\nu = \frac{1}{N\Delta t} \simeq \frac{1}{T_{\max}}, \tag{A.7}$$

$$F_{\max} = (N-1)\Delta\nu \simeq \frac{1}{\Delta t}, \tag{A.8}$$

whereby the frequency window is centered around the central frequency v_0. This also defines the minimum and maximum wavelengths in the simulation,

$$\lambda_{\min} = \frac{\lambda_0}{1+\frac{1}{2c\Delta t}}, \tag{A.9}$$

$$\lambda_{\max} = \frac{\lambda_0}{1-\frac{1}{2c\Delta t}}, \tag{A.10}$$

with the central wavelength λ_0.

A.4. Scaling and Normalization

Both temporal and spectral envelope should be normalized such that

$$E = \int_0^{T_{\max}} |A(t)|^2 \mathrm{d}t = \int_{\omega_{\min}}^{\omega_{\max}} |\tilde{A}(\omega)|^2 \mathrm{d}\omega, \tag{A.11}$$

where E is the total energy of the pulse. $|A(t)|^2$ is therefore the instantaneous power, and $|\tilde{A}(\omega)|^2$ is connected to the power spectral density $S(\omega)$ via the repetition rate f_{rep}

$$S(\omega) = f_{\mathrm{rep}}|\tilde{A}(\omega)|^2 \tag{A.12}$$

to obtain the scaling for the average power

$$P_{\mathrm{av}} = f_{\mathrm{rep}}E = \int_{\omega_{\min}}^{\omega_{\max}} S(\omega)\mathrm{d}\omega. \tag{A.13}$$

In plots, the spectral power density is often displayed on a wavelength scale. In this case care must be taken to ensure proper rescaling to observe the identity

$$P_{\mathrm{av}} = \int_{\omega_{\min}}^{\omega_{\max}} S(\omega)\mathrm{d}\omega = \int_{\lambda_{\max}}^{\lambda_{\min}} S(\lambda)\mathrm{d}\lambda = -\int_{\lambda_{\min}}^{\lambda_{\max}} S(\lambda)\mathrm{d}\lambda. \tag{A.14}$$

Through comparison one obtains the relation

$$S(\lambda)\mathrm{d}\lambda = -S(\omega)\mathrm{d}\omega. \tag{A.15}$$

Using (A.12) and

$$\frac{\mathrm{d}\omega}{\mathrm{d}\lambda} = -\frac{2\pi c}{\lambda^2} \tag{A.16}$$

the transformation equation for the spectral power density on wavelength scale can be deducted as

$$S(\lambda) = \frac{2\pi c}{\lambda^2} f_{\mathrm{rep}} |\tilde{A}(\omega)|^2. \tag{A.17}$$

A.5. One photon per mode

In section 3.1.2 input pulse shot noise is included into the simulation by adding one photon per mode with random spectral phase into each frequency bin, which models the effects of spontaneous emission noise [120]. The power of the one photon per mode field is

$$P_{\mathrm{oppm}} = \int_{\omega_{\mathrm{min}}}^{\omega_{\mathrm{max}}} \hbar\omega \mathrm{d}\omega. \tag{A.18}$$

Comparison with (A.13) yields $S_{\mathrm{oppm}}(\omega) = \hbar\omega$, and using the relation in (A.12)

$$|\tilde{A}_{\mathrm{oppm}}(\omega)|^2 = \frac{1}{f_{\mathrm{rep}}} \hbar\omega. \tag{A.19}$$

Therefore, the spectral envelope of the one photon per mode field for each frequency bin ω_m can be written as

$$\tilde{A}_{\mathrm{oppm}}(\omega_m) = \sqrt{\frac{\hbar\omega}{f_{\mathrm{rep}}}} \exp[-i\Phi(\omega_m)], \tag{A.20}$$

where $\Phi(\omega_m)$ is a random phase sampled uniformly over the interval $[0; 2\pi]$. $\tilde{A}_{\mathrm{oppm}}(\omega_m)$ is then inverse Fourier transformed to yield $A_{\mathrm{oppm}}(t_m)$ which is added to the input field.

List of publications

The following publications resulted from the work on this dissertation:

Journal publications:

- A. M. Heidt, "Efficient adaptive step size method for the simulation of supercontinuum generation in optical fibers," J. Lightwave Tech. **27**, 3984-3991 (2009).
- A. M. Heidt, "Pulse preserving flat-top supercontinuum generation in all-normal dispersion photonic crystal fibers," J. Opt. Soc. Am. B **27**, 550-559 (2010).
- A. M. Heidt, A. Hartung, G. W. Bosman, P. Krok, E. G. Rohwer, H. Schwoerer, and H. Bartelt, "Coherent octave spanning near-infrared and visible supercontinuum generation in all-normal dispersion photonic crystal fibers," Opt. Express **19**, 3775-3787 (2011).
- A. Hartung, A. M. Heidt, and H. Bartelt, "Design of all-normal dispersion microstructured optical fibers for pulse-preserving supercontinuum generation," Opt. Express **19**, 7742-7749 (2011).
- A. Hartung, A. M. Heidt, and H. Bartelt, "Pulse-preserving broadband visible supercontinuum generation in all-normal dispersion tapered suspended core optical fibers," Opt. Express **19**, 12275-12283.
- A. M. Heidt, J. Rothhardt, A. Hartung, H. Bartelt, E. G. Rohwer, J. Limpert, and A. Tünnermann, "High quality sub-two cycle pulses from compression of supercontinuum generated in all-normal dispersion photonic crystal fiber," Opt. Express **19**, 13873-13879.
- A. M. Heidt, A. Hartung, and H. Bartelt, "Optimization of photonic nanowires for coherent supercontinuum generation at deep ultraviolet wavelengths," (in preparation).

International conference contributions:

- Best Student Paper Award: A. M. Heidt, A. Hartung, and H. Bartelt, "Deep ultraviolet supercontinuum generation in optical nanofibers by femtosecond pulses at 400nm wavelength," in SPIE Photonics Europe / Photonic Crystal Fibers IV, Proc. SPIE 7714, 771407 (2010).
- Best Student Paper Award: A. M. Heidt, A. Hartung, E. G. Rohwer and H. Bartelt, "Infrared, visible and ultraviolet broadband coherent supercontinuum generation in all-normal dispersion fibers," in 2nd Workshop on Specialty Optical Fibers and their Applications, Proc. SPIE 7839, 78390X (2010).

- A. Hartung, A. M. Heidt, and H. Bartelt, "Dispersion design of all-normal dispersive microstructured optical fibers for coherent supercontinuum generation," in SPIE Optics + Optoelectronics 2011 / Photonic Crystal Fibers V, Proc. SPIE 8073, 8073Q (2011).

- J. Rothhardt, A. M. Heidt, A. Hartung, H. Bartelt, E. G. Rohwer, J. Limpert, and A. Tünnermann, "Sub-two cycle pulse generation with all normal dispersion photonic crystal fiber and linear chirp compensation," in CLEO/Europe and EQEC Conference 2011, paper CF 3.5.

Local conference contributions:

- A. M. Heidt, "Controlling supercontinuum generation in microstructured optical fibers," 53rd Annual Conference of the South African Institute of Physics, University of Limpopo, 2008.

- Best PhD Student Presentation Award: A. M. Heidt, "Spectral and temporal confinement of supercontinua generated in photonic crystal fiber," in 54th Annual Conference of the South African Institute of Physics, University of KwaZulu-Natal, 2009.

- Best PhD Student Presentation Award: A. M. Heidt, A. Hartung, H. Bartelt and E. G. Rohwer, "New concepts for broadband coherent supercontinuum generation in microstructured optical fibers and photonic nanowires," in 55th Annual Conference of the South African Institute of Physics, CSIR Conference Center Pretoria, 2010.